Doctoral Thesis

Carbon-based Electrocatalysts for Oxygen Reduction Reactions

Hyun-Jung Choi

Department of Energy Engineering

Graduate School of UNIST

2016

Carbon-based Electrocatalysts for Oxygen Reduction Reactions

Hyun-Jung Choi

Department of Energy Engineering

Graduate School of UNIST

Carbon-based Electrocatalysts for Oxygen Reduction Reactions

A thesis/dissertation
submitted to the Graduate School of UNIST
in partial fulfillment of the
requirements for the degree of
Doctor of Philosophy

Hyun-Jung Choi

1. 13. 2016

Approved by

Advisor
Jong-Beom Baek

Carbon-based Electrocatalysts for Oxygen Reduction Reactions

Hyun-Jung Choi

This certifies that the thesis/dissertation of Hyun-Jung Choi is approved.

1. 13. 2016

signature

Advisor: Jong-Beom Baek

signature

Jaephil Cho: Thesis Committee Member #1

signature

Hyun-Kon Song: Thesis Committee Member #2

signature

Guntae Kim: Thesis Committee Member #3

signature

Dong Wook Chang: Thesis Committee Member #4;

Abstract

Due to the rapid industrial development and growing human population, along with the increase in energy demand, the global energy consumption has been accelerating at an alarming rate. At current consumption rate, global energy exhaustion will become inevitable. Fuel cell draws tremendous attention as the upcoming alternative energy source. Because fuel cells are eco-friendly process to produce electricity, water and heat only with no pollutant or toxic by-product, many researches are now focusing on cost down and efficiency up fuel cells. The challenging and current bottleneck lies in the sluggish oxygen reduction reaction (ORR) kinetics on the cathode that significantly limits the efficiency and performance of the fuel cell device. Platinum is the most widely studied noble metal as electrocatalyst. However, it is too expensive and limited reserve in earth. Therefore, exploring new electrocatalysts with enhanced ORR activities and stabilities for the replacement of this costly noble metal with non-platinum alternatives is highly warranted and is of paramount importance to commercialize fuel cells as well as for other renewable energy applications. In this thesis, I explained with a brief overview of ORR in fuel cells and then I introduced my research results, including platinum incorporated multi-walled carbon nanotubes, heteroatom doped graphene and iron encapsulated polymers related with oxygen reduction reaction in both acidic and alkaline medium. Furthermore, these catalysts showed excellent electrocatalytic activities toward ORR with a high selectivity, good tolerance to methanol crossover/CN and SCN poisoning effects, and good long-term cycle stability.

Table of Contents

List of Figures

sealed ball-mill capsule and the remnant active carbon species are terminated upon subsequent exposure to air moisture. Red and gray balls stand for oxygen and hydrogen, respectively; (b) ball-mill capsule containing the pristine graphite and stainless steel balls (diameter 5 mm); (c) violent sparkling (red spots) occurred when the reaction mixture was exposed to ambient air moisture and excess purple I_2 was sublimated in the air (arrow); (d) continued sparkling from residual IGnP at the bottom of a ball-mill capsule even after most of the IGnPs and stainless balls were taken out.

Figure 3-2. Schematic representation of the edge-selective halogenation of graphite by ball-milling in the presence of halogens, such as chlorine (Cl_2), bromine (Br_2) and iodine (I_2) to produce edge-chloro- (ClGnP), edge-bromo- (BrGnP) and edge-iodo-graphene nanoplatelets (IGnP), respectively. The graphitic structures are simplified for clarity. The red and blue lines represent armchair and zigzag cuts, respectively, resulting in the red and blue dots as active carboradicals. The active carbon species are (1) reacted with halogen molecules and (2) subsequently terminated by air moisture upon opening ball-mill capsule lid to produce the edge-halogenated graphene nanoplatelets.

Figure 3-3. SEM images: (a) the pristine graphite with average grain size ~150 μm. The average grain sizes of XGnPs reduced to less than 1 μm: (b) ClGnP; (c) BrGnP; (d) IGnP. Scale bars are 1 μm. (e) EDX spectra. (f) XRD diffraction patterns. Inset is magnified XRD diffraction patterns from the pink rectangle. The relative [002] peak intensities of XGnPs are less than 0.4% of that of the pristine graphite, indicating that the great extent of graphite has been deliminated into edge-halogenated graphene nanoplatelets (XGnPs). (g) A schematic representation for the edge expansions of XGnPs caused by the edge-halogens.

Figure 3-4. EDX (FE-SEM) element mappings of samples: (a) the pristine graphite with halogen mapping; (b) ClGnP with chlorine mapping; (c) BrGnP with bromine mapping; (d) IGnP with iodine mapping. Scale bars are 250 nm.

Figure 3-5. Photographs of XGnPs dispersed solutions in various solvents after one week standing on bench top in the normal laboratory condition: **(a)** ClGnP; **(b)** BrGnP; **(c)** IGnP. Zeta-potentials of XGnPs in DMF at different concentrations: **(d)** 0.10 mg/mL; **(e)** 0.04 mg/mL. The solvents used in this study are: (1) H_2O; (2) 1M HCl; (3) 1M KOH; (4) diethyl ether (5) MeOH; (6) EtOH; (7) THF; (8) acetone; (9) DMAc; (10) DMF; (11) NMP; (12) dichloromethane; (13) dichlorobenzene; (14) benzene; (15) CS_2.

Figure 3-6. TEM images of ClGnP: (a) bright field (BF) image. Inset is the selected area electron diffraction (SAED) pattern; (b, c) energy-filtered images; (d) high-resolution image of 2-3 graphitic layers (arrows) with honeycomb lattice image (inset), indicating high crystallinity. EDX (HR-TEM) element mappings from rectangle in (b): (e) carbon; (f) oxygen; (g) chlorine.

Figure 3-14. The optimized O_2 adsorption geometries onto XGnPs, in which halogen covalently linked to two sp^2 carbons: (a) ClGnP; (b) BrGnP; (c) IGnP. The projected density of electronic states onto O_2: (d) ClGnP; (e) BrGnP; (f) IGnP for the cases of corresponding (a), (b), and (c), respectively. In (a), (b) and (c), the O-O bond length and the shortest C-O bond are shown in angstroms.

Figure 3-15. The optimized O_2 adsorption geometries onto XGnPs, in which halogen covalently linked to the sp^2 carbon as dangling bond: (a) ClGnP; (b) BrGnP; (c) IGnP. The projected density of electronic states onto O_2: (d) ClGnP; (e) BrGnP; (f) IGnP corresponding to (a), (b), and (c), respectively. In (a), (b) and (c), the bond lengths of the shortest C-O and O-O are shown in angstroms. In (d), (e) and (f), the downward and upward double arrows indicate the HOMO and LUMO states of O_2 triplet (doubly degenerated antibonding states). When sp^2 C-X is dangling bond, the charge transfer from the basal plane to the adsorbed O_2 is negligible, as indicated by the occupation of the LUMO states. It is thus thought that these configurations of halogenated edges do not contribute to the ORR catalysis.

Figure 3-16. (a) Current-time (*i-t*) chronoamperometric response of the pristine graphite, XGnPs, and commercial Pt/C electrodes at -0.25 V *vs.* Ag/AgCl in O_2-saturated 0.1 M aq. KOH solution at a rotation rate of 1600 rpm. Note that the blue and green curves are almost overlapped with each other. (b) The current-time (*j-t*) chronoamperometric responses for ORR at the pristine graphite, XGnPs, and commercial Pt/C electrocatalysts in an O_2-saturated 0.1 M aq. KOH solution at -0.40 V *vs.* Ag/AgCl and 3.0 M methanol was added at around 280 s.

Figure. 4-1. Synthesis and structural characterization of Fe@C_2N. (A) Schematic presentation of the Fe@C_2N synthesis. Inset: behavior of Fe@C_2N in the magnetic field, showing the attraction of the black Fe@C_2N particles toward a magnet and the accumulation of these particles on the side of the glass wall (B) Low-magnification of the HR-TEM image. The scale bar is 100 nm. (C) High-magnification of the HR-TEM image showing the encapsulated Fe nanoparticles. The scale bar is 5 nm. The inset is the fast Fourier transform (FFT) of Fe@C_2N. (D) Powder XRD pattern of the Fe@C_2N compared with those of Fe_3C and pure Fe. (E) X-ray absorption near edge structure (XANES) spectra of Fe@C_2N, Fe and Fe_3O_4. (F) Fourier transform radial distribution of Fe@C_2N, Fe and Fe_3O_4.

Figure. 4-21. Fe@C_2N energy dispersive X-ray spectroscopy (EDS) spectrum showing the elemental mapping and compositing (C, N, O and Fe) from the SEM image.

A uniform distribution of Fe nanoparticles in the C_2N framework was detected by element mappings in the EDS analysis. EDS (Figure. 4-2A) and XPS (Figure. 4-3) survey spectra of Fe@C_2N revealed

the presence of C, N, O (physically adsorbed oxygen and residue of HKH at the edges of C_2N structure) and Fe. Their detailed compositions are summarized in Table 4-1.

Figugre. 4-3. (A) XPS survey spectrum showing C 1s, Fe 2p, N 1s and O 1s. Inset is deconvoluted O 1s XPS stectrum of Fe@C_2N. Deconvoluted XPS spectra of Fe@C_2N: (B) C 1s; (C) N 1s; (D) Fe 2p. The important peaks identified in the XPS survey spectrum correspond to different chemical states of carbon, nitrogen, oxygen and iron atoms, respectively (Figure. 4-3). High resolution XPS spectra for C 1s, N 1s, O 1s and Fe are shown in the Figure S2. C 1s can be resolved into three major peaks at 284.7 eV (C=C), 285.3 eV (C-N), 287.6 eV (C=O) and 290.9 eV (C-C plasmon) (Figure. 4-3B). There are two peaks of element N 1s in Figure 4-3C. The peak at 398.7 eV corresponds to the binding energy of the N-heteroatom and the peak at 400.6 eV corresponds to the pyrazine like nitrogen in the C2N framework. O 1s is resolved into a peak at 531.7 eV C=O bonds at the edges of C2N structures (inset, Figure 4-3A). The high-resolution XPS spectrum of Fe shows that there are peaks at for the Fe $2p_{3/2}$ and Fe $2p_{1/2}$ suggestive of the presence of metallic iron or its carbides. The peaks at 707.3 eV in the Fe $2p_{3/2}$ and 720.2 eV in the Fe $2p_{1/2}$ show that the metallic Fe in Fe@C_2N.

Figure. 4-4. HR-TEM images of as-prepared Fe@C_2N mounted on carbon grid after dispersion in NMP. (A, C) HR-TEM images of as-prepared Fe@C_2N. (B, D) Inter layer distance from the red marked line, respectively. Inset of (C) is the fast Fourier transform (FFT) of marked blue dot square.

Figure 4-5. Nitrogen adsorption and desorption isotherms for the Fe@C_2N. The Brunauer-Emmett-Teller (BET) specific surface area is approximately 584 $m^2 g^{-1}$ which is quite high. The nitrogen adsorption-desorption isotherms exhibit a hysteresis loop of type H4 indicating the presence of slit like pores between the layers.

Figure 4-6. Cyclic voltammograms of Pt/C and Fe@C_2N in O_2-saturated (solid line) and N_2-saturated conditions: (A) 0.1 M KOH; (B) 0.5 M H_2SO_4 solution. The scan rate was 0.01 V s^{-1}.

Figure 4-7. Electrochemical evaluation of Fe@C_2N. (A, B) Rotating ring-disk electrode (RRDE) voltammograms (bottom), percentage of peroxide (middle) and electron transfer number (*n*) (top) recorded with Fe@C_2N and Pt/C at 1,600 rpm in O_2-saturated conditions: (A) 0.1 M aq. KOH solution and (B) 0.5 M aq. H_2SO_4 solution. The disk potential was scanned at 10 mV s^{-1} and the ring potential was constant at 1.4 V *vs.* RHE. Tafel plots were obtained by mass-transport correction of corresponding RDE measurements at 1,600 rpm in O_2-saturated conditions: (C) 0.1 M aq. KOH solution and (D) 0.5 M H_2SO_4 solution. The catalyst loading was 0.795 mg cm^{-2} (159 μgPt cm^{-2}).

Figure 4-8. Polarization curves on a glassy carbon RDE voltammograms for Pt/C and Fe@C_2N in O_2-saturated (A,B) 0.1 M aq KOH solution and (D,E) 0.5 M aq H_2SO_4 with a scan rate of 0.01 V s^{-1} at different rotating rates of 600, 900, 1200, 1600, 2000, and 2500 rpm. Inset is Koutecky-Levich plots

List of Tables

Abbreviations

1. LIB (Lithium ion battery)
2. ORR: oxygen reduction reaction
3. OER: oxygen evolution reaction
4. HOR: hydrogen oxidation reaction
5. HER: hydrogen evolution reaction
6. HO^-: hydrogen peroxide anion
7. H_2O_2: hydrogen peroxide
8. MWCNT: Multi-walled carbon nanotube
9. DAB-MWCNT: 3,4-diaminobenzoylfunctionalized MWCNTs
10. PNP: platinum nanoparticle
11. CNT: Carbon nanotube
12. PPA: polyphosphoric acid
13. P_2O_5: phosphorous pentoxide
14. H_3PO_4: phosphorous pentoxide
15. HNO_3: Nitric Acid
16. H_2SO_4: Sulfuric acid
17. DABA: 3,4-diaminobenzoic acid
18. FT-IR: Fourier-transform infrared
19. EA: Elemental analysis
20. TGA: Thermogravimetric analysis
21. WAXD: Wideangle X-ray diffraction
22. FE-SEM: field emission scanning electron microscopy
23. HR-TEM: High-resolution transmission electron microscopy
24. MSA: methanesulfonic acid
25. NMP: Nmethyl-2-pyrrolidone

26. CV: cyclic voltammetry
27. GC: glassy carbon
28. RDE: rotating disk electrode
29. XRD: X-ray diffraction
30. SEM: scanning electron
31. TEM: transmission electron
32. XGnP: edge-selectively halogenated graphene nanoplatelets
33. Pt: platinum
34. CO: carbon monoxide
35. VA-NCNT: vertically-aligned nitrogen-doped carbon nanotube
36. N-graphene: nitrogen-doped graphene
37. CVD: chemical vapor deposition
38. DFT: density-functional theory
39. BET: Brunauer-Emmett-Teller
40. XPS: . X-ray photoelectron spectra
41. AFM: atomic force microscopy
42. GnP: graphene nanoplatelet
43. SAED: selected area electron diffraction
44. HGnP: edge-hydrogenated GnP
45. LSV: linear sweep voltammetry
46. RDE: rotating disk electrode
47. LUMO: lowest-unoccupied molecular orbital
48. ADT: accelerated degradation test
49. C_2N: nitrogenated holey two-dimensional carbon framework
50. EXAFS: extended X-ray fine structures
51. HKH: Hexaketocyclohexane octahydrate
52. HAB: Hexaaminobenzene trihydrochloride

53. RRDE: Rotating ring disk electrode
54. TEGDM: tetraethylene glycol dimethyl ether
55. DI: deionized water
56. PVDF-HFP: poly(vinylidene fluoride-*co*-hexafluoropropylene)
57. FFT: fast Fourier transform
58. Fe@C_2N: Fe nanoparticle encapsulated in C_2N
59. $FeCl_3$: iron chloride
60. $NaBH_4$: sodium borohydride
61. EDS: Energy-dispersive spectroscopy
62. XANES: X-ray absorption near edge structure
63. Fe_xO_y: iron oxides
64. K-L plot: Koutechy-Levich plot
65. OCV: open-circuit voltage
66. PEMFC: polymer electrolyte membrane fuel cell

Chapter I. Introduction

Note: This chapter if partially and toaaly adapted with permission from Graphene supported non-precious metalmacrocycle catalysts for oxygen reduction reaction in fuel cells" Nanoscale, 2015, 7, 6991. Copyright ⓒ 2015 Royal Society of Chemistry

An alarming increase in environmental pollution and ever increasing energy consumption has turned research attention towards clean and energy efficient alternative systems. Lithium ion batteries (LIBs), supercapacitors and fuel cells show promise to meet the colossal energy demand. Fuel cells are devices that directly convert chemical energy from a fuel into electricity by an electrochemical reaction,[1–3] and are on par with supercapacitors and LIBs. With near zero emission of pollutants, high power density and high energy-conversion, fuel cell technology is swiftly shifting from basic research towards commercial development.[4,5] Typical fuel cells consist of an anode, cathode and a membrane. At the cathode, electrochemical fuel oxygen reduction reaction (ORR) and oxygen evolution reaction (OER) take place, whereas hydrogen oxidation reaction (HOR) and hydrogen evolution reaction (HER) take place at the anode.[6] The challenging and current bottleneck lies in the sluggish ORR kinetics on the cathode that significantly limits the efficiency and performance of the fuel cell device. Because platinum-based (Pt) electrocatalysts have been traditionally used to catalyze the ORR, a fuel cell stack alone accounts up to 50% of the cost of the whole system.[7] Although Pt-based composites are most efficient cathode catalysts, they still suffer from serious drawbacks that include crossover poisoning, low stability, especially in acidic media thus leading to declined activity or performance loss. Most important of all, limited reserves and prohibitively high costs hinder wide spread commercialisation of fuel cells in general. Therefore, exploring new electrocatalysts with enhanced ORR activities and stabilities for the replacement of this costly noble metal with non-precious alternatives is highly warranted and is of paramount importance to commercialise fuel cells as well as for other renewable energy applications. In the intensifying search for durable and efficient materials, researchers have tried to reduce the amount of Pt used by lowering platinum usage,[8–10] use of non-precious metal catalysts[11,12] that are abundant in nature and also metal free catalysts for ORR have been actively explored.[13–18] Obviously, the latter two hold astounding importance in realising cheap fuel cell technology.

1.1 Kinetics and mechanism of the ORR

Low temperature fuel cells are attracting considerable interest as a means of producing electricity by direct electrochemical conversion of hydrogen and oxygen into water.[19] Oxygen reduction is considered to proceed by the following two overall pathways.[20,21] The ORR takes place at the cathode

is of particular importance in fuel cells, since it is a multi-electro reaction, and a good control of the number of electrons involved is essential for the efficiency of the overall system. Indeed, in the ORR, two pathways are possible : (i) one involving the transfer of 2-elecrons to produce the hydrogen peroxide anion (HO_2^-) in alkaline media (3) hydrogen peroxide (H_2O_2) in acidic media (6) which are eventually reduced ((4,5) and (7,8)) ; (ii) is second involving a direct transfer of 4-electrons to produce hydroxide (OH^-) in alkaline media (1) or water (H_2O) in acidic media (2). The undesirable production of H_2O_2 (2-electron pathway) is the key limiting issue for the fuel cell power output because it causes the degradation of the catalytic sites, while the 4-electron pathway allows obtaining the maximum energy capacity.

1.1.1 Direct 4-electron pathway

Alkaline solutions.

$$O_2 + 2H_2O + 4e^- \rightarrow 4OH^-; \quad E_o = 0.401 \text{ V} \qquad (1)$$

Acid solutions.

$$O_2 + 4H^+ + 4e^- \rightarrow 2H_2O; \quad E_o = 1.229 \text{ V} \qquad (2)$$

1.1.2 2-electron pathway

Alkaline solutions.

$$O_2 + H_2O + 2e^- \rightarrow HO_2^- + OH^-; \quad E_o = -0.065 \text{ V} \quad (3)$$

$$HO_2^- + H_2O + 2e^- \rightarrow 3OH^-; \quad E_o = 0.867 \text{ V} \qquad (4)$$

$$\text{or } 2HO_2^- \rightarrow 2OH^- + O_2 \qquad (5)$$

Acid solutions.

$$O_2 + 2H^+ + 2e^- \rightarrow H_2O_2; \quad E_o = 0.67 \text{ V} \qquad (6)$$

$$H_2O_2 + 2H^+ + 2e^- \rightarrow 2H_2O; \quad E_o = 1.77 \text{ V} \qquad (7)$$

$$\text{or } 2H_2O_2 \rightarrow 2H_2O + O_2 \qquad (8)$$

The potentials correspond to the standard state values vs. the normal hydrogen electrode (NHE) at 25^{o}C. Note that in alkaline solutions the sum of reactions Eqs. (3,4) or Eqs. (3,5) is the equivalent of the overall 4-electron reaction Eq. (1). Likewise, the sum of reactions in Eqs. (6 and 7) or Eqs. (6 and 8) is equivalent to reaction Eq. (2) in acid electrolytes.

The extent, to which each of these pathways is involved at a particular electrode surface, is usually established with the rotating ring-disc electrode technique[22] with the ring used to monitor peroxide produced on the disc electrode. Typically, the reaction appears to be under a combined kinetic-diffusion control of charge transfer and mass transport. It is apparent that the electrode rotation has an effect on the reaction rate at very high over potentials for the ORR. But no well diffusion limiting current is reached over the measurement potential range for the ORR on the disk electrode.

Figure 1-1. shows the simplified principal reaction scheme for the reduction of oxygen that occurred in acidic media.[23] Once an oxygen molecule is adsorbed on a catalytic site, it can either follow the direct 4-electron pathway to form water (k_1 and Eq. (2)) or the 2-electron pathway to generate hydrogen peroxide (k_2 and Eq. (6)). Hydrogen peroxide either desorbed from the catalyst surface (k_{-6}), is further reduced to water in the 2 x 2 pathway (k_3 and Eq. (7)), or can chemically decompose to form water and oxygen (k_4 and Eq. (8)). In analyzing the kinetics of the 2 x 2 peroxide pathway, two independent active sites can be assumed for the respective reaction steps (k_2 and k_3), while maintaining that intermediate species are still formed.

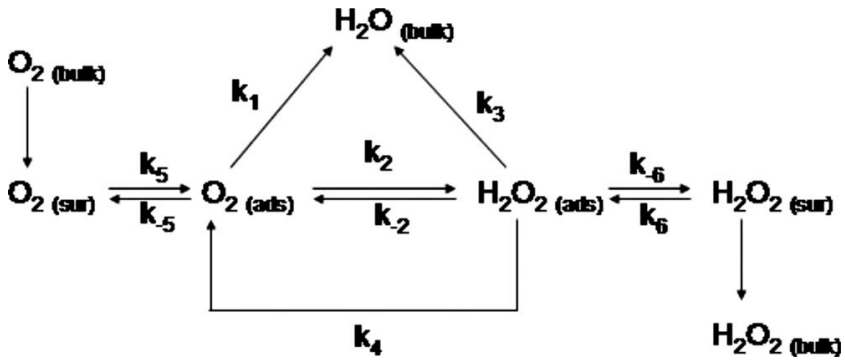

Figure 1-1. Schematic showing oxygen reduction pathways in acidic media.[23]

As the Tafel slope of -58 mV/dec is the value for O_2 reduction on Pt/C, and this can be ascribed to the transfer of the first electron as a rate-determining step and Temkin conditions of intermediate adsorption.[24.25]

According to the flooded-agglomerate, liquid-electrolyte model, (1) when the ORR is controlled by kinetics and the diffusion of dissolved O_2, the data should show a doubled Tafel slope of Pt/C and be first order in O_2 partial pressure; (2) when the ORR is controlled by kinetics and ionic transport, a doubled Tafel slope of Pt/C and half-order in O_2 partial pressure should be expected; (3) in the case of kinetics, diffusion of dissolved O_2 and ionic transport control, this model predicts a quadrupled Tafel slope of Pt/C and half-order in O_2 partial pressure.

1.2 References

(1) M. Z. Jacobson, W. G. Colella and D. M. Golden, Science, 2005, 308, 1901–1905.

(2) M. G. Schultz, T. Diehl, G. P. Brasseur and W. Zittel, Science, 2003, 302, 624–627.

(3) M. Dresselhaus and I. Thomas, Nature, 2001, 414, 332–337.

(4) C. K. Dyer, J. Power Sources, 2002, 106, 31–34.

(5) A. Heinzel, C. Hebling, M. Müller, M. Zedda and C. Müller, J. Power Sources, 2002, 105, 250–255.

(6) W. Sheng, H. A. Gasteiger and Y. Shao-Horn, J. Electrochem. Soc., 2010, 157, B1529–B1536.

(7) J. K. B. James, in DOE-EERE Fuel Cell Technologies Program-2009 DOE Hydrogen Program Review (http://www.hydrogen.energy.gov/pdfs/review09/fc_30_james.pdf).

(8) S. Guo and S. Sun, J. Am. Chem. Soc., 2012, 134, 2492–2495.

(9) K. A. Kuttiyiel, K. Sasaki, Y. Choi, D. Su, P. Liu and R. R. Adzic, Energy Environ. Sci., 2012, 5, 5297–5304.

(10) A. Morozan, B. Jousselme and S. Palacin, Energy Environ. Sci., 2011, 4, 1238–1254.

(11) Y. Liang, Y. Li, H. Wang, J. Zhou, J. Wang, T. Regier and H. Dai, Nat. Mater., 2011, 10, 780–786.

(12) Z.-S. Wu, S. Yang, Y. Sun, K. Parvez, X. Feng and K. Müllen, J. Am. Chem. Soc., 2012, 134, 9082–9085.

(13) S. Wang, L. Zhang, Z. Xia, A. Roy, D. W. Chang, J.-B. Baek and L. Dai, Angew. Chem., Int. Ed., 2012, 51, 4209–4212.

(14) L. Yang, S. Jiang, Y. Zhao, L. Zhu, S. Chen, X. Wang, Q. Wu, J. Ma, Y. Ma and Z. Hu, Angew. Chem., Int. Ed., 2011, 123, 7270–7273.

(15) I.-Y. Jeon, H.-J. Choi, M. Choi, J.-M. Seo, S.-M. Jung, M.-J. Kim, S. Zhang, L. Zhang, Z. Xia, L. Dai, N. Park and J.-B. Baek, Sci. Rep., 2013, 3, 2260.

(16) S. Chen, J. Bi, Y. Zhao, L. Yang, C. Zhang, Y. Ma, Q. Wu, X. Wang and Z. Hu, Adv. Mater., 2012, 24, 5593–5597.

(17) C. Zhang, N. Mahmood, H. Yin, F. Liu and Y. Hou, Adv. Mater., 2013, 25, 4932–4937.

(18) I.-Y. Jeon, S. Zhang, L. Zhang, H.-J. Choi, J.-M. Seo, Z. Xia, L. Dai and J.-B. Baek, Adv. Mater., 2013, 25, 6138–6145.

(19) Markovic, N. M.; Ross, P. N. New Electrocatalysts for Fuel Cells: From Model. Surfaces to Commercial Catalysts *Cattech.* **2000**, *4*, 110.

(20) Yeager E., Mechanism of electrochemical reactions on non-metallic surfaces, in Electrocatalysis on Non-metallic Surfaces, pp. 203-219. NBS Special Publication, **1976**, 455.

(21) Tarasevich M., Sadkowski A. and Yeager E., Oxygen electrochemistry, in Comprehensive Treutise of Efecrrochemisrry, Vol. 7: Kineries and Mechanism of Ekctrode Processes, Chapter 6,

pp. 301-398. Plenum Press, New York, **1983**.

(22) Paulus U. A., Schmidt T. J. , Gasteiger H.A., Behm R.J., Oxygen reduction on a high-surface area Pt:Vulcan carbon catalyst: a thin-film rotating ring-disk electrode study, J. Elec.Chem. **2001**, *495*, 134–145.

(23) Tim S. Olson, Svitlana Pylypenko, Julia E. Fulghum, and Plamen Atanassov , Bifunctional Oxygen Reduction Reaction Mechanism on Non-Platinum Catalysts Derived from Pyrolyzed Porphyrins, J. Electrochem. Soc., **2010**, *157* (1) B54-B63.

(24) Gojkovic´ SL, Gupta S, Savinell RF. Heat-treated iron(III) tetramethoxyphenyl porphyrin chloride supported on higharea carbon as an electrocatalyst for oxygen reduction Part II. kinetics of oxygen reduction. J. Electroanal. Chem. **1999,** *462*, 63–72.

(25) S˘ epa DB, Vojnovic´ MV, Damjanovic´ A. Reaction intermediates as a controlling factor in the kinetics and mechanism of oxygen reduction at platinum electrodes. Electrochim. Acta **1981**, *26*(6), 781–93.

Chapter II. Immobilization of platinum nanoparticles on 3,4-diaminobenzoyl-functionalized multi-walled carbon nanotube and its electrocatalytic acitivty

Note: This chapter is partially and totally adapted with permission from "Immobilization of platinum nanoparticles on 3,4-diaminobenzoyl-functionalized multi-walled carbon nanotube and its electrocatalytic acitivty", Journal of Nanoparticle Research 2012, 14, 704. Copyright ⓒ 2012 Springer.

2.1 Abstract

Multi-walled carbon nanotubes (MWCNTs) are functionalized at the sp2 C–H defect sites with 3,4-diaminobenzoic acid by a ''direct'' Friedel–Crafts acylation reaction in a mild polyphosphoric acid/phosphorous pentoxide medium. Owing to enhanced surface polarity, the resulting 3,4-diaminobenzoylfunctionalized MWCNTs (DAB-MWCNT) are highly dispersible in polar solvents, such as ethanol, N-methyl-2-pyrrolidone, and methanesulfonic acid. The absorption and emission properties of DABMWCNT in solution state are qualitatively shown to be sensitive to the pH in the environment. The DABMWCNT is used as a stable platform on which to deposit platinum nanoparticles (PNP). The PNP/DABMWCNT hybrid displays high electrocatalytic activity with good electrochemical stability for an oxygen reduction reaction under an alkaline condition..

2.2 Introduction

Carbon nanotubes (CNTs) have attracted a lot of attention because of their excellent mechanical, thermal, and electrical properties, and chemical stability, stemming from their unique elongated fullerene structure.[1] CNTs are good candidates as advanced materials such as nanoscale reinforcing additives[2] and catalytic supports.[3-5] More recently, in a research directed to combine the advantages of CNTs and metal nanoparticles, various approaches to generating such hybrid systems have been reported, such as physical evaporation,[6] thermal reduction of adsorbed metal salts under H_2 atmosphere,[7] ''wet'' reduction of metal salts adsorbed on surface oxidized CNTs,[8] redox reaction between metal ions and reduced CNT,[9] nanoscale electroless metal deposition process,[10] and assembly of CNT–metal nanoparticle hybrids using biointerfaces.[11] Among these options, the deposition of nanoparticles onto the surface-functionalized CNTs is perhaps the most reliable for performance, reproducibility, and scalability.[7-9] The dispersion and functionalization of raw CNTs have been typically carried out by sonication[12.13] in strong acids such as sulfuric acid and nitric,[14-16] or sonication in strong acid mixtures.[8,17,18] However, it is generally known that such treatments could result in structural damage to the CNTs.[19] As a result, the CNTs would lose valuable characteristics such as

their electrical properties and structural integrity after introducing various oxygenated groups into their framework. The oxidized defects on the CNTs are probable sites for deactivation of transition metal catalysts.[20] Hence, the development of a simple and benign process for functionalization becomes more important for the CNTs without and/or with minimal damages.[21,22] We have developed a non-oxidizing and less destructive method that combines purification and functionalization of carbon-based nanomaterials in a single-pot process utilizing polyphosphoric acid (PPA) with additional phosphorous pentoxide (P_2O_5), which plays the roles of a solvating/dispersing medium and a Brönsted catalyst for Friedel–Crafts acylation of carbon nanomaterials.[23] PPA is a polymeric form of phosphoric acid (H_3PO_4, pKa ~ 2.1), which is less corrosive and practically non-oxidizing as compared with commonly used strong acids (HNO_3, pKa ~ -1.3; H_2SO_4, pKa ~ -3.0). Commercial grade PPA (83% P_2O_5 assay) has been used as a polymerization medium for the synthesis of high-performance polybenzazoles (PBXs).[24,25] If the purification and functionalization of CNTs could be achieved in a non-destructive and one-pot fashion, then it would be an ideal system to exploit. In this study, multi-walled carbon nanotubes (MWCNTs) were functionalized with 3,4-diaminobenzoic acid (DABA) via ‘‘direct’’ Friedel–Crafts acylation reaction to produce covalently 3,4-diaminobenzoyl-functionalized MWCNT (DAB-MWCNT). Platinum nanoparticle (PNP), is a known catalyst for hydrogenation and Heck reactions that can bind strongly amine groups.[26] It is believed that PNP can be stably anchored to DABMWCNT without agglomeration. Thus, the resulting PNP/DAB-MWCNT hybrid is expected to have high electrocatalytic performance with good electrochemical stability.

2.3 Materials and Instrumentation

All reagents and solvents were purchased from Aldrich Chemical Inc., USA and were used as received, unless otherwise specified. MWCNT (CVD MWCNT 95 with a diameter of ~20 nm and a length of 10–50 μm) was obtained from Hanwaha Nanotech Co., LTD, Seoul, Korea. The commercial grade platinum on the activated carbon catalyst (Pt/C, C2–20, 20% HP Pt on Vulcan XC-72R, E-TEK Division, PE-MEAS Fuel Cell Technologies) was provided by BASF Fuel Cell.

The Fourier-transform infrared (FT-IR) spectra were recorded on a Jasco FT-IR 480 plus spectrophotometer. Solid samples were imbedded in KBr disks. Elemental analysis (EA) was performed using a CE Instrument EA1110. Thermogravimetric analysis (TGA) was conducted in an air atmosphere with a heating rate of 10 $^oC\ min^{-1}$ using a TA Q200. Wideangle X-ray diffraction (WAXD) powder patterns were recorded using a Rigaku RU-200 diffractometer applying Ni-filtered Cu Ka radiation (40 kV, 100 mA, k = 0.15418 nm). The field emission scanning electron microscopy (FE-SEM) used in this study was performed using an FEI NanoSEM 230. High-resolution transmission electron microscopy (HR-TEM) in this study was performed using a JEOL JEM-2100F (Cs) operating at 200 kV. Photoluminescence measurements were performed using a Perkin-Elmer LS

55 fluorescence spectrometer. Stock solutions were prepared by dissolving 20 mg of each sample in 5 mL (4 mg mL^{-1}) of methanesulfonic acid (MSA) or Nmethyl-2-pyrrolidone (NMP). The excitation wavelength was that of the UV absorption maximum of each sample. For electrochemical measurements, cyclic voltammetry (CV) was carried out using a VersaSTAT3 AMETEK model (Princeton Applied Research, TN, USA) potentiostat/galvanostat employing a standard three-electrode electrochemical cell. This consisted of samples on glassy carbon (GC) with a diameter of 3 mm as the working electrode, an Ag/AgCl (saturated KCl) reference electrode, and platinum gauze as the counter electrode. Experiments were carried out at room temperature in a 0.1 M aqueous KOH electrolyte solution. Either nitrogen or oxygen gas was used to purge the solution to achieve an oxygen-free or an oxygen-saturated electrolyte solution, respectively. All potentials are reported relative to an Ag/AgCl (saturated KCl) reference electrode recorded at a scan rate of 10 mV s^{-1}. The potential window for cycling was confined between -1.0 V and +0.2 V in a basic electrolyte to omit the extra current generated by samples in the alkaline medium. The GC electrode was polished with alumina slurry before use to obtain a mirror-like surface. Samples (2.0 mg) were dispersed in NMP (0.2 mL), and aliquots of the suspension (10 μL) were coated on GC electrodes and dried under reduced pressure (0.5-mm Hg) for 24 h at 50 ^{o}C. Nafion (5%, 5 μL) in ethanol was pipetted onto the sample/GC electrode and allowed to dry at laboratory conditions for 2 h. Electrodes for rotating disk electrode (RDE) voltammogram measurements were prepared on a 3 mm diameter GC disk electrode (ALS, Japan).

2.4 Synthesis of 3,4-diaminobenzoyl-functionalized MWCNT (DAB-MWCNT)

3,4-Diaminobenzoic acid (5.0 g, 31.02 mmol), MWCNT (5.0 g), PPA (83% P_2O_5 assay; 200.0 g) and P_2O_5 (40.0 g) were placed in a 250 mL resin flask equipped with a high torque mechanical stirrer, nitrogen inlet and outlet, and stirred under dry nitrogen purge at 80 ^{o}C for 1 h. The temperature was increased incrementally to 100 ^{o}C over 1 h. Then, the reaction mixture was stirred at 130 ^{o}C for an additional 72 h. At the end of the reaction, the mixture was cooled to room temperature, and distilled water was added. The precipitates were isolated and Soxhlet-extracted with water for 3 days to completely remove the reaction medium and then with methanol for three more days to remove other possible impurities. The final product was freeze-dried under reduced pressure (0.05 mm DAB-MWCNT, which could be easily broken up. Found: C, 79.17%; H, 1.93%; N, 8.31%, and O, 5.67%.

2.5 Preparation of thin DAB-MWCNT paper via solution casting

Film was cast from DAB-MWCNT (1.0 g) dispersed in MSA, 20 mL. The resultant homogeneous solution was cast on a leveled glass plate in a custom-made film-casting apparatus. MSA was slowly removed by heating the apparatus to 80 ^{o}C under reduced

pressure (0.05 mm Hg). The resultant film was removed from the glass plate after immersion in distilled water. The free-standing films were sandwiched between Teflon membranes to keep them pressed, and then kept under distilled water for 4 days. The film was further Soxhlet-extracted with water for 3 days and then methanol for an additional 3 days to ensure complete removal of residual MSA. FT-IR spectra of the DABMWCNT film were obtained from a crushed sample that was imbedded in KBr pellet and showed that there was no trace of residual MSA by judging the absence of m(SO_2) for MSA at 1,202 (symmetric stretching) and 1,403 (asymmetric stretching) cm^{-1}. The average DC conductivity of the cast film was 280 ± 8 S m^{-1}.

2.6 In situ synthesis of PNP/DAB-MWCNT hybrid

The PNP was prepared according to the procedure described by Ahmadi et al.[27] In short, an aqueous solution, containing 18.4 mL of DI water, 0.5 mL of an aqueous 0.05 M $H_2PtCl_6 \cdot 6H_2O$ solution, and 0.5 mL of an aqueous 0.05 M trisodium citrate solution, was mixed in a conical flask. To this solution, an ice-cold aqueous solution (0.6 mL) containing 0.1 M $NaBH_4$ was added in one portion under vigorous magnetic stirring. The solution turned red immediately after the addition of the $NaBH_4$ solution, indicating PNP's formation. DAB-MWCNT (50 mg) was dispersed in 30 mL of ethanol by ultrasonic agitation for 3 min. Then black suspension was added to the solution containing platinum colloids (20 mg) at room temperature. After stirring for 24 h, PNP/DABMWCNT hybrids were collected through filtration, washed with water several times, and completely dried under reduced pressure (0.05 mm Hg) at 100 ^oC for 24 h. The procedures of GC electrode pretreatment and modification are described as follows: before use, the working electrode was polished with alumina slurry to obtain a mirror-like surface and then washed with DI water and allowed to dry. The samples (1 mg) were dispersed in 1 mL solvent mixture of Nafion (5%) and EtOH/water (v/v = 1:9) by sonication. Each sample suspension (5 μl) was pipetted on the GC electrode surface, followed by drying at room temperature.

2.7 Results and Discussion

Table 2-1 summarizes the EA results. The hydrogen content of a multi-walled carbon nanotube (MWCNT) is 0.30 wt%. The maximum possible ratio of hydrogen/carbon (H/C) is approximately 1/27, which explains the existence of sp^2C–H on the tube defects. Similar to the electrophilic substitution reaction of benzene, the available sp^2C–H is the site for the Friedel–Crafts acylation reaction of MWNCT. Thus, DAB-MWCNT could be prepared from the reaction between DABA and MWCNT in a mild PPA/P_2O_5 medium (Figure. 2-1).[22] The advantage of the reaction medium is that it

is non-destructive, but strong enough for efficient functionalization compared with typical functionalization by destructive oxidation in nitric acid/sulfuric acid mixtures.[28] The elemental contents of DAB-MWCNT from EA are consistent with theoretical and experimental values (Table 2-1).

Table 2-1. Elemental analysis (EA) data of MWCNT and DAB-MWCNT

Sample		Elemental Analysis				
		C (%)	H (%)	N (%)	O (%)	H/C ratio
MWCNT	Cacd.	100.00	0.00	0.00	0.00	0
	Found	97.81	0.30	BDL*	0.59	1/27.4
DAB-	Cacd.	84.25	1.32	9.17	5.24	1/5.4
MWCNT	Found	79.17	1.93	8.31	5.67	1/6.6

*BDL= blow detection limit

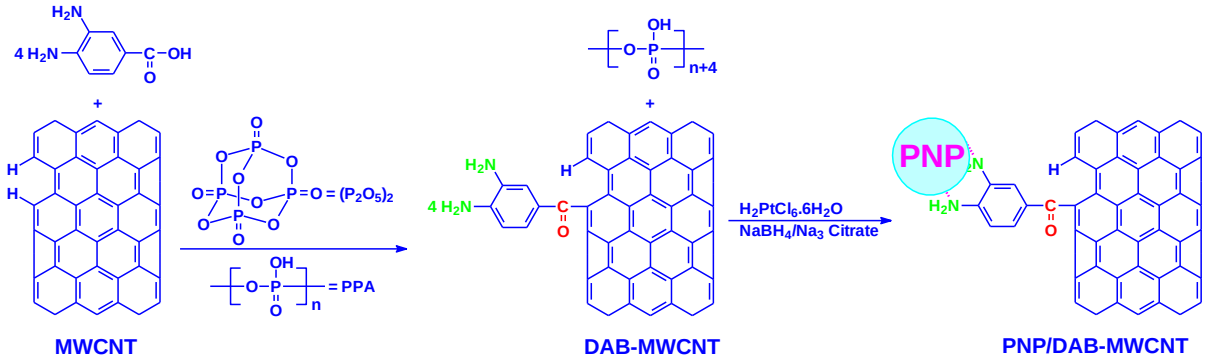

Figure 2-1. Functionalization of multi-walled carbon nanotubes (MWCNT) with 3,4-diaminobenzoic acid (DABA) to produce 3,4-diaminobenzoyl-functionalized MWCNT (DAB-MWCNT) and preparation of platinum nanoparticles (PNP) on DAB-MWCNT (PNP/DAB-MWCNT).

In order to verify the structure of DAB-MWCNT, FT-IR spectroscopy was commonly used as a convenient tool to trace the chemical modification of carbon nanomaterials.[23] Since CNTs strongly absorb infrared light, samples have to be carefully prepared to collect reliable spectra. The thinner KBr window gives better resolution. While MWCNT shows a featureless spectrum (Figure. 2-2a), DABMWCNT displays a strong ketone carbonyl (C=O) stretching band at 1,639 cm^{-1}. In addition, DABMWCNT also displays distinct C–N stretching band at 1,385 cm^{-1}. Although the N–H stretching bands around 3,430 and 3,350 cm^{-1} are obscured by the more intense and broad O–H stretching band (3,500–3,000 cm^{-1}) of lattice-bound water in the KBr, the right shoulder (Figure. 2-2b, sky blue oval) from DAB-MWCNTs should be attributed to amine of the N–H stretching band (sky blue arrow).

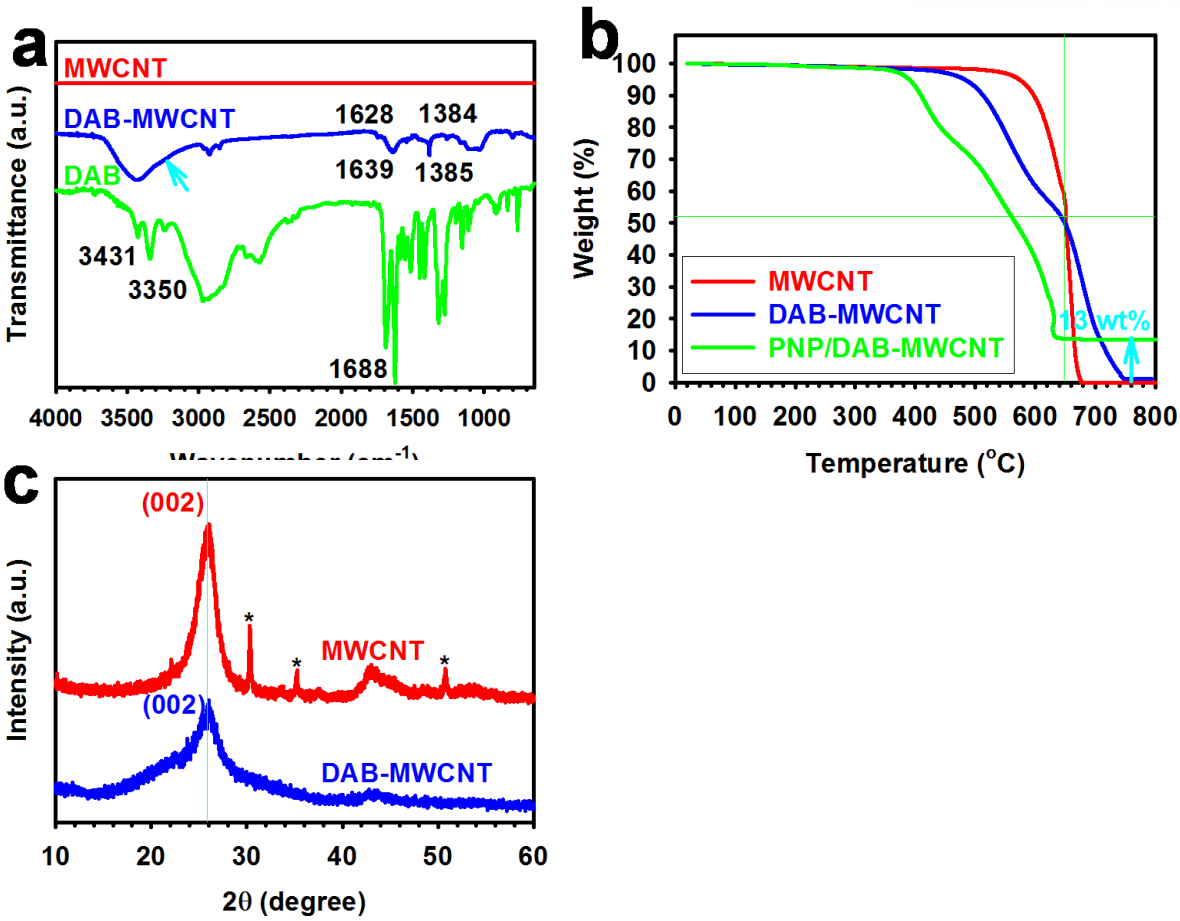

Figure 2-2. (a) FT-IR (KBr pellet) spectra; (b) TGA thermograms obtained with heating rate of 10 °Cmin^{-1} in air; (c) XRD patterns. Metallic impurity peaks are completely disappeared in DAB-MWCNT, while wall-to-wall interlayer peak remains at 26.0° (*d*-spacing = 3.42 Å).

The degree of functionalization was estimated by using thermogravimetric analysis (TGA) in air. Since the functionalization is non-destructive, the early weight loss is ascribable to thermo-oxidative decomposition of DAB ($C_7H_7N_2O$, FW = 136.06) moiety. DAB-MWCNT shows a two-step weight loss from ~460℃ to 800℃. Initial weight loss from ~460-650 ℃ was 48 wt%, which is attributed to thermo-oxidative stripping of the DAB moiety (Figure 2-2b). The value agreed well with the feed ratio of DAB/MWCNT (1/1, wt/wt) and near-quantitative yield of DAB-MWCNT, indicating high efficiency functionalization. Thus, the degree of functionalization is estimated to be less than 8 atom%.

Furthermore, the role of the reaction medium and morphology of DAB-MWCNT could be evaluated from X-ray diffraction (XRD) patterns. The XRD powder pattern from pristine MWCNT shows the presence of metallic impurities (peaks marked with *), while there are no peaks for impurities in the DAB-MWCNT (Figure 2-2c). The result suggests that the reaction medium can purify and functionalize MWCNT at the same time. DAB-MWCNT shows (002) peak at 26.00° (d-spacing = 3.42 Å).

The functionalization could be visually ascertained by scanning electron (SEM) and transmission electron (TEM) microscopes. Pristine MWCNT shows that their surface is clean and smooth with diameter dimensions in the range of 10~20 nm (Figure 2-3a). DAB-MWCNT is uniformly coated with DAB moiety and the average diameter was increased to about 40~50 nm (Figure 2-3b). Magnified images clearly resolve core-shell structure (Figure 2-3c). The average diameter of an inner core is approximately 20 nm and the average thickness of an outer shell is roughly 15 nm (Figure 2-3c, inset). Considering the average diameter of pristine MWCNT (10~20nm) and the average thickness of DAB layer (~1 nm), the increased thickness should be due to bundling of DAB-MWCNT[29] because the surface polarity of DAB-MWCNT is much higher than that of pristine MWCNT. The enhanced lateral interactions of DAB-MWCNT driven by inter-tube hydrogen bonding after functionalization is strong enough to overcome the rigidity of MWCNT, resulting in the formation of DAB-MWCNT bundles. The result implies that the uniform decoration of DAB onto the surface of MWCNT may be achieved through “direct” Friedel-Crafts acylation reaction in PPA/P_2O_5.

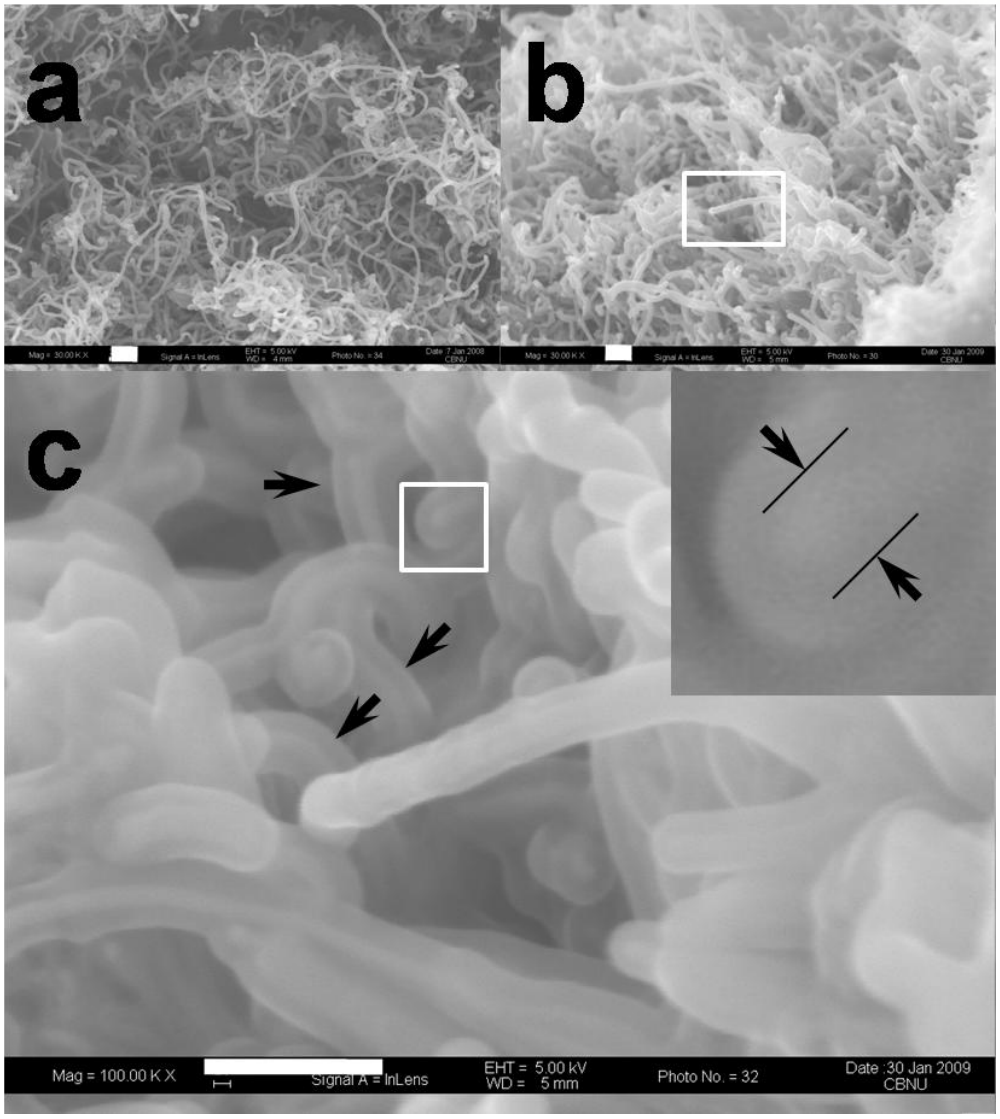

Figure 2-3. SEM images of samples: (a) pristine MWCNT; (b) DAB-MWCNT; (c) magnified image of the rectangle area in (b). Inset is magnified image from a white square in (c), showing core-shell structure of DAB-MWCNT. Scale bars are 200 nm.

The morphology of DAB-MWCNT could be further assayed by TEM. Again, the surface of pristine MWCNT is apparently clean and smooth (Figure 2-4a and 2-4b), showing almost no carbonaceous impurity deposits. On the contrary, DAB moiety is uniformly populating the surface of MWCNT (Figure 2-4c). Specifically, the tip of the DAB-MWCNT appears to be more DAB-coated (white arrow) due to the possibility of sp^2C-H defects at the tube end being much higher.[30]

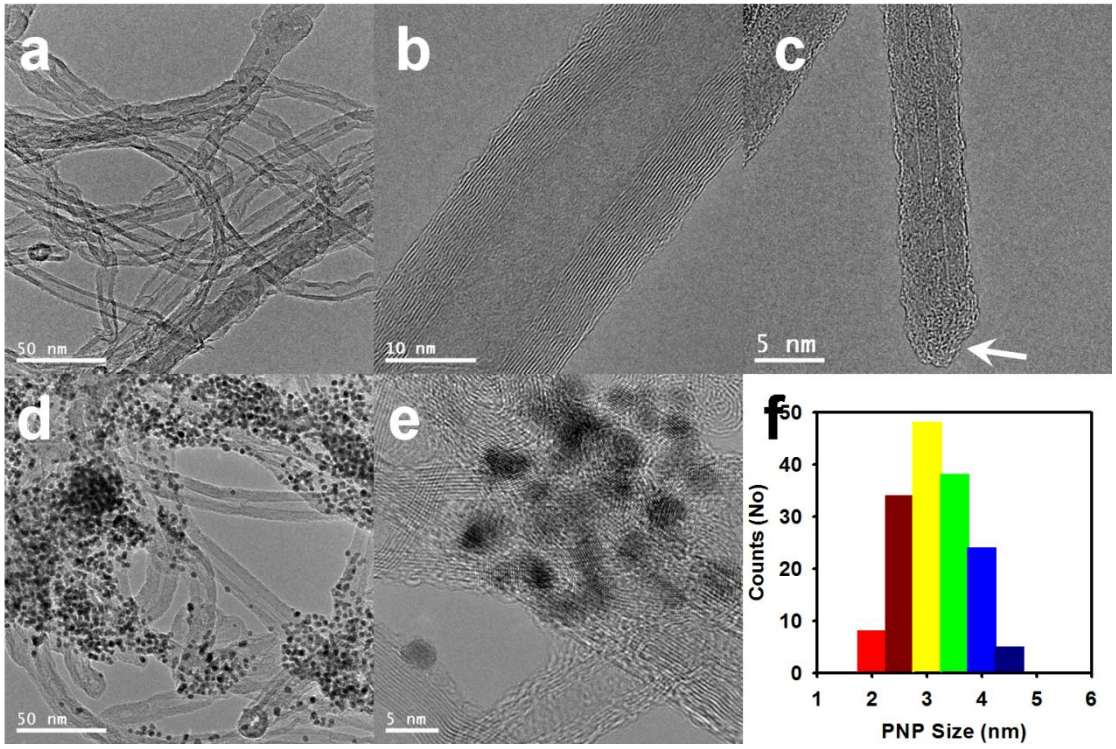

Figure 2-4. TEM images of samples: (a, b) pristine MWCNT; (c) DAB-MWCNT, showing uniform decoration of DAB moiety onto the surface of MWCNT; (d, e) PNP/DAB-MWCNT; (f) the particle size distribution of PNP, which is uniform in the range of 3-5 nm.

DAB-MWCNT is dispersed well in both acidic and basic solvents, e.g. methanesulfonic acid (MSA) and *N*-methyl-2-pyrrolidone (NMP), respectively, as well as their mixtures. In addition, it is also dispersible in alcohol, probably due to its enhanced surface polarity. The photograph of the DAB-MWCNT in MSA solutions demonstrates its strong dispersibility (Figure 2-5a, inset). These solutions were homogeneous and transparent, while pristine MWCNT solution contained mostly MWCNT agglomerates (not shown). The DAB-MWCNT displayed different UV-absorption and emission behaviors in different solvents. DAB-MWCNT in an acidic MSA solution had an absorption maximum at 365 nm (Figure 2-5a). The absorption maximum is red-shifted to 373 nm in a basic NMP solution (Figure 2-5b). Interestingly, when a few drops of the DAB-MWCNT in MSA solutions were added to pure NMP, the absorption peak red-shifted to 404 nm (Figure 2-5a). The absorption maxima changes were closely related to the conjugation-length changes of the ground state in different solvents. In the two extreme cases, namely in NMP and MSA solutions, this is clearly determined by the availability of the nitrogen lone-pair electrons of the DAB pendants to participate or not (Figure 2-5c). In the intermediate case, the red-shift to 404 nm is rather surprising, suggesting even longer conjugation length and the possibility of extension into CNT framework. The emission maximum of

DAB-MWCNT in MSA solution was 394 nm with a right shoulder peak at 415 nm (Figure 2-5b). The solution emitted strong blue light when exposed to a hand-held UV light (365 nm) (Figure 2-5b, inset). Similar to UV-vis absorption behavior, the sample in NMP solution shows that the peak red-shifted and centered at 421 nm with a right shoulder peak at 440 nm (Figure 2-5b). In comparing with the spectrum of MSA solution, the peak maximum was shifted bathochromically by as much as 27 nm, implying that the electronic structure of the excited state had been affected by vastly different solvent environments. Surprisingly, the solution prepared from adding a few drops of DAB-MWCNT/MSA solution into pure NMP displayed a broader emission band with peak at 531 nm (Figure 2-5b), showing a strong sky-blue fluorescence (Figure 2-5b, inset). The emission peak was red-shifted by as much as 137 nm as compared to the spectrum of MSA solution. Similar to the UV absorption behavior, significant red-shifted emission maxima are related to extended conjugation lengths of charged complexes in NMP (Figure 2-5c). Both UV-vis absorption and emission behaviors also strongly suggest that homogeneous dispersions of DAB-MWCNT can be achieved in organic solvents ranging from basic to acidic.

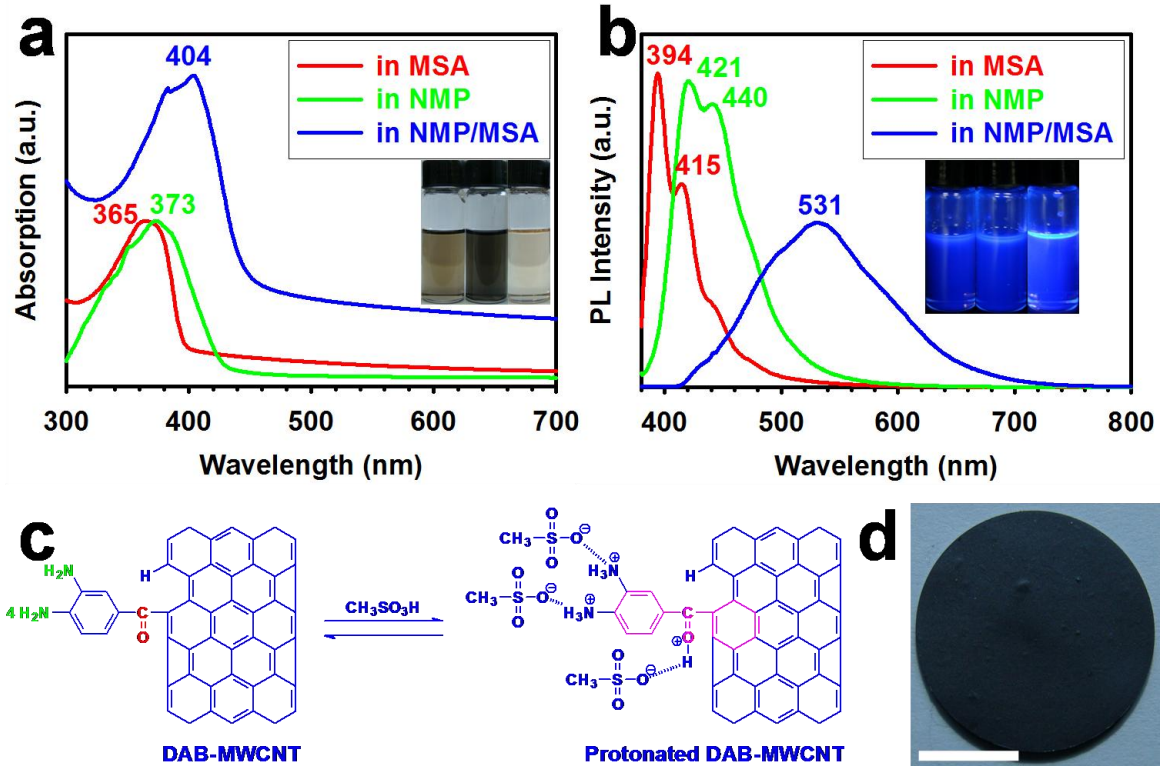

Figure 2-5. (a) UV- vis absorption and (b) emission spectra of DAB-MWCNT solutions in MSA, NMP and NMP with a few drops of MSA solution. Inset in (a) is photo of the solutions without hand-held UV lamp and inset in (b) is photo of the solutions with hand-held UV lamp (365 nm). The excitation wavelengths are UV-vis absorption maximum of each sample; (c) proposed charge complex formation of DAB-MWCNT in MSA solution; (d) DAB-MWCNT thin paper. Scale bar is 1 cm.

After homogeneous dispersion of DAB-MWCNT in MSA had been confirmed spectroscopically, the solution was cast on a leveled Petri dish and the MSA evaporated to produce DAB-MWCNT thin paper as described in the Experimental section (Figure 2-5d). The electrical conductivity of the resultant paper was measured by a standard four-point probe method under laboratory conditions. The average electrical conductivities of the paper were 280 ± 8 $S \cdot m^{-1}$, which is surprisingly better than the reported values for elastomer-nanotube thin films[31] or doped MWCNT-conjugated polymer films.[32] This may be the best results so far for such a simple strategy, indicating that a relatively high loading of MWCNT has led to easy formation of a conduction network in the DBA-MWCNT thin paper, resulting in improved electrical properties.

By having numerous ortho-diaminobenzoyl units on the surface of DAB-MWCNT, platinum nanoparticles (PNP) could be efficiently immobilized on the surface of the DAB-MWCNT to produce a PNP/DAB-MWCNT hybrid.[26] The DAB(o-diamine)-platinum chelate-type coordination bonding[33] is expected to be stable, and thus, should display an enhanced electrochemical stability. Since PNP is aggregate-prone during an electrochemical reaction, the catalytic surface area is reduced.[34] If CNT could provide a higher surface area to uniformly hold and immobilize PNP, higher electrocatalytic activity may be possible.[35,36] In this work, the amount of PNP loaded was determined by TGA analysis to be *ca.* 13 wt% (Figure 2-2b). The size distribution of PNP is uniform and in the range of 2-5 nm determined by TEM (Figure 2-4d-2-4f). Cyclic voltammetry (CV) was performed in N_2 and O_2-saturated, 0.1M aqueous KOH solutions in the potential range of -1.0 to 0.2 V versus Ag/AgCl and with a sweep rate of 10 $mV \cdot s^{-1}$. Hence, CV was used to estimate the electrocatalytic activity of the modified electrodes. For comparison, the CV curves were recorded for DAB-MWCNT and PNP/DAB-MWCNT on glassy carbon (GC) electrodes. DAB-MWCNT shows a featureless redox behavior in a N_2-saturated medium (Figure 2-6a), while a weak reduction peak at -2.6 V in an O_2-saturated medium (Figure 2-6b). PNP/DAB-MWCNT hybrid displays distinct reduction peaks at -0.16 and -0.14V in both N_2- and O_2-saturated media, respectively (Figure 2-6a and 2-6b). Compared to DAB-MWCNT, the PNP/DAB-MWCNT hybrid shows significantly higher current and lower reduction potential, illustrating that the PNP/DAB-MWCNT electrode possesses much higher electrocatalytic activity and lower activation barrier for oxygen reduction reaction (ORR). For reference, CV curves for commercially available Vulcan XC-72R on GC electrodes, which displays higher current and reduction potential at -0.25 and -0.27V, in both N_2- and O_2-saturated media, respectively, indicate that Vulcan XC-72R electrodes have higher electrocatalytic activity and activation barrier than the PNP/DAB-MWCNT electrodes. However, when taking into account the PNP contents of the PNP/DAB-MWCNT (13 wt%) and Vulcan XC-72R (20 wt%), electrocatalytic activities in a N_2-saturated medium are actually quite similar for both electrodes (Figure 2-6c), the

PNP/DAB-MWCNT electrode in an ORR condition is approximately 85% that of Vulcan XC-72R electrodes after 100 cycles (Figure 2-6d). The current-time (*i-t*) responses for the sample electrodes clearly demonstrate current densities depending on cycle times. Together with current and potential values, the overall performance of PNP/DAB-MWCNT can be comparable with that of the optimized and commercially available Vulcan XC-72R.

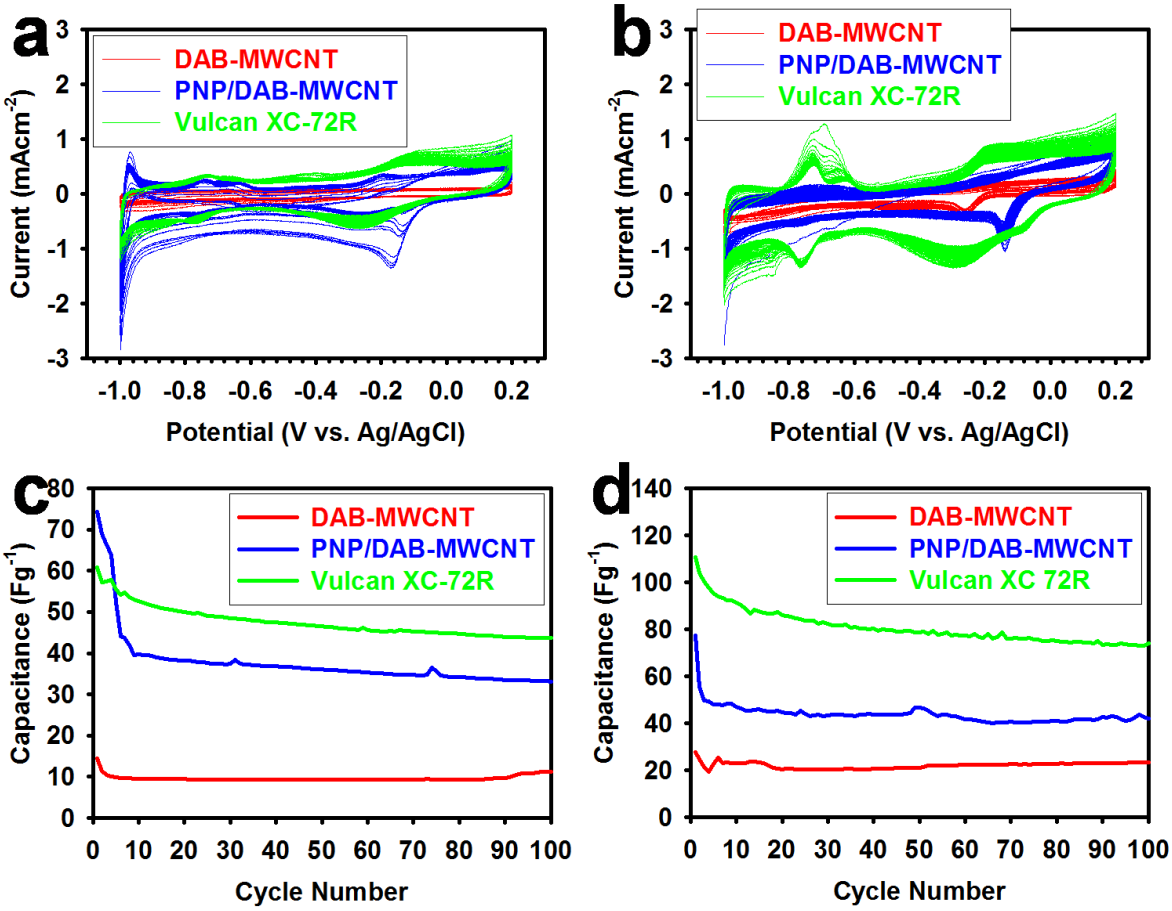

Figure 2-6. CV curves of DAB-MWCNT/GC, PNP/DAB-MWCNT/GC and Vulcan-72R/GC electrodes in 0.1 M aqueous KOH solution with a scan rate of 10 mVs^{-1}: (a) N_2-saturated medium; (b) O_2-saturated medium. Electrochemical stability measurements of sample electrodes by using sequential CV in (c) N_2-saturated medium; (d) O_2-saturated medium.

In order to obtain an important electrocatalytic parameter during the ORR process, the reaction kinetics were investigated by rotating disk voltammetry (Figure 2-7a). The voltammetric profiles showed that the current density was increased by increasing rotating rate. The onset potential of PNP/DABMWCNT/GC for ORR was about -0.12 V, which is close to that identified from CV

measurements (Figure 2-7b). The corresponding Koutecky–Levich curves at different electrode potentials revealed parallel plots with a good linearity (Figure 2-7b), which are often taken as an indication of first-order reaction kinetics with respect to the concentration of dissolved O_2.[37] The kinetic parameters can be analyzed on the basis of the Koutecky–Levich equation.[38] The transferred electron numbers per oxygen molecule involved in the oxygen reduction are 3.94, 3.91, and 3.89 at -0.4, -0.5, and -0.6 V, respectively, suggesting that the PNP/DAB-MWCNT leads to an efficient four-electron transfer in ORR process.

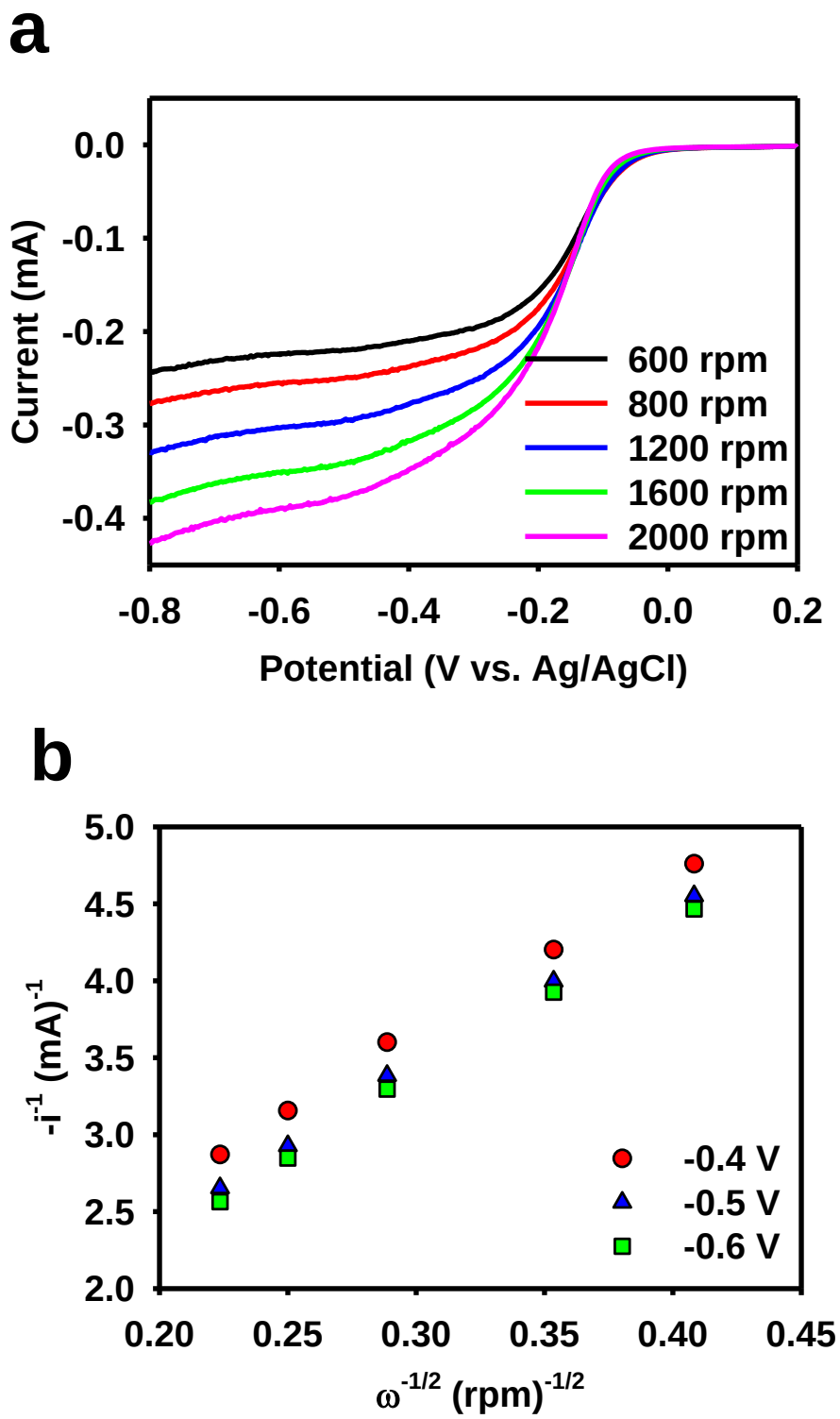

Figure. 2-7 a Rotating disk electrode (RDE) voltammograms of PNP/DAB-MWCNT/GC electrodes in an O_2-saturated 0.1 M aq. KOH solution with at different rotate rates of 600, 800, 1,200, 1,600, and 2,000 rpm. b Koutecky–Levich plots of the PNP/DAB-MWCNT derived from RDE measurements at different electrode potentials.

2.9 Conclusions

MWCNT was functionalized with 3,4-diaminobenzoic acid (DABA) *via* a "direct" Friedel-Crafts acylation in a mildly acidic PPA/P_2O_5 medium. The resultant DAB-MWCNT was thoroughly characterized with EA, FT-IR, UV-vis, TGA, XRD, SEM, and TEM. The results showed that DAB moiety was introduced well onto the surface of DAB-MWCNT. In addition, XRD results showed that persisting metallic impurities in pristine MWCNT were mostly removed at the same time. The resultant DAB-MWCNT was used to support PNP to prepare a PNP/DAB-MWCNT hybrid, which was characterized, and an efficient deposition of PNP on DAB-MWCNT was confirmed. The morphology of the PNP/MB-MWCNT hybrid was studied with SEM and TEM, showing that PNP were uniformly distributed on the surface of DAB-MWCNT. Compared to DAB-MWCNT, the PNP/DAB-MWCNT hybrid displayed distinct redox peaks with much higher electrocatalytic activity and lower activation barrier. The results suggest a new design of PNP/MWCNT-based electrocatalysts for energy conversion applications.

2.10 References

(1) Tasis D., Tagmatarchis N., Bianco A., Prato M. Chemistry of carbon nanotubes. Chem. Rev. 2006, 106, 1105–1136.

(2) Carneiro O., Covas J., Bernardo C., Caldeira G., Van Hattum F., Ting J.M., Alig R., Lake M. Production and assessment of polycarbonate composites reinforced with vapour-grown carbon fibres. Compos. Sci. Technol. 1998, 58, 401–407.

(3) Lee S.Y., Yamada M., Miyake M. Synthesis of carbon nanotubes over gold nanoparticle supported catalysts. Carbon 2005, 43, 2654–2663.

(4) Shi Y., Yang R., Yuet P.K. Easy decoration of carbon nanotubes with well dispersed gold nanoparticles and the use of the material as an electrocatalyst. Carbon 2009, 47, 1146–1151.

(5) Alexeyeva N., Matisen L., Saar A., Laaksonen P., Kontturi K., Tammeveski K. Kinetics of oxygen reduction on gold nanoparticle/multi-walled carbon nanotube hybrid electrodes in acid media. J. Electroanal. Chem. 2010. 642, :6–1.2

(6) Yu R., Chen L., Liu Q., Lin J., Tan K.L., Ng S.C., Chan H.S.O., Xu G.Q., Hor T.S.A. Platinum deposition on carbon nanotubes via chemical modification. Chem. Mater. 1998, 10, 718–722.

(7) Xue B., Chen P., Hong Q., Lin J., Tan K.L. Growth of Pd, Pt, Ag and Au nanoparticles on carbon nanotubes. J. Mater. Chem. 2001, 11, 2378–2381.

(8) Li W., Liang C., Zhou W., Qiu J., Zhou Z., Sun G., Xin Q. Preparation and characterization of multiwalled carbon nanotube-supported platinum for cathode catalysts of direct methanol fuel cells. J. Phys. Chem. B 2003, 107, 6292–6299.

(9) Lorencon E., Ferlauto A.S., de Oliveira S., Miquita D.R., Resende R.R., Lacerda R.G., Ladeira L.O. Direct production of carbon nanotubes/metal nanoparticles hybrids from a redox reaction between metal ions and reduced carbon nanotubes. ACS Appl. Mater. Interfaces 2009. 1, 2104–2106.

(10) Li J., Moskovits M., Haslett T.L. Nanoscale electroless metal deposition in aligned carbon nanotubes. Chem. Mater. 1998, 10, 1963–1967.

(11) Kim S.N., Slocik J.M., Naik R.R. Strategy for the assembly of carbon nanotube-metal nanoparticle hybrids using biointerfaces. Small 2010, 6, 1992–199.5

(12) Shaffer M.S.P., Windle A.H. Fabrication and characterization of carbon nanotube/poly (vinyl alcohol) composites. Adv. Mater. 1999, 11, 937–941.

(13) Chen G.Z., Shaffer M.S.P., Coleby D., Dixon G., Zhou W., Fray D., Windle A. Carbon nanotube and polypyrrole composites: coating and doping. Adv. Mater. 2000, 12, 522–526.

(14) Sun Y.P., Fu K., Lin Y., Huang W. Functionalized carbon nanotubes: properties and applications. Acc. Chem. Res. 2002, 35, 1096–1104.

(15) Dai L., Mau A.W.H. Controlled synthesis and modification of carbon nanotubes and C 60: carbon nanostructures for advanced polymeric composite materials. Adv. Mater. 2001, 13, 899–913.

(16) Hirsch A. Functionalization of single walled carbon nanotubes. Angew. Chem. Int. Ed. 2002, 41,1853–1859.

(17) Zhang Y., Shi Z., Gu Z., Iijima S. Structure modification of single-wall carbon nanotubes. Carbon 2000, 38, 2055–2059.

(18) Huang W., Lin Y., Taylor S., Gaillard J., Rao A.M., Sun Y.P. Sonication-assisted functionalization and solubilization of carbon nanotubes. Nano Lett. 2002, 2, 231–234.

(19) Heller D.A., Barone P.W., Strano M.S. Sonication-induced changes in chiral distribution: a complication in the use of single-walled carbon nanotube fluorescence for determining species distribution. Carbon 2005, 43, 651–653.

(20) Wildgoose G.G., Banks C.E., Compton R.G. Metal nanoparticles and related materials supported on carbon nanotubes: methods and applications. Small 2006, 2, 182–193.

(21) Han S.W., Oh S.J., Tan L.S., Baek J.B. One-pot purification and functionalization of single-walled carbon nanotubes in lesscorrosive poly (phosphoric acid). Carbon 2008, 46, 1841–1849.

(22) Lee H.J., Han S.W., Kwon Y.D., Tan L.S., Baek J.B. Functionalization of multi-walled carbon nanotubes with various 4-substituted benzoic acids in mild polyphosphoric acid/phosphorous pentoxide. Carbon 2008, 46, 1850–1859 .

(23) Baek J.B., Lyons C.B., Tan L.S. Covalent modification of vapour-grown carbon nanofibers via direct Friedel–Crafts acylation in polyphosphoric acid. J. Mater. Chem. 2004, 14, 2052–2056.

(24) Eo S.M., Oh S.J., Tan L.S., Baek J.B. Poly (2,5-benzoxazole)/carbon nanotube composites via in situ polymerization of 3-amino-4-hydroxybenzoic acid hydrochloride in a mild poly (phosphoric acid). Eur. Polym. J. 2008, 44,1603–1612.

(25) Wolfe J.F. Polybenzothiazoles and polybenzoxazoles. In Encyclopedia of polymer science and engineering, 2nd edn. Wiley, New York 1988, 11, 601–635.

(26) Mandal S., Roy D., Chaudhari R.V., Sastry M. Pt and Pd nanoparticles immobilized on amine-functionalized zeolite: excellent catalysts for hydrogenation and heck reactions. Chem. Mater. 2004, 16, 3714–3724.

(27) Ahmadi T.S., Wang Z.L., Green T.C., Henglein A., El-Sayed M.A. Shape-controlled synthesis of colloidal platinum nanoparticles. Science 1996, 272, 1924.

(28) Hu H., Zhao B., Itkis M.E., Haddon R.C. Nitric acid purification of single-walled carbon nanotubes. J. Phys. Chem. B .2003, 107, 13838–13842.

(29) Jeon I.Y., Lee H.J., Choi Y.S., Tan L.S., Baek J.B. Semimetallic transport in nanocomposites derived from grafting of linear and hyperbranched poly (phenylene sulfide) s onto the surface of functionalized multi-walled carbon nanotubes. Macromolecules 2008, 41, 7423–7432.

(30) Charlier J.C. Defects in carbon nanotubes. Acc. Chem. Res. 2002, 35, 1063–1069

(31) Koizumi T., Fukuju K. Cyclometalated platinum (II) complexes bearing o-phenylenediamine derivatives: synthesis and electrochemical behavior. J. Organomet. Chem. 2010, 696,1232–1235.

(32) Lahiff E., Leahy R., Coleman J.N., Blau W.J. Physical properties of novel free-standing polymer-nanotube thin films. Carbon 2006, 44, 1525–1529.

(33) Zhou C., Wang S., Zhuang Q., Han Z. Enhanced conductivity in polybenzoxazoles doped with carboxylated multiwalled carbon nanotubes. Carbon 2008, 46, 1232–1240.

(34) Yano H., Inukai J., Uchida H., Watanabe M., Babu P.K., Kobayashi T., Chung .JH., Oldfield E., Wieckowski A. Particlesize effect of nanoscale platinum catalysts in oxygen reduction reaction: an electrochemical and 195Pt EC-NMR study. Phys. Chem. Chem. Phys. 2006, 8, 4932–4939.

(35) Laviron E. General expression of the linear potential sweep voltammogram in the case of diffusionless electrochemical systems. J. Electroanal. Chem. 1979, 101,19–28.

(36) Laviron E. The use of linear potential sweep voltammetry and of ac voltammetry for the study of the surface electrochemical reaction of strongly adsorbed systems and of redox modified electrodes. J. Electroanal. Chem. 1979, 100, 263–270.

(37) Bard A.J., Faulkner L.R. Electrochemical methods, fundamentals and applications. Wiley, New York, 2001.

(38) Tammeveski K., Tenno T., Claret J., Ferrater C Electrochemical reduction of oxygen on thin-film Pt electrodes in 0.1 M KOH. Electrochim. Acta 1997, 42, 893–897.

Chapter III. Facile, scalable synthesis of edge-halogenated graphene nanoplatets as efficient metal-free electrocatalysts for oxygen reduction reaction

Note: This chapter is partially and totally adapted with permission from "Facile, scalable synthesis of edge-halogenated graphene nanoplatets as efficient metal-free electrocatalysts for oxygen reduction reaction", Scientific Reports 2013, 3, 1810. Copyright ⓒ 2013 Nature Publishing Group.

3.1 Abstract

A series of edge-selectively halogenated (X = Cl, Br, I) graphene nanoplatelets (XGnPs = ClGnP, BrGnP, IGnP) were prepared simply by ball-milling graphite in the presence of Cl_2, Br_2 and I_2, respectively. High BET surface areas of 471, 579 and 662 m^2/g were observed for ClGnP, BrGnP and IGnP, respectively, indicating a significant extent of delamination during the ball-milling and subsequent workup processes. The newly-developed XGnPs can be well dispersed in various solvents, and hence are solution processable. Furthermore, XGnPs showed remarkable electrocatalytic activities toward oxygen reduction reaction (ORR) with a high selectivity, good tolerance to methanol crossover/CO poisoning effects, and excellent long-term cycle stability. First-principle density-functional calculations revealed that halogenated graphene edges could provide decent adsorption sites for oxygen molecules, in a good agreement with the experimental observations.

3.2 Introduction

One of the major huddles for commercialization of the fuel cell technology is the sluggish oxygen reduction reaction (ORR) at cathode[1-3]. So far, high cost and scarce precious platinum (Pt) and its alloys have been considered to be the most reliable cathodic ORR electrocatalysts in fuel cells[4-8]. In addition to the high cost, however, Pt and its alloys are also suffered from methanol crossover/carbon monoxide (CO) poisoning effects and poor operation stability. Therefore, it is essential to search for non-precious metal[9-11] or metal-free[12-17] electrocatalysts with a high catalytic activity and long-term operation stability to reduce or replace Pt-based ORR electrocatalysts in fuel cells. Although extensive efforts have been devoted to the development of non-precious metal-based electrocatalysts, their practical application is still out of sight due largely to their limited electrocatalytic activity, poor cycle stability and sometimes environmental hazard.

Recently, carbon-based materials doped with heteroatoms, such as boron (B)[14,18], iodine (I)[19], nitrogen (N)[15,20-24], phosphorus (P)[25], sulfur (S)[26], and their mixtures[27-29], have attracted tremendous attentions as metal-free ORR eletrocatalysts. The difference in electronegativity (χ) between the

heteroatom dopants (B = 2.04, I = 2.66, N = 3.04, P = 2.19 and S = 2.58) and carbon atom (2.55)[30] in covalently doped graphitic carbon frameworks can polarize adjacent carbon atoms. Indeed, quantum mechanics calculations revealed that the electron accepting/donating ability of the heteroatom dopants created net positive/negative charges on adjacent carbon atoms in graphitic lattice to facilitate the oxygen reduction process[12]. Thus, both the vertically-aligned nitrogen-doped carbon nanotubes (VA-NCNTs)[12] and nitrogen-doped graphene (N-graphene)[24] catalyzed an efficient four-electron ORR process with a higher electrocatalytic activity and better operation stability than the commercially available Pt/C-based electrocatalyst (Pt: 20 wt%, Vulcan XC-72R). Furthermore, the excellent stability over the methanol crossover/CO poisoning effects is additional advantage of these carbon-based metal-free catalysts. Although the basic catalytic mechanism has been established, the full potential of these carbon-based, metal-free catalysts is hard to achieve without the synthetic capability for large-scale production of the heteroatom-doped, carbon-based materials at low cost. However, commonly affordable chemical vapor deposition (CVD)[14] and/or Hummers' methods are too expensive and involve environmentally hazardous reagents, and thus inappropriate for large-scale production[31].

In this study, we have, for the first time, synthesized a series of edge-selectively halogenated (Cl, Br and I) graphene nanoplatelets (ClGnP, BrGnP and IGnP; collectively designated as XGnPs) by simply ball-milling graphite flake[32,33] in the presence of chlorine (Cl_2), bromine (Br_2) or iodine (I_2), respectively. Since fluorine (F_2) gas is too reactive and toxic to be handled in normal laboratories (serious cautions!)[34,35], edge-fluorinated GnP (FGnP) could not be prepared for this study. Although the electronegativities of halogen atoms are in the order of Cl (3.16) > Br (2.96) > I (2.66), the experimentally observed electrocatalytic activities for ORR are in the order of IGnP > BrGnP > ClGnP. Compared to the pristine graphite and commercially available Pt/C electrocatalyst, IGnP exhibited much better electrocatalytic performances for ORR with an excellent long-term durability and tolerance to methanol crossover/CO poisoning effects. The density-functional theory (DFT) calculations revealed that certain particular types of halogenated edges showed desirable binding affinity with oxygen (O_2) molecules. In consistency with the experimental observations, the charge-transfer induced weakening of the O-O bond strength was most prominent for the case of IGnP.

3.3 Syntehsis of XGnPs

XGnPs were prepared simply by ball-milling the pristine graphite in a planetary ball-mill capsule in the presence of Cl_2, Br_2 and I_2, respectively. In a typical experiment, the pristine graphite (5.0 g) was placed into a stainless steel capsule containing stainless steel balls (500 g, diameter 5 mm). The capsule was then sealed and degassed by five cycles of charging and discharging argon after applying

reduced pressure (0.05 mmHg). Thereafter, Cl_2 gas was charged through a gas inlet with cylinder pressure of 8.75 atm. The capsule was then fixed in the planetary ball-mill machine, and agitated with 500 rpm for 48h. The resultant product was Soxhlet extracted with methanol to get rid of small molar mass organic impurities and 1 M aq. HCl solution to remove metallic impurities, if any. Final product was then freeze-dried at -120 ℃ under a reduced pressure (0.05 mmHg) for 48h to yield 6.09 g (ClGnP has at least 1.09 g of Cl uptake) of dark black ClGnP powder. BrGnP (6.93 g, 1.93 g of Br uptake) and IGnP (6.86 g, 1.86 g of I uptake) samples were also prepared following the similar ball-milling and work-up procedures.

3.4 Instrumentation

Fourier transform infrared (FTIR) spectra were recorded on Perkin-Elmer Spectrum 100 using KBr disks. Themogravimetric analysis (TGA) was conducted on a TA Q200 (TA Instrument) under nitrogen at a heating rate of 10 °C/min. The surface area was measured by nitrogen adsorption-desorption isotherms using the Brunauer-Emmett-Teller (BET) method on Micromeritics ASAP 2504N. The field emission scanning electron microscopy (FE-SEM) was performed on FEI Nanonova 230 while the high-resolution transmission electron microscopy (HR-TEM) was carried out on a JEOL JEM-2100F (Cs) microscope operating at 200 kV. The TEM specimen were prepared by dipping carbon micro-grids (Ted Pella Inc., 200 Mesh Copper Grid) into well-dispersed samples in ethanol. X-ray photoelectron spectra (XPS) were recorded on a Thermo Fisher K-alpha XPS spectrometer. Elemental analysis (EA) was conducted with Thermo Scientific Flash 2000. Zeta-potential values were determined using a Malvern Zetasizer (Nano ZS, Malvern Instruments). X-Ray diffraction (XRD) patterns were recorded with a Rigaku D/MAZX 2500V/PC with Cu–Kα radiation (35 kV, 20 mA, λ = 1.5418 Å). Raman spectra were taken with a He-Ne laser (532 nm) as the excitation source by using confocal Raman microscopy (Alpha 300S, WITec, Germany), in conjunction with atomic force microscopy (AFM).

3.5 Electrochemical measurements

The electrochemical tests were carried out using a computer-controlled potentiostat (1470E Cell Test System, Solartron Analytical, UK) with a typical three-electrode cell. A platinum wire was used as a counter-electrode and an Ag/AgCl (3 M KCl filled) electrode as the reference electrode. All the experiments were conducted at ambient condition. The working electrodes were prepared by applying respective catalyst inks onto the prepolished glassy carbon (GC) disk electrodes. Briefly, samples were dispersed in ethanol and ultrasonicated for 15 min to form uniform catalyst inks (2 mg mL^{-1}). A total of 7.5 µL of a well-dispersed catalyst ink was applied onto a pre-polished glassy carbon (GC)

disk electrode (5 mm in diameter). After drying at room temperature, Nafion (0.05 wt%) stock solution (5 μL) in ethanol was applied onto the surface of the catalyst layer to form a thin protective film. The addition of a small amount of Nafion could effectively improve the dispersion of catalyst suspension. The electrodes thus prepared were dried at room temperature overnight prior to the electrochemical tests. The detailed kinetic analysis was conducted according to Koutecky-Levich plots:

$$\frac{1}{j} = \frac{1}{j_k} + \frac{1}{B\omega^{0.5}} \quad (1)$$

where j_k is the kinetic current and B is Levich slope which is given by:

$$B = 0.2nF(D_{O_2})^{2/3}\nu^{-1/6}C_{O_2} \quad (2)$$

Here n is the number of electrons transferred in the reduction of one O_2 molecule, F is the Faraday constant (F = 96485 C/mol), D_{O2} is the diffusion coefficient of O_2 (D_{O2} =1.9×10^{-5} cm^2 s^{-1}), ν is the kinematics viscosity for KOH (v = 0.01 cm^2 s^{-1}) and C_{O2} is concentration of O_2 in the solution (C_{O2} = 1.2 × 10^{-6} mol cm^{-3}). The constant 0.2 is adopted when the rotation speed is expressed in rpm. According to equations (1) and (2), the number of electrons transferred (n) can be obtained from the slope of Koutecky-Levich plot of i^{-1} *vs.* $\omega^{-1/2}$. From published data[2, 3] for F (96485 C mol^{-1}), D_{O2} (1.9×10^{-5} cm^2 s^{-1}), υ (0.01 cm^2 s^{-1}), and C_{O2} (1.2 ×10^{-6} mol cm^{-3}), B is calculated to be 0.144 mA s$^{-1/2}$ at A=0.19625 cm^2 for a four-electron exchange reaction (n = 4).

3.6 DFT calculations

For computations, we used the Vienna Ab initio Simulation Package(VASP) to calculate the ground state of many electrons system in the frame work of density functional theory. The plane-wave basis set with an energy cut-off of 400 eV and the PBE-type gradient-corrected exchange-correlation potential were employed.

3.7 Results and Discussion

The ball-milling-driven mechanochemical reaction between active carbon species and halogens is schematically shown in Figure 1a. Briefly, the high speed rotation (500 rpm) of the stainless steel balls during ball milling generated sufficient kinetic energy to cause bond cleavages for the graphitic C-C framework (Figure 3-1b). As a result, active carbon species (mostly carboradicals, carbocations and carbanions)[36] formed at the broken edges of graphite, which were sufficiently reactive to pick up

halogens (*e.g.*, Cl_2, Br_2, I_2) in the sealed ball-mill capsule. The detailed mechanism is proposed in Figure 3-2. The high reactivity of the active carbon species was indicated by violent sparkling observed when capsule lid was opened (Figures 3-1c, 3-1d), presumable due to the termination reaction for the remnants of the active carbon species with air moisture.

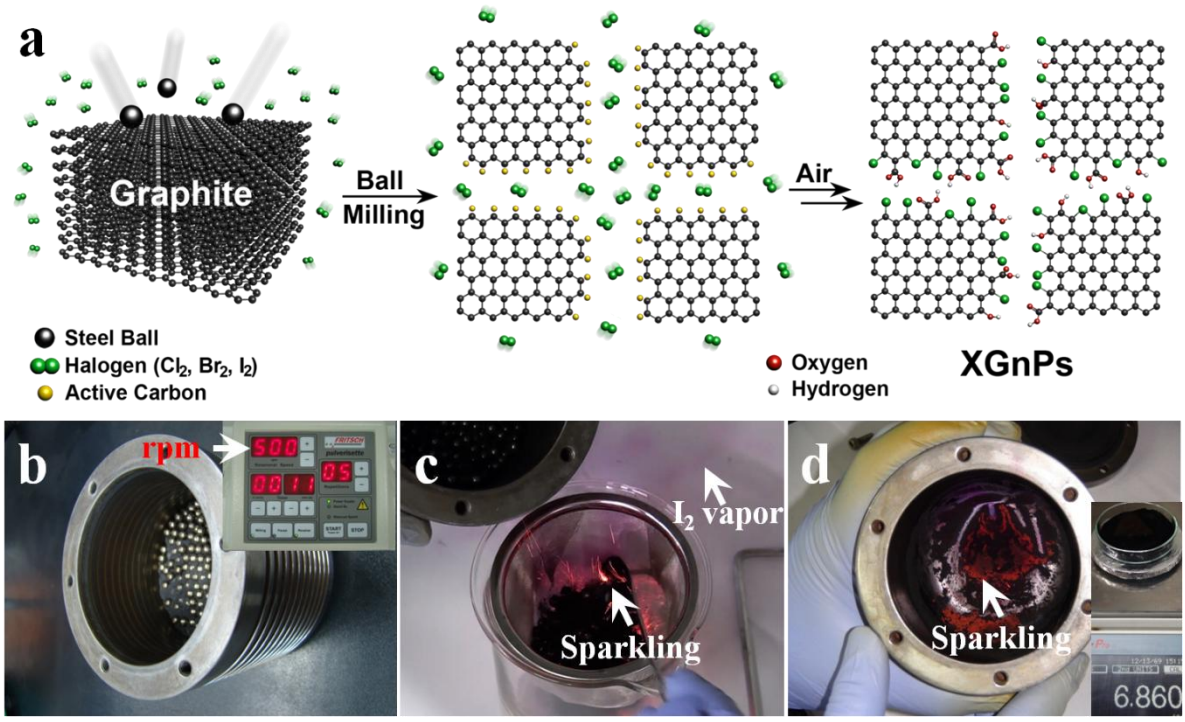

Figure 3-1. (a) A schematic representation for mechanochemically driven edge-halogenation reaction between the *in-situ* generated active carbon species (gold balls) and reactant halogens (twin green balls). Active carbon species were generated by homolytic bond cleavages of graphitic C-C bonds and reacted with halogen molecules to produce edge-halogenated graphene nanoplatelets (XGnPs) in a sealed ball-mill capsule and the remnant active carbon species are terminated upon subsequent exposure to air moisture. Red and gray balls stand for oxygen and hydrogen, respectively; (b) ball-mill capsule containing the pristine graphite and stainless steel balls (diameter 5 mm); (c) violent sparkling (red spots) occurred when the reaction mixture was exposed to ambient air moisture and excess purple I_2 was sublimated in the air (arrow); (d) continued sparkling from residual IGnP at the bottom of a ball-mill capsule even after most of the IGnPs and stainless balls were taken out.

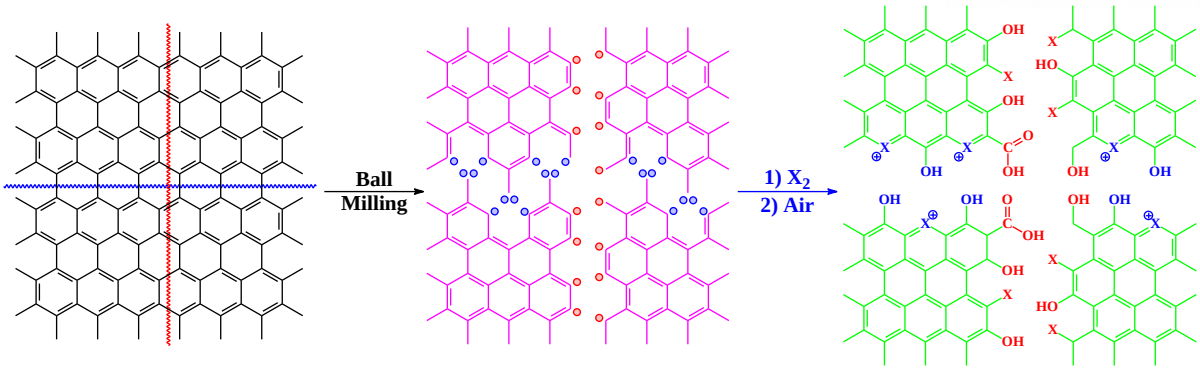

Figure 3-2. Schematic representation of the edge-selective halogenation of graphite by ball-milling in the presence of halogens, such as chlorine (Cl_2), bromine (Br_2) and iodine (I_2) to produce edge-chloro- (ClGnP), edge-bromo- (BrGnP) and edge-iodo-graphene nanoplatelets (IGnP), respectively. The graphitic structures are simplified for clarity. The red and blue lines represent armchair and zigzag cuts, respectively, resulting in the red and blue dots as active carboradicals. The active carbon species are (1) reacted with halogen molecules and (2) subsequently terminated by air moisture upon opening ball-mill capsule lid to produce the edge-halogenated graphene nanoplatelets.

Scanning electron microscopy (SEM) images show an obvious size reduction from a large grain size of ~150 μm for the pristine graphite (Figure 3-3a) to a much smaller grain size of < 1 μm for XGnPs (Figures 3-3b-3-3d) by ball-milling. The size reduction implies C-C bond breakings in the graphitic structures, and thus *in-situ* generation of active carbon species to react with halogens. The presence of Cl, Br and I in the resultant XGnPs are clearly evident by energy dispersive X-ray (EDX) spectroscopic (Figure 3-3e) measurements with element mapping (Figure 3-4 and Table 3-2) and elemental analysis (EA) (Table 3-1).

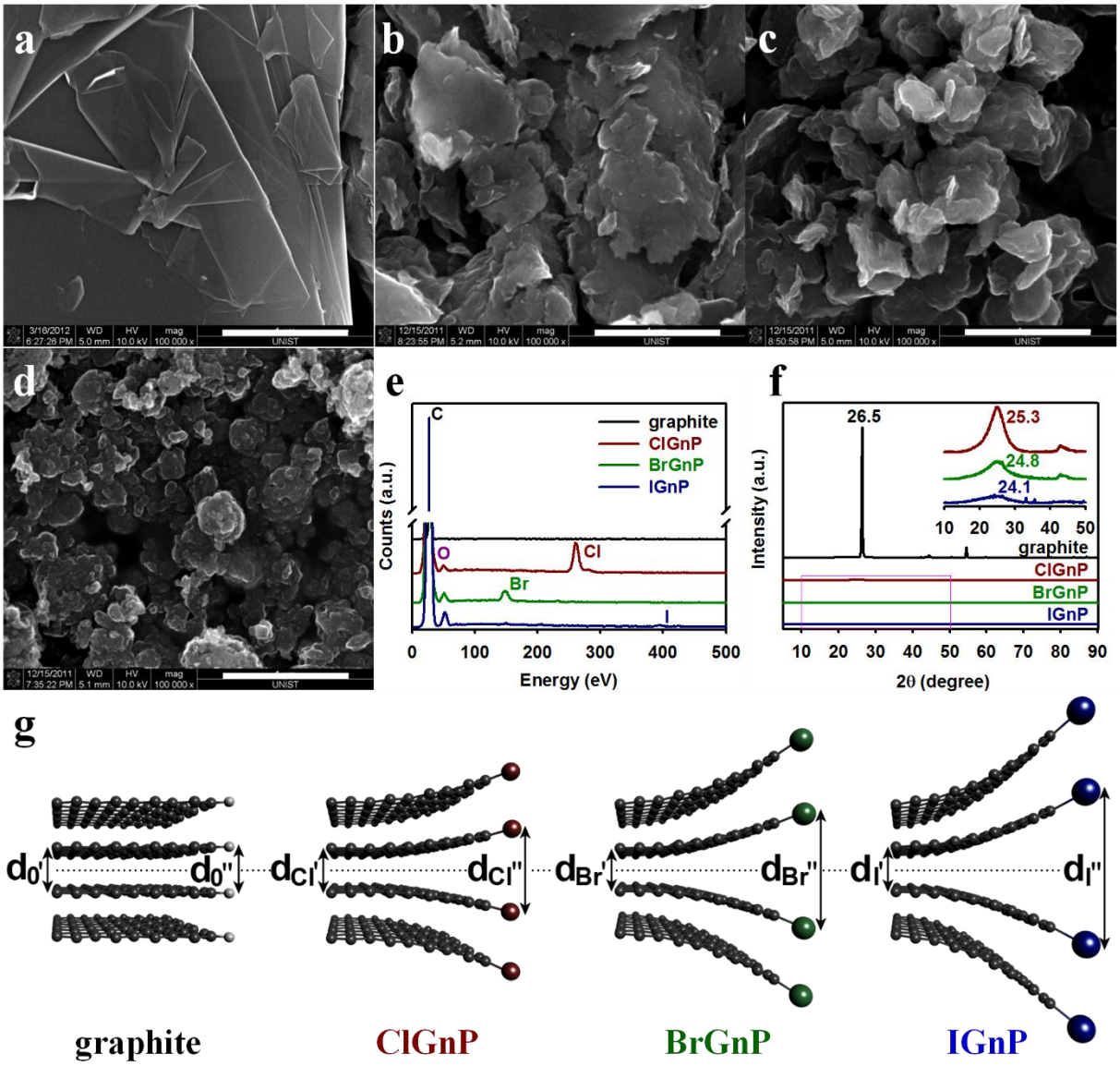

Figure 3-3. SEM images: (a) the pristine graphite with average grain size ~150 μm. The average grain sizes of XGnPs reduced to less than 1 μm: (b) ClGnP; (c) BrGnP; (d) IGnP. Scale bars are 1 μm. (e) EDX spectra. (f) XRD diffraction patterns. Inset is magnified XRD diffraction patterns from the pink rectangle. The relative [002] peak intensities of XGnPs are less than 0.4% of that of the pristine graphite, indicating that the great extent of graphite has been deliminated into edge-halogenated graphene nanoplatelets (XGnPs). (g) A schematic representation for the edge expansions of XGnPs caused by the edge-halogens.

Table 3-1. EA data of the pristine graphite and XGnPs

Sample	C (%)	H (%)	O (%)	C/O
graphite	99.64	BDL[a]	0.13	1021
ClGnP	78.62	0.30	3.40	30.8
BrGnP	74.24	0.44	5.29	20.0
IGnP	77.51	0.79	9.11	11.3

a. BDL = Below detection limit.

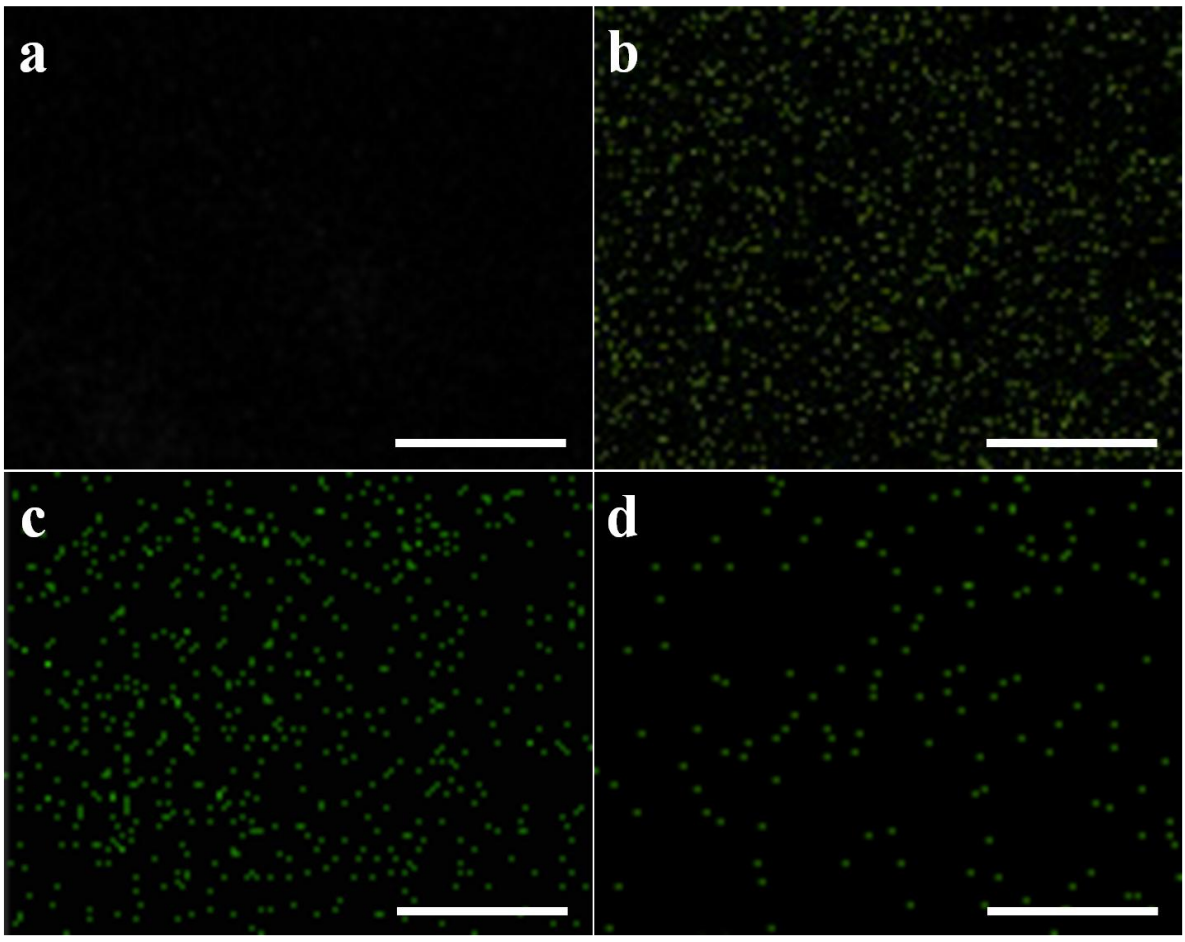

Figure 3-4. EDX (FE-SEM) element mappings of samples: (a) the pristine graphite with halogen mapping; (b) ClGnP with chlorine mapping; (c) BrGnP with bromine mapping; (d) IGnP with iodine mapping. Scale bars are 250 nm.

Table 3-2. XPS, EDX, and TGA data of the pristine graphite and XGnPs

Sample	Element	XPS	EDX (SEM)	TGA (Char % yield in N_2)	
				at 800 ℃	at 1000 ℃
graphite	C (%)	98.35	98.80	99.7	99.1
	O (%)	1.65	1.20		
	C/O	59.6	82.3		
ClGnP	C (%)	89.78	93.06	85.9	81.2
	O (%)	4.33	1.82		
	Cl (%)	5.89	5.12		
	C/O	20.7	51.1		
	C/Cl	45.0	53.6		
BrGnP	C (%)	88.05	94.26	71.4	69.1
	O (%)	9.17	4.45		
	Br (%)	2.78	1.29		
	C/O	9.6	21.2		
	C/Br	210.7	486.1		
IGnP	C (%)	89.24	95.49	75.4	72.7
	O (%)	9.81	5.04		
	I (%)	0.95	0.46		
	C/O	9.1	18.9		

	C/I	992.5	2165.0

a. BDL = Below detection limit or not available.

b. NA = Not applicable.

XRD diffraction patterns are shown in Figure 2f. As can be seen, the pristine graphite exhibited a typical strong [002] peak at 26.5°, corresponding to an interlayer *d*-spacing of 0.34 nm[37]. In contrast, all XGnPs displayed less than 0.4% of the [002] peak intensity characteristic of the pristine graphite, suggesting a high degree of exfoliation occurred during the ball-milling and subsequent work-up processes. Unlike graphite oxide (GO) with a large parallel shift of the [002] peak to as low as 10.5° (*d*-spacing of 0.83 nm)[38], XGnPs showed a dramatic decrease in the peak intensity while maintaining the peak location close to 26.5°, indicating that the great extent of graphitic layers were delaminated into XGnPs without much lattice expansion or basal plane damage. As atomic size decreased in the order of I > Br > Cl (Figure 3-3g), the peaks (*d*-spacing) appear at 25.3 (0.35 nm), 24.8 (0.36 nm) and 24.1° (0.37 nm) for ClGnP, BrGnP and IGnP, respectively (Figure 3-3f, inset). The average number of layers in the delaminated graphite by ball-milling could be estimated on the basis of surface area of XGnPs. Given that the maximum BET surface of single layer graphene is 2630 m^2/g[39], the average layer numbers of the XGnP samples could be calculated by simply dividing the maximum surface area by experimentally determined BET surface areas of the XGnPs (Table 3-3). Because the edge contribution of the graphene nanoplatelets (GnPs) is negligible in respect to the basal area, the estimated average numbers of the delaminated graphitic layers are 5.6 (2630/471), 4.5 (2630/579) and 4.0 (2630/662) for ClGnP, BrGnP and IGnP, respectively. Hence, the ball-milling process involves not only mechanochemically cracking graphitic C-C bonds and edge-selectively functionalizing graphitic layers, but also delaminating graphite into GnPs. The XGnPs could be further exfoliated into even fewer-layered GnPs *via* edge-opening upon dispersion in various polar solvents (Figures 3-5a-3-5c). Zeta-potential data for the XGnPs at different concentrations in DMF (Figures 3-5d and 3-5e) are in the range of -31.6 – -38.7 mV, indicating the formation of stable dispersions as an absolute Zeta-potential value larger than 30 mV can ensure a stable dispersion *via* either positive or negative charge repulsion (Table 4-4)[40]. Thus, the Zeta-potential measurements, together with microscopic (see Figures 3-3a-3-3d) and spectroscopic studies (see Figures 3-3e and 3-3f), indicate that the driving force for the good dispersion stability must be originated from the size reduction (entropic contribution) and the steric repulsion between the halogen groups at the edges (enthalpic contribution, Figure 3-3g)[41].

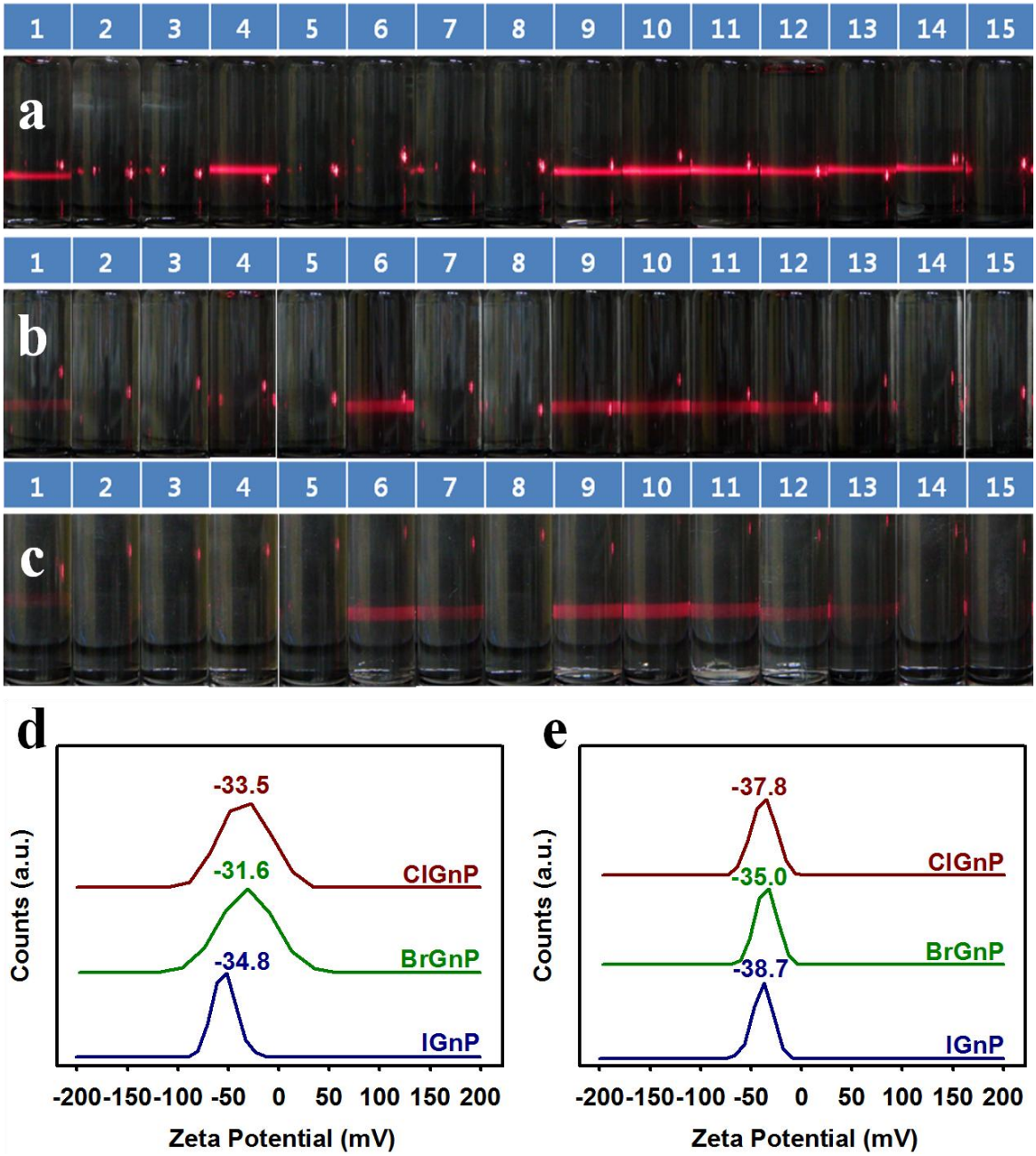

Figure 3-5. Photographs of XGnPs dispersed solutions in various solvents after one week standing on bench top in the normal laboratory condition: **(a)** ClGnP; **(b)** BrGnP; **(c)** IGnP. Zeta-potentials of XGnPs in DMF at different concentrations: **(d)** 0.10 mg/mL; **(e)** 0.04 mg/mL. The solvents used in this study are: (1) H_2O; (2) 1M HCl; (3) 1M KOH; (4) diethyl ether (5) MeOH; (6) EtOH; (7) THF; (8) acetone; (9) DMAc; (10) DMF; (11) NMP; (12) dichloromethane; (13) dichlorobenzene; (14) benzene; (15) CS_2.

Typical TEM images (Figures 3-6~3-8) with selected area electron diffraction (SAED) patterns (insets, Figures 3-6a, 3-7a and 3-8a) of XGnPs show flake-like morphology with ordered structures at the basal planes and some structural distortions at the edges (insets, Figures S4d, S5d and S6d). Once again, these results confirm the edge-selective halogenations of GnPs by ball-milling with minimal alteration of their basal planes. Element mappings of multilayer XGnPs through the bulk thickness further confirm the presence of halogen heteroatoms in XGnPs (Figures 3-6e-3-6g, 3-7e-3-7g and 3-8e-3-8g).

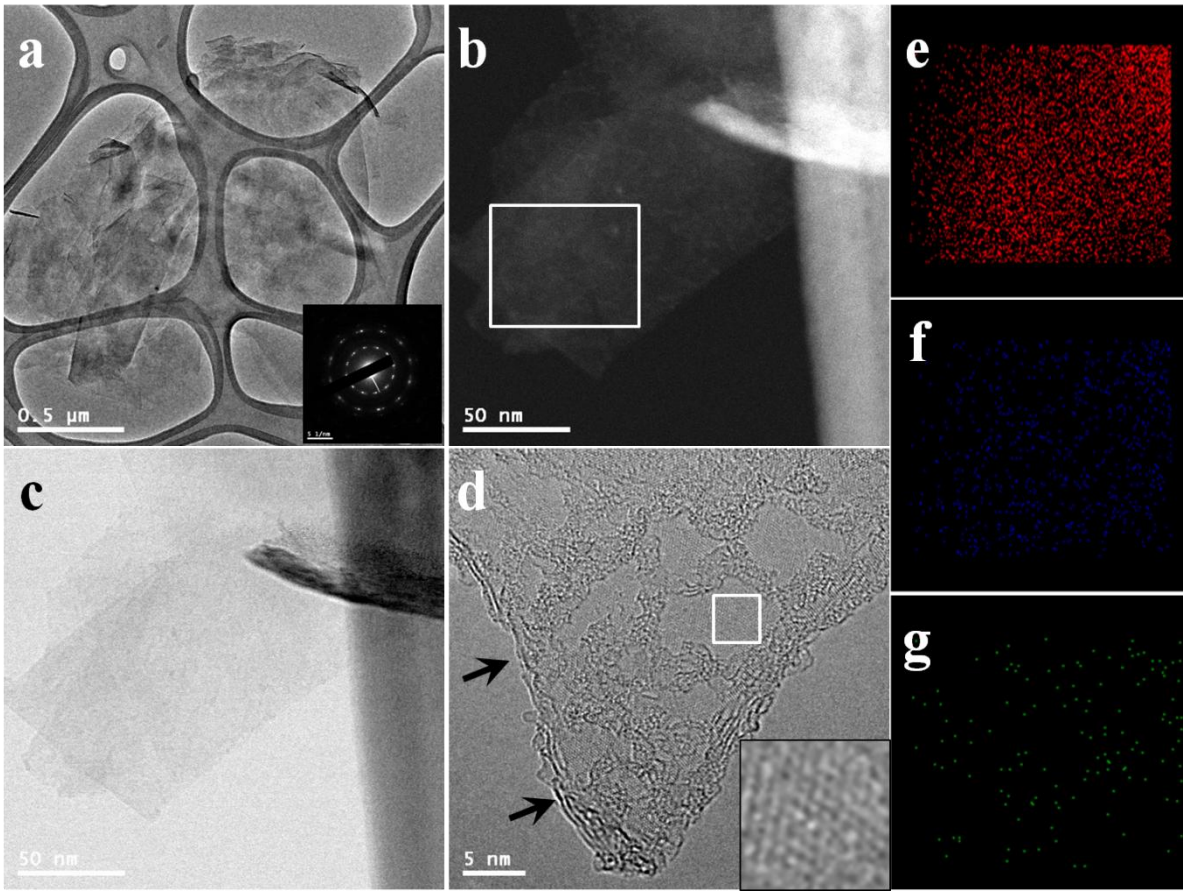

Figure 3-6. TEM images of ClGnP: (a) bright field (BF) image. Inset is the selected area electron diffraction (SAED) pattern; (b, c) energy-filtered images; (d) high-resolution image of 2-3 graphitic layers (arrows) with honeycomb lattice image (inset), indicating high crystallinity. EDX (HR-TEM) element mappings from rectangle in (b): (e) carbon; (f) oxygen; (g) chlorine.

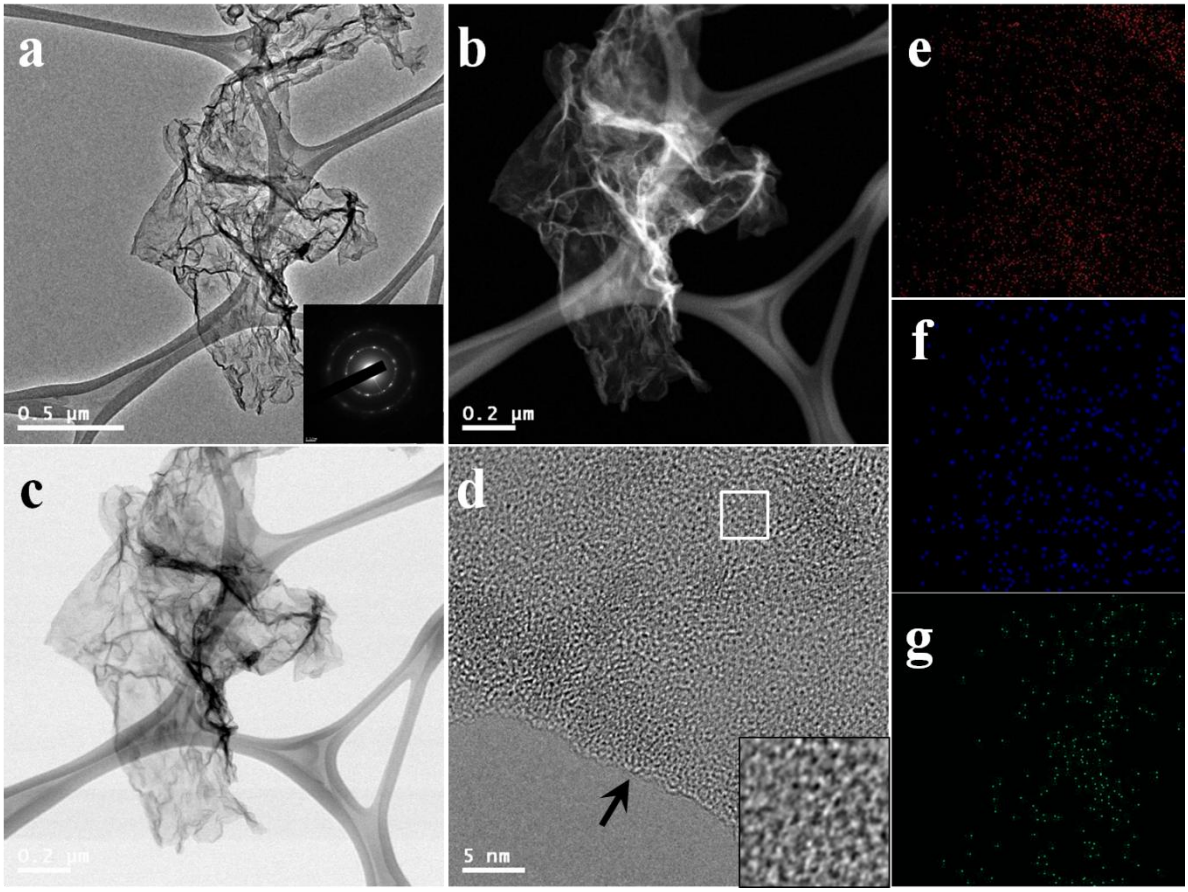

Figure 3-7. TEM images of BrGnP: (a) bright field (BF) image. Inset is the selected area electron diffraction (SAED) pattern; (b, c) energy-filtered images; (d) high-resolution image of a single graphitic layer (arrow) with lattice image at high magnification (inset). EDX (HR-TEM) element mappings from (b): (e) carbon; (f) oxygen; (g) bromine.

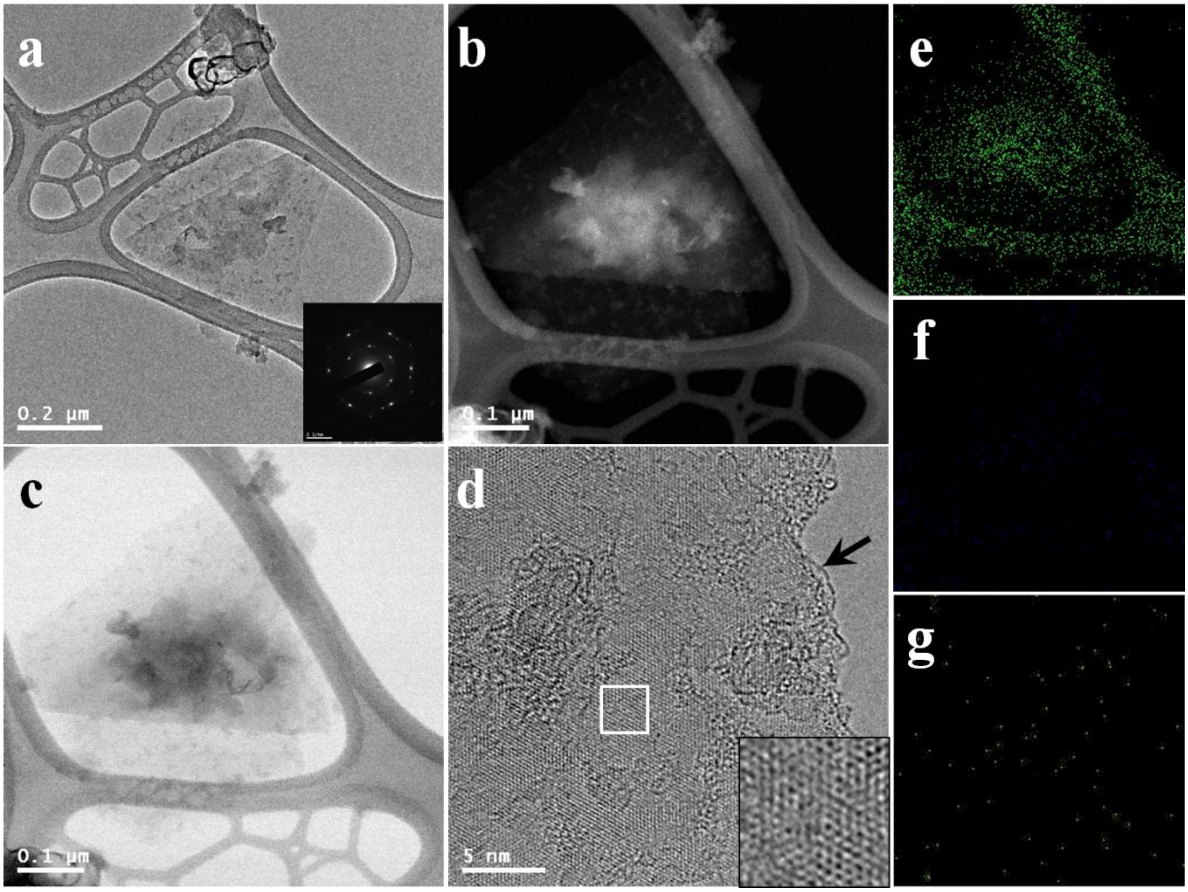

Figure 3-8. TEM images of IGnP: (a) bright field (BF) image. Inset is the selected area electron diffraction (SAED) pattern; (b, c) energy-filtered images; (d) high-resolution image of a single graphitic layer (arrow) with honeycomb lattice image (inset), indicating high crystallinity. EDX (HR-TEM) element mappings from (b): (e) carbon; (f) oxygen; (g) iodine.

The degree of halogenations could be quantitatively measured by thermogravimetric analyses (TGA) in nitrogen. The weight losses of ClGnP, BrGnP and IGnP at 800 °C were found to be 14.1, 28.6 and 24.6 wt%, respectively, while the pristine graphite displayed a negligible weight loss (0.3 wt%) under the same condition (Figure 3-9a and Table 3-2). The major part of the lost weight came from thermal decomposition of edge-halogen groups in XGnPs[42] in consistency with the EA data (Table 3-1).

Raman spectra given in Figure S7b show that the pristine graphite with the relatively large grain size has no detectable D band at around 1350 cm^{-1}, and hence the ratio of the D-band to G-band intensities (I_D/I_G) is nearly zero. However, all XGnPs showed strong D bands around 1350 cm^{-1} with the I_D/I_G ratios in the range of 1.05 – 1.31, indicating significant size reduction and edge distortion as

also indicated by Figures 3-3b-3-3d. It is of interest to note that the relative intensity of the D band decreased with decreasing atomic size of halogen in the order of I > Br > Cl, accompanied by peak narrowing. The above observation can be attributed to the dopant size effect with the bigger edge-functional groups for a more significant graphitic lattice distortion, as schematically shown in Figure 2g.

To characterize chemical compositions of the as-prepared XGnPs, we performed X-ray photoelectron spectroscopic (XPS) measurements (Figures 3-9c-3-9f). Along with the O1s and C1s peaks, the XPS survey spectra given in Figure S7c clearly show the Cl2p (Figure 3-9d), Br3d (Figure 3-9e)[43] and I3d (Figure 3-9f)[44] peaks for ClGnP, BrGnP and IGnP, respectively. It was found that the contents of Cl, Br and I to be 5.89, 2.78 and 0.95 at% for ClGnP, BrGnP and IGnP, respectively (see Table 3-2). In view of its surface sensitive nature, the XPS result may be not always in a good agreement with the EA (see Table 3-1) and TGA (see Table 3-2) data. The high-resolution Cl2p (Figure 3-9d), Br3d (Figure 3-9e)[43] and I3d (Figure 3-9f)[44] spectra show two different types of bonding for all the halogen dopants, leading to the unusual ORR activity observed for XGnPs (*vide infra*).

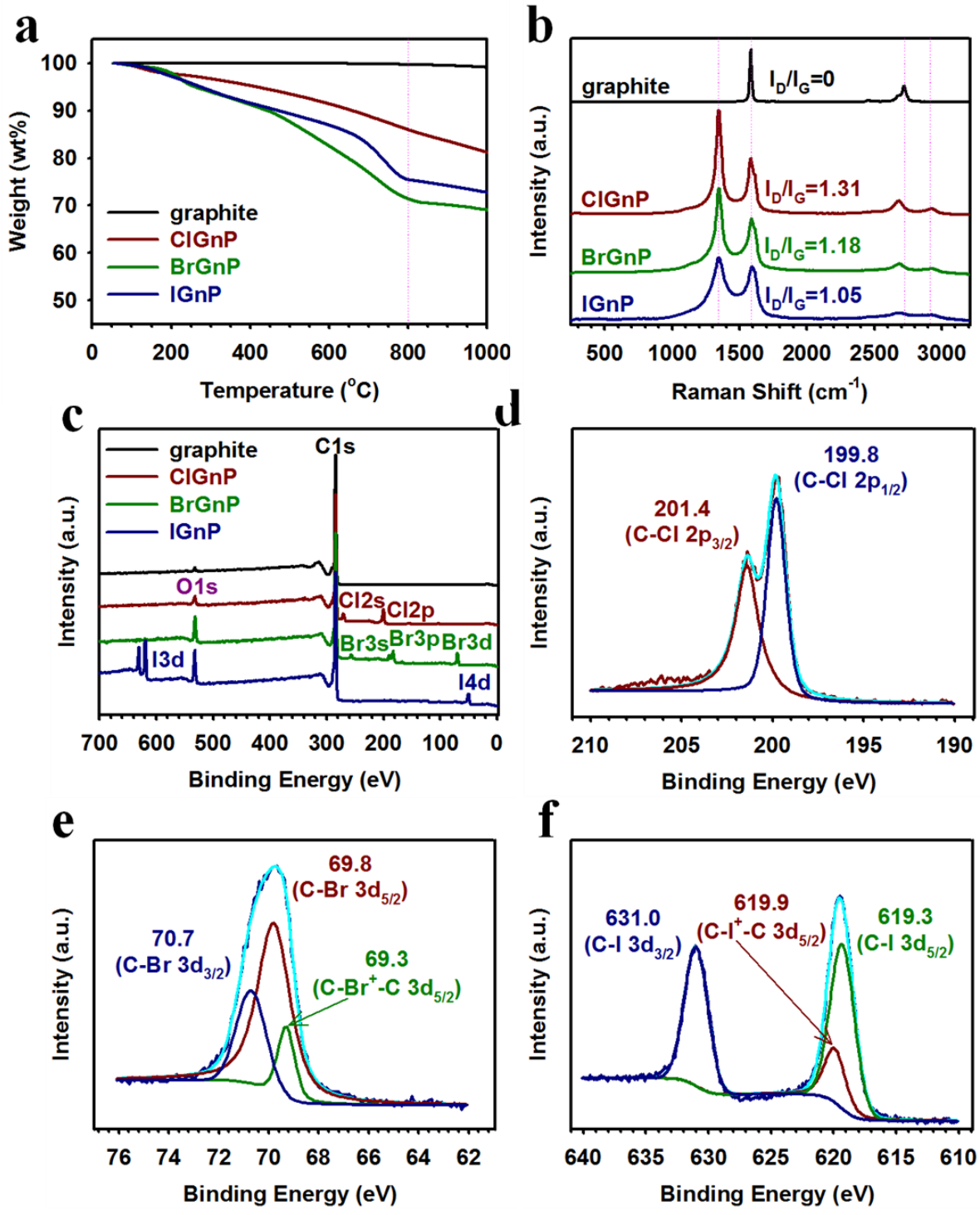

Figure 3-9. (a) TGA thermograms obtained from the heating rate of 10 ℃/min in nitrogen. (b) Raman spectra obtained with 532 nm wavelength; (c) XPS survey spectra of the pristine graphite and XGnPs. High-resolution XPS spectra of Cl, Br, and I for (d) ClGnP, (e) BrGnP, and (f) IGnP, respectively.

Having characterized the morphological and the chemical structures for XGnPs, we further investigated their electrocatalytic activities in N_2- and O_2-saturated 0.1 M aq. KOH solutions using the pristine graphite and commercial Pt/C electrocatalysts with the same mass loadings as reference. Cyclic voltammograms (CV) in Figures 3-10a~3-10d show the obvious oxygen reduction peaks for all the four carbon-based electrodes in the O_2-saturated 0.1 M aq. KOH solution, while they displayed featureless CVs in the corresponding N_2-satureted medium. Figure 3-10a shows a single cathodic reduction peak at -0.37 V with a current density of -0.28 mA cm^{-2} for the pristine graphite electrode in the O_2-saturated 0.1 M aq. KOH solution. The corresponding cathodic reduction peaks for the ClGnP, BrGnP and IGnP were positively shifted to -0.24, -0.22 and -0.22 V, respectively. The corresponding peak currents for oxygen reduction were determined to be -0.39, -0.60 and -0.78 mA cm^{-2} for the ClGnP, BrGnP and IGnP, respectively. These values are over 1.4, 2.1 and 2.8 times that of the pristine graphite (-0.28 mA cm^{-2}). Thus, the reduction currents of XGnPs gradually increased while their onset potentials positively shifted along the order of ClGnP < BrGnP < IGnP. As shown in Figures 3-11~3-13 and Table 3-3, the capacitances of XGnPs gradually increased in the order of the pristine graphite < ClGnP < BrGnP < IGnP. Among all the electrodes tested in this study, the IGnP electrode has the highest capacitances of 127.6 and 139.5 F g^{-1} in both N_2- and O_2-saturated electrolytes with a high cycle stability. Clearly, therefore, the edge-halogenations, particularly Br and I, play an important role to significantly improve the ORR activity of graphite, while edge-hydrogenated GnPs (HGnPs), prepared by ball-milling under the same conditions in the absence of halogen, showed marginally improved ORR activity[45].

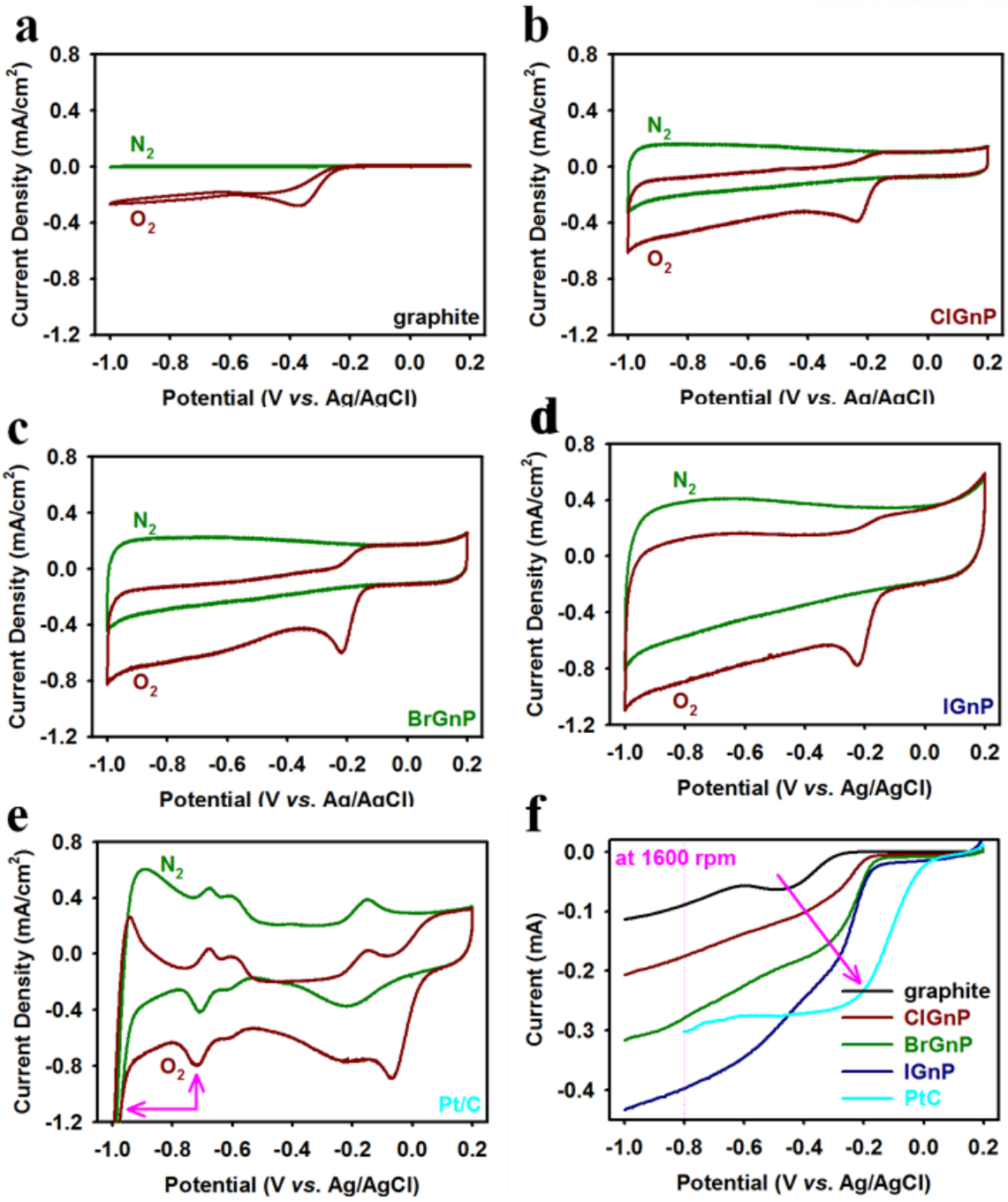

Figure 3-10. Cyclic voltammograms (CV) of samples on glassy carbon (GC) electrodes in N_2- and O_2-saturated 0.1 M aq. KOH solution with a scan rate of 10 mV s^{-1}: (a) the pristine graphite; (b) ClGnP; (c) BrGnP; (d) IGnP; (e) Pt/C. Pink arrows indicate the contributions of hydrogen evolution at around -0.7 V and out of limiting potential (-0.8 V). (f) Linear sweep voltammograms (LSV) at a rotation rate of 1600 rpm and a scan rate of 10 mV s^{-1}, showing a gradual increase in current and a positive shift in the onset potential along the order of the pristine graphite < ClGnP < BrGnP < IGnP < Pt/C (pink arrow).

Table 3-3. Capacitance and capacity retention of the pristine graphite, XGnPs and Pt/C in N_2- and O_2-saturated 0.1 M aq. KOH solution at a scan rate of 0.01 V/s

Sample	Capacitance (F/g)		Capacity Retention (%)	
	N_2	O_2	N_2	O_2
graphite	1.2	5.7	99.3	97.1
ClGnP	46.0	53.3	94.2	95.4
BrGnP	68.8	75.1	94.6	93.2
IGnP	127.6	139.5	95.2	96.2
Pt/C	99.6	101.4	87.8	88.7

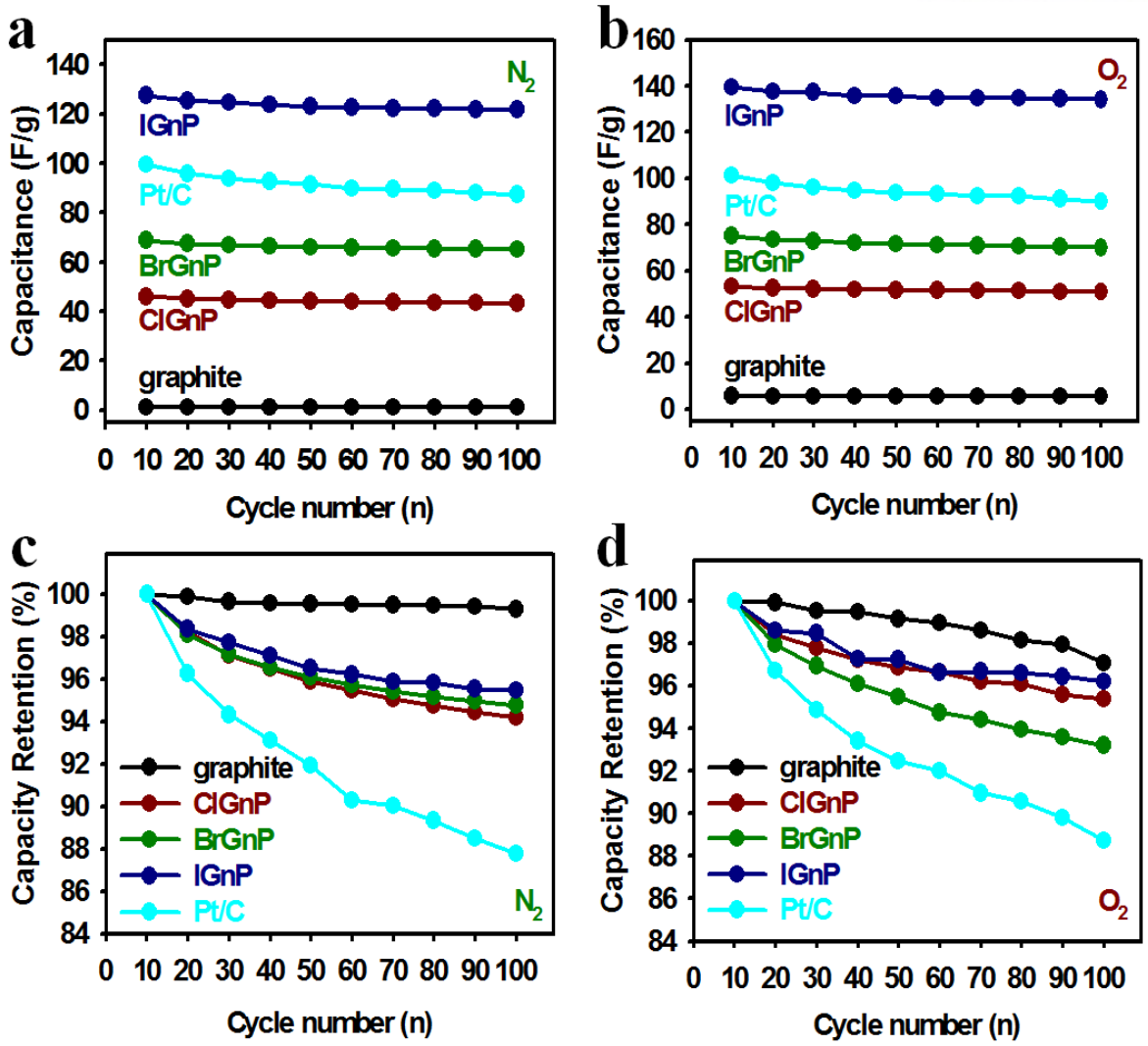

Figure 3-11. Capacitance changes with respect to the cycle number in 0.1 M aq. KOH solution at a scan rate of 0.01 V/s: (a) capacitance *vs*. cycle number in N_2 saturated electrolyte solution; (b) capacitance *vs*. cycle number in O_2 saturated electrolyte solution; (c) relative capacity retention *vs*. cycle number in N_2 saturated electrolyte solution; (d) relative capacity retention *vs*. cycle number in O_2 saturated electrolyte solution.

To further study the ORR performance, we carried out the linear sweep voltammetry (LSV) measurements on a rotating disk electrode (RDE) for the XGnP electrodes, along with the pristine graphite and commercial Pt/C electrodes, in O_2-saturated 0.1 M KOH at a scan rate of 0.01 V s^{-1} and a rotation rate of 1600 rpm. As shown in Figure 3-10f, the onset potential for oxygen reduction at the pristine graphite electrode is about -0.33 V, which positively shifted to the range of -0.16 – -0.14 V upon the edge-functionalization with halogen atoms - though still smaller than that of the Pt/C (-0.06

V). The limiting diffusion currents at -0.8 V for the pristine graphite, ClGnP, BrGnP, IGnP and Pt/C electrodes are -0.09, -0.18, -0.28, -0.40 and -0.30 mA, respectively. These current values for the XGnPs are about 2, 3.1 and 4.4 times higher than that of the pristine graphite and 60%, 93% and 133% that of the Pt/C. These results are consistent with the CV measurements (see Figures 3-10a-3-10e and Table 3-5), confirming, once again, the significant contributions to the ORR electrocatalytic activity of GnPs by the edge-halogenation.

To gain further insight into the kinetics of the XGnPs-catalyzed ORR process, we performed the RDE measurements in an O_2-saturated, 0.1 M KOH aqueous solution at various rotating speeds and a constant scan rate of 0.01 V s^{-1}. As shown in Figures 3-12 and 3-13, the diffusion current densities increased with increasing the rotating rates, while the onset potentials remained almost constant. Once again, the limiting current densities for XGnPs are much higher than those for the pristine graphite at any constant rotation rate. It is well known that the number of electron transfers (n) per O_2 molecule involved in the ORR process can be calculated from the slope of the Koutecky-Levich equation (see Experimental section in ESI)[46,47]. As shown in Figure 3-12f, the experimentally determined value (n = 4.0) at the limiting potential of -0.8 V for Pt/C agrees well with the theoretically calculated one (n = 4.0), indicating that a four-electron oxygen reduction process. The corresponding numbers of electrons transferred per O_2 molecule at -0.8 V for the pristine graphite, ClGnP, BrGnP and IGnP were calculated to be 2.0, 3.5, 3.8 and 3.9 respectively (Figure 3-13f). The number of transferred electrons for the pristine graphite is close to the classical two-electron process, whereas the ORR processes at all the XGnP electrodes are much closer to an ideal four-electron process.

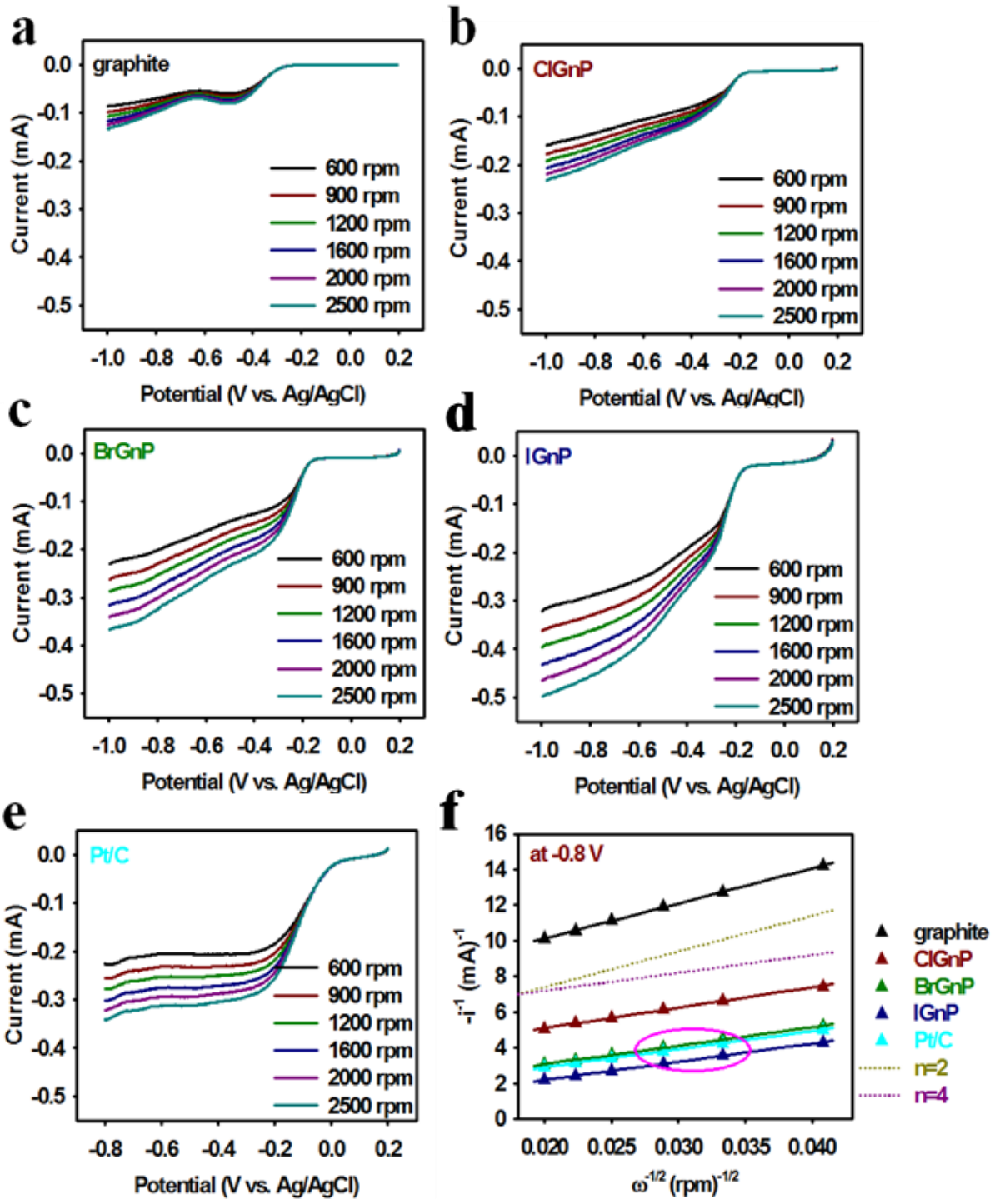

Figure 3-12. RDE voltammograms in O_2-saturated 0.1 M aq. KOH solution at a scan rate of 0.01 V/s at different rotating rates of 600, 900, 1200, 1600, 2000 and 2500 rpm: (a) the pristine graphite; (b) ClGnP; (c) BrGnP; (d) IGnP; (e) Pt/C; (f) Koutecky-Levich plots derived from the RDE measurements at -0.8 V electrode potentials. XGnPs and Pt/C (pink oval) are very close to a four-electron transfer process, while the pristine graphite is a classical two-electron process.

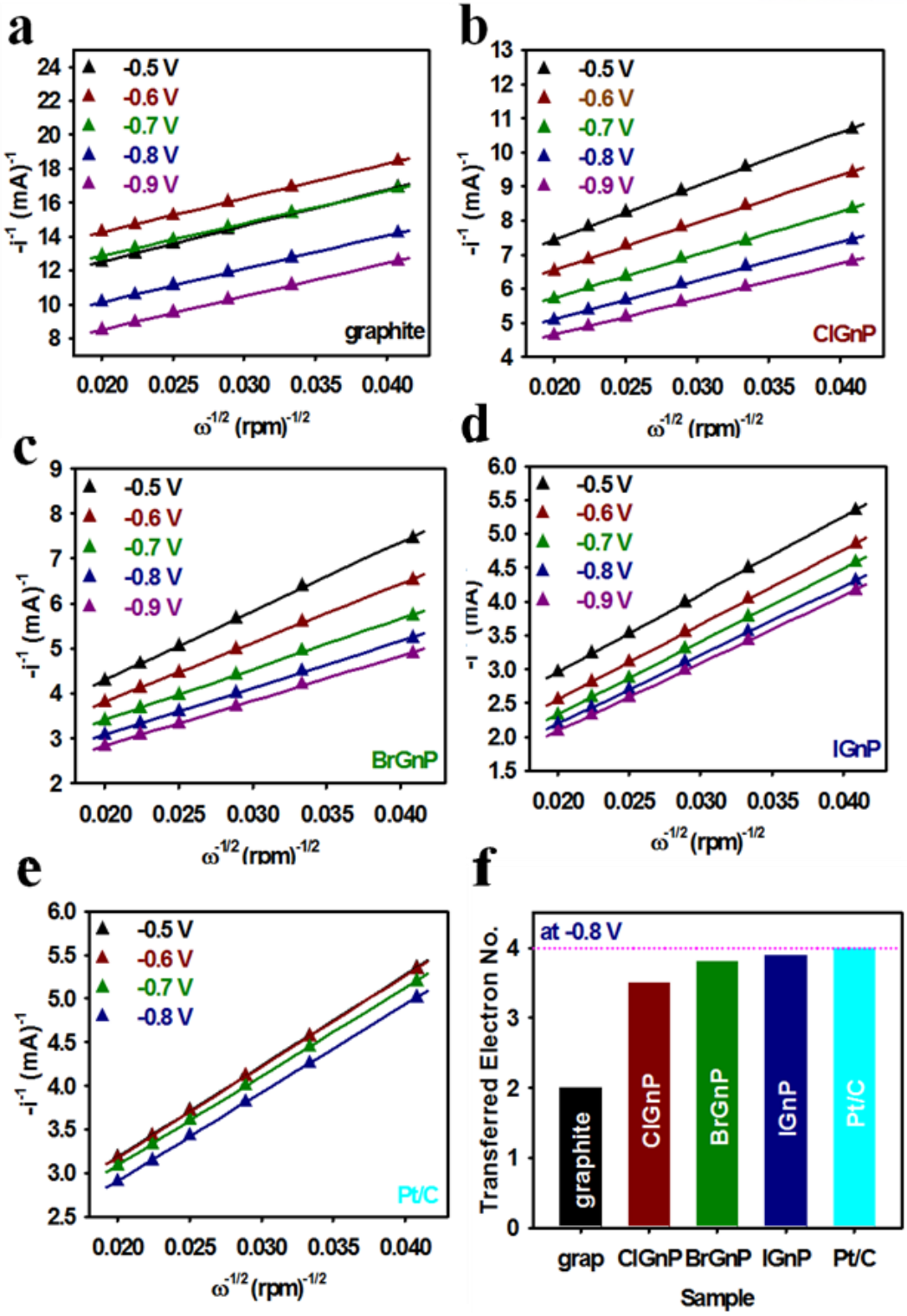

Figure 3-13. Koutecky-Levich plots derived from the RDE measurements at different electrode potentials (black line: -0.5 V, red line: -0.6 V green line:-0.7 V, blue line: -0.8 V and pink line: -0.9 V): (a) the pristine graphite; (b) ClGnP; (c) BrGnP; (d) IGnP; (e) Pt/C; (f) comparison of the numbers of electrons (*n*) transferred calculated from the limiting currents at -0.8 V.

The origin of ORR activity enhancement with the nitrogen-doped carbon-based materials has been previously attributed to the higher electronegativity (χ) of the nitrogen (3.04) than carbon (2.55) to polarize adjacent carbon atoms in graphitic frameworks to efficiently facilitate the O_2 adsorption and charge-transfer[12]. Considering the difference in the electronegativity between halogens (Cl = 3.16, Br = 2.96 and I = 2.66) and carbon (2.55), the reverse order ORR activities for ClGnP << BrGnP < IGnP observed in this study seems to be contradicted to the doping-induced charge-transfer mechanism[12]. However, it is noted that the atomic sizes of Br and I are larger than that of Cl, and hence the valence electrons of Br and I are much loosely bound than those of Cl for facilitating charge polarization in the BrGnP and IGnP electrodes. Unlike Cl, Br and I can form partially ionized bonds of $–Br^{+}–$ and $–I^{+}–$ (Figures 3-15d-3-15f) to further enhance the charge-transfer because of their relatively large atomic sizes.

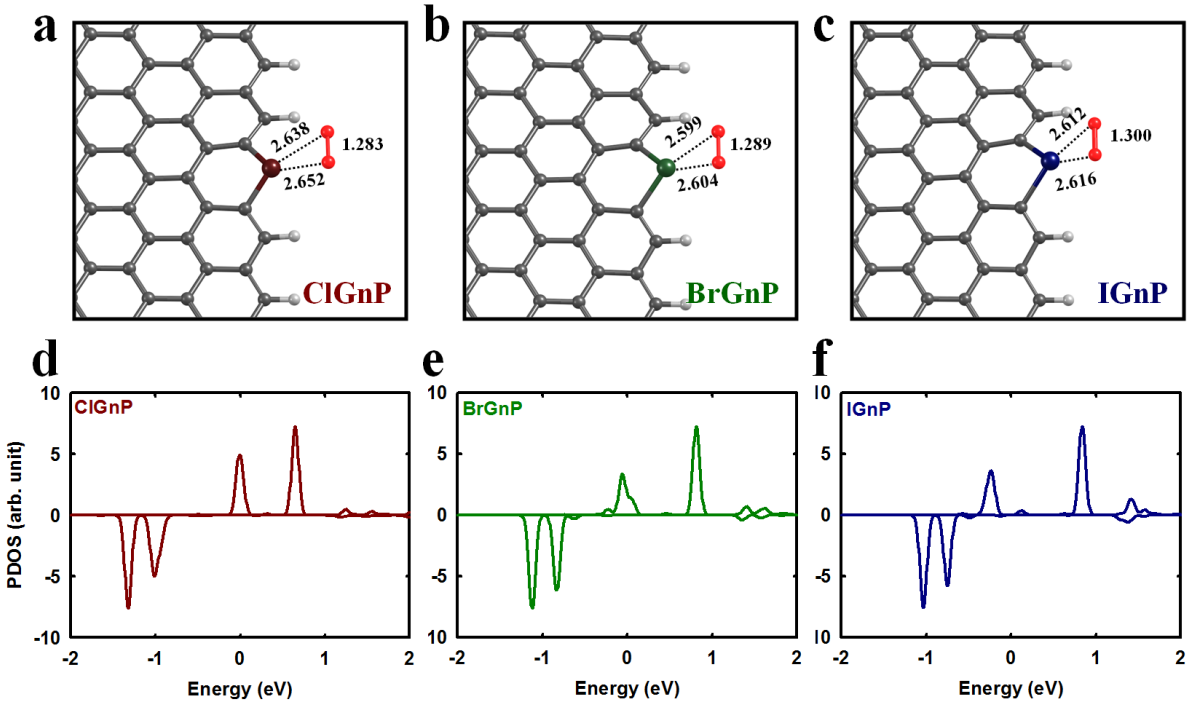

Figure 3-14. The optimized O_2 adsorption geometries onto XGnPs, in which halogen covalently linked to two sp^2 carbons: (a) ClGnP; (b) BrGnP; (c) IGnP. The projected density of electronic states onto O_2: (d) ClGnP; (e) BrGnP; (f) IGnP for the cases of corresponding (a), (b), and (c), respectively. In (a), (b) and (c), the O-O bond length and the shortest C-O bond are shown in angstroms.

The above scenarios are supported by the first-principle DFT calculations for various types of edge structures of the XGnPs. As observed in XPS spectra (Figures 3-9), only two distinct types of edge configurations are considered; namely (i) the bond formations between halogen atoms and the sp^2 carbons as dangling bonds at the zigzag edge (Figures 3-15a~3-15c), and (ii) the substitutions of halogen atoms with the C sites (*i.e.*, $–Cl^+–$, $–Br^+–$ and $–I^+–$) at the zigzag edge (Figures 3-14a~3-14c). When halogen atoms form the single sp^2 C-X dangling bond, the edges does not have particular binding affinity with O_2 molecule (Figures 3-15d~3-15f). As a result of total energy minimization, the adsorption of O_2 molecules is no more than the dispersive intermolecular physisorption. However, when halogen atoms substitute for the C sites in the zigzag edges as shown in Figures 3-14a~3-14c, the halogenated edges revealed decent binding affinity with O_2. The PBE density functional calculations resulted in the binding of O_2 with the strength of 0.71, 0.75, and 1.04 eV, respectively, for the cases of Cl (Figure 3-14a), Br (Figure 3-14b), and I (Figure 3-14c) with respect to the triplet state of free O_2 in the vacuum. On the basis of the occupation of the lowest-unoccupied molecular orbital (LUMO) level of O_2 as shown in Figures 4d-4f, it is noteworthy that the efficiency of the charge transfer between the halogen and adsorbed O_2 follows the atomic size in the order of Cl < Br < I. Accordingly, the O-O bond length increases in that order (see Figures 3-14a~3-14c). The results suggest that the edges of halogenated graphene have enough activities to attract O_2 and to weaken the O-O bond of the adsorbed O_2, which is favorable for an efficient development into water upon reduction and protonation.

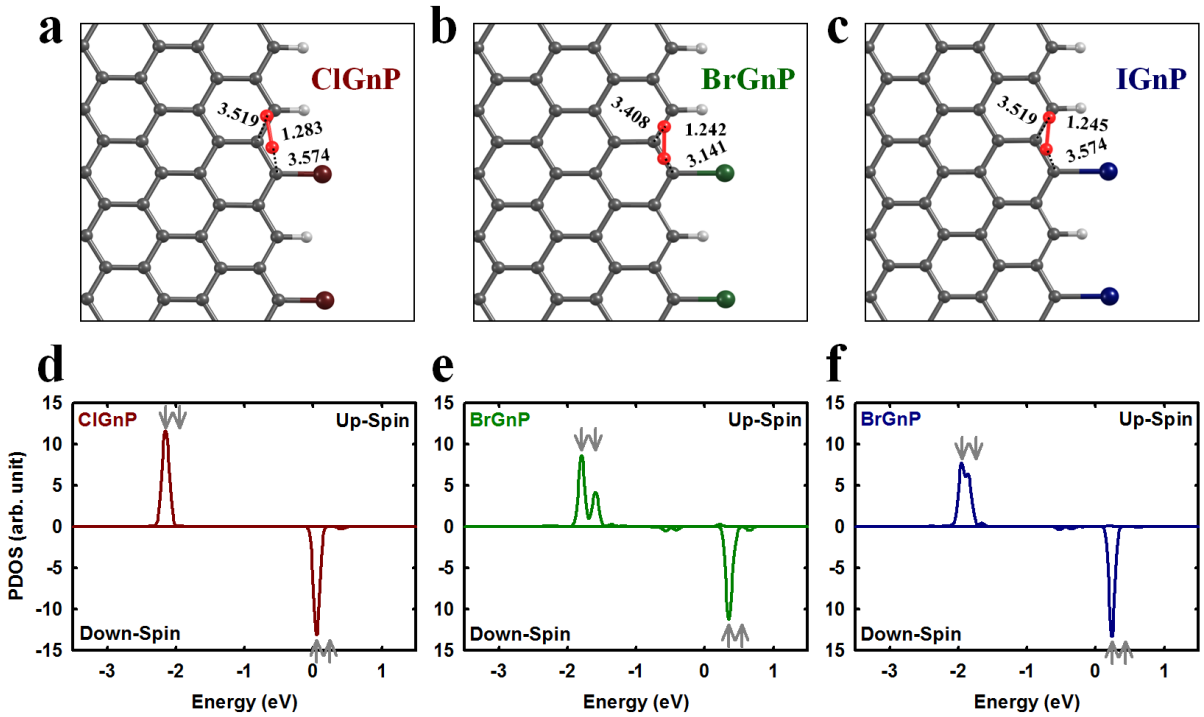

Figure 3-15. The optimized O_2 adsorption geometries onto XGnPs, in which halogen covalently linked to the sp^2 carbon as dangling bond: (a) ClGnP; (b) BrGnP; (c) IGnP. The projected density of electronic states onto O_2: (d) ClGnP; (e) BrGnP; (f) IGnP corresponding to (a), (b), and (c), respectively. In (a), (b) and (c), the bond lengths of the shortest C-O and O-O are shown in angstroms. In (d), (e) and (f), the downward and upward double arrows indicate the HOMO and LUMO states of O_2 triplet (doubly degenerated antibonding states). When sp^2 C-X is dangling bond, the charge transfer from the basal plane to the adsorbed O_2 is negligible, as indicated by the occupation of the LUMO states. It is thus thought that these configurations of halogenated edges do not contribute to the ORR catalysis.

To investigate the cycle stability of the XGnP electrocatalysts, we performed accelerated degradation test (ADT) by continuous chronoamperometric measurements at -0.25 V in an O_2-saturated 0.1 M aq. KOH solution at a rotation rate of 1600 rpm. As shown in Figure 3-16a, the current densities for all of the electrodes initially decreased with time. However, the XGnP electrodes exhibited a relatively slow decay rate, maintaining 85.6 – 87.4% of their initial currents even after 10,000 s, in respect to the commercial Pt/C electrode (62.5%). These results indicate that the XGnP electrocatalysts have a much better electrochemical stability than the commercial Pt/C electrocatalyst.

Furthermore, a sharp decrease in the ORR current density was observed for the commercial Pt/C electrocatalyst upon the additions of methanol while the XGnP electrodes and even the pristine graphite were insensitive to the methanol addition.(Figure 3-16b) For a methanol fuel cell, methanol crossover from anode to cathode could diminish cathodic performance through the depolarizing effect. In comparison with many precedent carbon-based ORR catalysts, the preparation of XGnPs *via* ball-milling is very simple for practicality with overall better performance. Therefore, the above results unambiguously indicate that the XGnPs have much higher selectivity toward ORR than the commercial Pt/C electrocatalyst and are free from the methanol crossover, promising for applications in fuel cells and other energy-related devices.

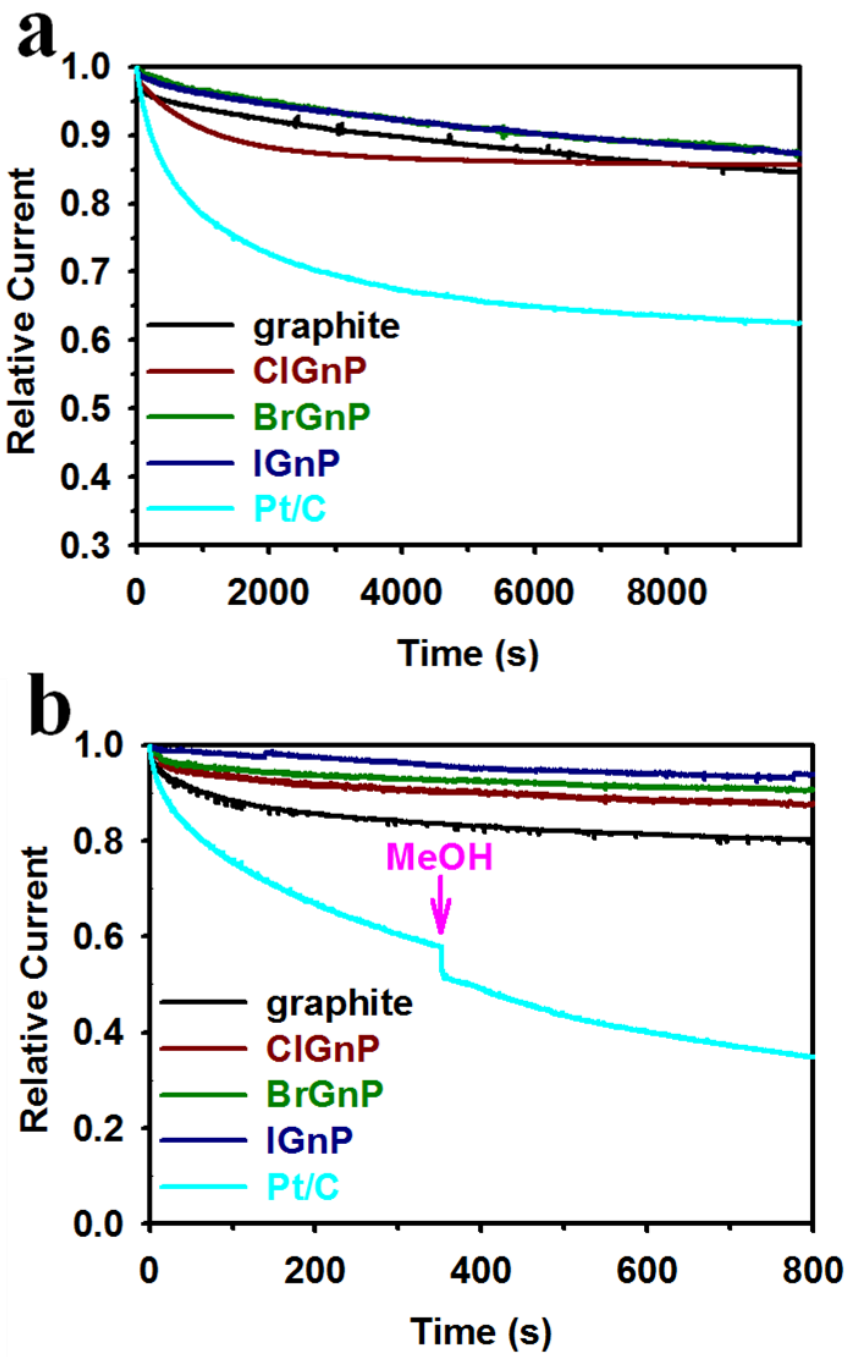

Figure 3-16. (a) Current-time (*i-t*) chronoamperometric response of the pristine graphite, XGnPs, and commercial Pt/C electrodes at -0.25 V *vs.* Ag/AgCl in O_2-saturated 0.1 M aq. KOH solution at a rotation rate of 1600 rpm. Note that the blue and green curves are almost overlapped with each other. (b) The current-time (*j-t*) chronoamperometric responses for ORR at the pristine graphite, XGnPs, and commercial Pt/C electrocatalysts in an O_2-saturated 0.1 M aq. KOH solution at -0.40 V *vs.* Ag/AgCl and 3.0 M methanol was added at around 280 s.

3.8 Conclusions

In summary, we have, for the first time, used a simple ball-milling method to synthesize edge-halogenated graphene nanoplatelets (XGnPs). The resultant XGnPs were tested as cathode electrodes of fuel cells and revealed remarkable electrocatalytic activities for ORR with high tolerance to methanol crossover/CO poisoning effects and longer-term stability than those of the pristine graphite and commercial Pt/C electrocatalysts. To understand the underlying mechanism, first-principle DFT calculations were performed for various edge configurations. We found that the edges of halogenated graphene had favorable binding affinity with O_2 molecule, and the O-O bond strengths are weakened as a result of the halogenation-induced charge transfer. Our results suggest new insights and practical methods for designing edge-functionalized GnPs as high-performance metal-free ORR electrocatalysts through low-cost and scalable ball-milling techniques.

3.9 References

(1) Stamenkovic, V. R. et al. Improved oxygen reduction activity on Pt_3Ni (111) via increased surface site availability. Science, **2007**, *315*, 493-497

(2) Zhang, J. et al. Mixed-metal Pt monolayer electrocatalysts for enhanced oxygen reduction kinetics. J. Am. Chem. Soc. **2005**, *127*, 12480-12481.

(3) Xiao, L., Zhuang, L., Liu, Y. & Lu, J. Activating Pd by morphology tailoring for oxygen reduction. J. Am. Chem. Soc. **2008**, *131*, 602-608.

(4) Peng, Z. & Yang, H. Synthesis and oxygen reduction electrocatalytic property of Pt-on-Pd bimetallic heteronanostructures. J. Am. Chem. Soc. **2009**, *131*, 7542-7543.

(5) Zhang, S., Shao, Y., Yin, G. & Lin, Y. Carbon nanotubes decorated with Pt nanoparticles via electrostatic self-assembly: a highly active oxygen reduction electrocatalyst. J. Mater. Chem. **2010**, *20*, 2826-2830.

(6) Lim, B. et al. Pd-Pt bimetallic nanodendrites with high activity for oxygen reduction. Science. **2009**, *324*, 1302-1305.

(7) Zhang, S., Shao, Y., Yin, G. & Lin, Y. Self-assembly of Pt nanoparticles on highly graphitized carbon nanotubes as an excellent oxygen-reduction catalyst. Appl. Catal. B-Envion. **2011**, *102*, 372-377.

(8) Huang, S. Y., Ganesan, P., Park, S. & Popov, B. N. Development of a titanium dioxide-supported platinum catalyst with ultrahigh stability for polymer electrolyte membrane fuel cell applications. J. Am. Chem. Soc. **2009**, *131*, 13898-13899.

(9) Wu, G., More, K. L., Johnston, C. M. & Zelenay, P. High-performance electrocatalysts for oxygen reduction derived from polyaniline, iron, and cobalt. Science. **2011**, *332*, 443-447.

(10) Lefèvre, M., Proietti, E., Jaouen, F. & Dodelet, J. P. Iron-based catalysts with improved oxygen reduction activity in polymer electrolyte fuel cells. Science. **2009**, *324*, 71-74.

(11) Byon, H. R., Suntivich, J. & Shao-Horn, Y. Graphene-based non-noble-metal catalysts for oxygen reduction reaction in acid. Chem. Mater. **2011**, *23*, 3421-3428.

(12) Gong, K., Du, F., Xia, Z., Durstock, M. & Dai, L. Nitrogen-doped carbon nanotube arrays with high electrocatalytic activity for oxygen reduction. Science. **2009**, *323*, 760-764.

(13) Wang, S., Yu, D. & Dai, L. Polyelectrolyte functionalized carbon nanotubes as efficient metal-free electrocatalysts for oxygen reduction. J. Am. Chem. Soc. **2011**, *133*, 5182-5185.

(14) Yang, L. et al. Boron-doped carbon nanotubes as metal-free electrocatalysts for the oxygen reduction reaction. Angew. Chem. Int. Ed. **2011**, *123*, 7270-7273.

(15) Sheng, Z. H. et al. Catalyst-free synthesis of nitrogen-doped graphene via thermal annealing graphite oxide with melamine and its excellent electrocatalysis. ACS Nano **2011**, *5*, 4350-4358.

(16) Tang, Y., Allen, B. L., Kauffman, D. R. & Star, A. Electrocatalytic activity of nitrogen-doped carbon nanotube cups. J. Am. Chem. Soc. **2009**, *131*, 13200-13201.

(17) Shanmugam, S. & Osaka, T. Efficient electrocatalytic oxygen reduction over metal free-nitrogen doped carbon nanocapsules. Chem. Commun. **2011**, *47*, 4463-4465.

(18) Sheng, Z. H., Gao, H. L., Bao, W. J., Wang, F. B. & Xia, X. H. Synthesis of boron doped graphene for oxygen reduction reaction in fuel cells. J. Mater. Chem. **2011**, *22*, 390-395.

(19) Yao, Z. et al. Catalyst-free synthesis of iodine-doped graphene via a facile thermal annealing process and its use for electrocatalytic oxygen reduction in an alkaline medium. Chem. Commun. **2012**, *48*, 1027-1029.

(20) Liu, R., Wu, D., Feng, X. & Müllen, K. Nitrogen-doped ordered mesoporous graphitic arrays with high electrocatalytic activity for oxygen reduction. Angew. Chem. Int. Ed. **2010**, *122*, 2619-2623 .

(21) Yu, D., Zhang, Q. & Dai, L. Highly efficient metal-free growth of nitrogen-doped single-walled carbon nanotubes on plasma-etched substrates for oxygen reduction. J. Am. Chem. Soc. **2010**, *132*, 15127-15129.

(22) Zheng, Y. et al. Nanoporous graphitic-C_3N_4@carbon metal-free electrocatalysts for highly efficient oxygen reduction. J. Am. Chem. Soc. **2011**, *133*, 20116-20119.

(23) Jeon, I. Y. et al. Formation of large-area nitrogen-doped graphene film prepared from simple solution casting of edge-selectively functionalized graphite and its electrocatalytic activity. Chem. Mater. **2011**, *23*, 3987-3992.

(24) Qu, L., Liu, Y., Baek, J. B. & Dai, L. Nitrogen-doped graphene as efficient metal-free electrocatalyst for oxygen reduction in fuel cells. ACS Nano **2010**, *4*, 1321-1326.

(25) Liu, Z. W. et al. Phosphorus-doped graphite layers with high electrocatalytic activity for the O_2 reduction in an alkaline medium. Angew. Chem. Int. Ed. **2011**, *123*, 3315-3319.

(26) Yang, Z. et al. Sulfur-doped graphene as an efficient metal-free cathode catalyst for oxygen reduction. ACS Nano **2011**, *6*, 205-211.

(27) Yang, S. et al. Efficient synthesis of heteroatom (N or S)-doped graphene based on ultrathin graphene oxide-porous silica sheets for oxygen reduction reactions. Adv. Funct. Mater **2012**, *22*, 3634-3640.

(28) Wang, S. et al. Vertically aligned BCN nanotubes as efficient metal-free electrocatalysts for the oxygen reduction reaction: a synergetic effect by co-doping with boron and nitrogen. Angew. Chem. Int. Ed. **2011**, *50*, 11756-11760.

(29) Wang, S. et al. BCN graphene as efficient metal-free electrocatalyst for the oxygen reduction reaction. Angew. Chem. Int. Ed. **2012**, *51*, 4209-4212.

(30) Zhang, M. & Dai, L. Carbon nanomaterials as metal-free catalysts in next generation fuel cells. Nano Energy **2012**, *1*, 514-517.

(31) Hummers Jr, W. S. & Offeman, R. E. Preparation of graphitic oxide. J. Am. Chem. Soc. **1958**, *80*, 1339-1339.

(32) Jeon, I.-Y. et al. Edge-carboxylated graphene nanosheets via ball milling. Proc. Natl. Acad. Sci. USA **2012**, *109*, 5588-5593.

(33) Zheng, J. et al. Production of graphite chloride and bromide using microwave sparks. Sci. Rep. **2012**, *2*, 662.

(34) Jaccaud, M., Faron, R., Devilliers, D. & Romano, R. Fluorine. Ullmann's Encyclopedia of Industrial Chemistry, John Wiley and Sons, Inc., New York, **2000**.

(35) Moore, J. W., Stanitski, C. L. & Jurs, P. C. Principles of chemistry: the molecular science. Brooks/Cole Publishing Company, **2009**.

(36) Cho, D. W. et al. Nature and kinetic analysis of carbon-carbon bond fragmentation reactions of cation radicals derived from SET-oxidation of lignin model compounds. J. Org. Chem. **2010**, *75*, 6549-6562.

(37) Li, Z., Lu, C., Xia, Z., Zhou, Y. & Luo, Z. X-ray diffraction patterns of graphite and turbostratic carbon. Carbon **2007**, *45*, 1686-1695.

(38) Dikin, D. A. et al. Preparation and characterization of graphene oxide paper. Nature **2007**, *448*, 457-460.

(39) Zhu, Y. et al. Graphene and graphene oxide: synthesis, properties, and applications. Adv. Mater. **2010**, *22*, 3906-3924.

(40) Everett, D. H. & Chemistry, R. S. Basic principles of colloid science, vol. 144, Royal Society of Chemistry, London, **1988**.

(41) Becerril, H. A. et al. Evaluation of solution-processed reduced graphene oxide films as transparent conductors. ACS Nano **2008**, *2*, 463-470.

(42) Stankovich, S. et al. Synthesis of graphene-based nanosheets via chemical reduction of exfoliated graphite oxide. Carbon **2007**, *45*, 1558-1565.

(43) Zheng, Q. B. et al. Improved electrical and optical characteristics of transparent graphene thin films produced by acid and doping treatments. Carbon **2011**, *49*, 2905-2916.

(44) Jung, Y., Hwang, S. J. & Kim, S. J. Spectroscopic evidence on weak electron transfer from intercalated iodine molecules to single-walled carbon nanotubes. J. Phys. Chem. C **2007**, *111*, 10181-10184.

(45) Jeon, I.-Y. et al. Large-scale production of edge-selectively functionalized graphene nanoplatelets via ball milling and their use as metal-free electrocatalysts for oxygen reduction reaction. J. Am. Chem. Soc. **2012**, *135*, 1386-1393.

(46) Jung, H. Y., Park, S. & Popov, B. N. Electrochemical studies of an unsupported PtIr electrocatalyst as a bifunctional oxygen electrode in a unitized regenerative fuel cell. J. Power Sources **2009**, *191*, 357-361.

(47) Zhang, S., Shao, Y., Yin, G. & Lin, Y. Stabilization of platinum nanoparticle electrocatalysts for oxygen reduction using poly (diallyldimethylammonium chloride). J. Mater. Chem. **2009**, *19*, 7995-8001.

Chapter IV. Non-noble iron comparable to noble platinum for oxygen reduction reaction

4.1 Abstract

We describe modern alchemy that converts non-precious iron (Fe) into comparably active and highly stable catalyst compared with precious platinum (Pt) for oxygen reduction reaction (ORR) in both alkaline and acidic media. The Fe-based catalyst is obtained by *in-situ* encapsulation of Fe nanoparticles with a nitrogenated holey two-dimensional carbon framework (denoted C_2N). The structure of the Fe nanoparticles covered by C_2N (Fe@C_2N) layers is confirmed by transmission electron microscopy (TEM). The high catalytic activity of Fe@C_2N is attributed to the electrochemically transparent C_2N layers, which facilitate an efficient electron tunneling to oxygen. The durability of Fe@C_2N stems from the protection of Fe nanoparticles by the electrochemically stable C_2N layers. The synergistic effects is attributed to the unique C_2N structure, which consists of evenly distributed holes, each one surrounded by six nitrogen atoms, providing abundant coordination sites to stabilize the cocooned Fe nanoparticles.

4.2 Introduction

Electrochemical catalysts are essential for the clean and sustainable energy technologies such as fuel cells[1,2] and metal-air cells.[3,4] In these systems, platinum (Pt)-based materials have long been regarded as the most efficient catalysts for oxygen reduction reaction (ORR).[5,6] However, their sensitivity to fuel crossover and carbon monoxide (CO) poisoning, limited reserves, electrochemical loss and very high cost hamper their large-scale commercialization in air-breathing electrodes.[7] There have been two major research directions to find alternative materials to replace Pt-based catalysts. The first one is heteroatom-doped carbon-based materials, which display appreciable catalytic activity and good stability.[8-10] However, they only work in alkaline media and their onset potential is not as good as Pt catalyst.[7] The other comprehensive efforts have targeted non-precious metal-based catalysts.[11-13] Although their onset potential is near that of Pt, they are always suffering from instability. In this connection, researchers have been actively searching for an efficient encapsulation of the non-precious metal (*e.g.*, Fe, Co) nanoparticles by using carbon-based materials to achieve both catalytic performance and stability.[13] Pure carbon-based materials such as carbon nanotubes and graphene are, however, not polar enough to provide a strong interaction with metal nanoparticles for efficient encapsulation. As a result, hybrid systems of non-precious metal nanoparticles and heteroatom-doped carbon-

based materials have gathered huge interest for ORR catalysts.[14-16] Nevertheless, they are still electrochemically unstable due to defective encapsulation. One of the major pitfalls associated with metal-based electrocatalysts including Pt is their dissolution in electrolytes during the electrochemical redox process, diminishing the catalyst activity and contaminating the electrode and membrane[17] and thus leading to a fading overall catalytic performance. The roles of encapsulating materials should not only provide electrochemical transparency for efficient catalytic activity but also protect the non-precious metal nanoparticles for stability. Therefore, the most important challenge is to evenly distribute holes and heteroatoms through the encapsulating layers for a enhanced catalytic performance *via* efficient electron tunneling and for a stable encapsulation of metal nanoparticles *via* effective coordination.

4.3 Materials

All the solvents, chemicals and reagents were purchased from Aldrich Chemical Inc., unless otherwise stated. Solvents were degassed with nitrogen purging before use. All reactions were performed under nitrogen atmosphere using oven dried glassware. 1,2,3,4,5,6-hexaaminobenzene was synthesized according to a procedure described in the literature.

4.4 Instrumentations

Thermogravimetric analysis (TGA) was conducted in air and in nitrogen atmosphere at a heating rate of 10 ℃/min using a Thermogravimetric Analyzer Q200 TA Instrument, USA. The surface area was calculated by nitrogen adsorption-desorption isotherms using the Brunauer-Emmett-Teller (BET) method on Micromeritics ASAP 2504N. Scanning electron microscope (SEM) images were taken with a Field Emission Scanning Electron Microscope Nanonova 230 FEI, USA. X-ray photoelectron spectroscopy (XPS) was performed on a X-ray Photoelectron Spectrometer Thermo Fisher K-alpha (UK). X-ray diffraction (XRD) studies were taken on a High Power X-Ray Diffractometer D/MAZX 2500V/PC (Cu–Kα radiation, 35 kV, 20 mA, λ = 1.5418 Å) Rigaku, Japan. The extended X-ray fine structures (EXAFS) measurements were carried out using a Lab-EXAFS (Rigaku, Japan) with a Ge (220) crystal. The Fe–K edge spectra were recorded in transmittance mode at room temperature. EXAFS data were analyzed to fit the experimental EXAFS spectra to theoretical values obtained by an IFEFFIT program based on FEFF8. High resolution transmission electron microscopy (TEM) was performed by using a JEM-2100F microscope (JEOL, Japan) under an operating voltage of 200 keV. The samples for TEM were prepared by drop casting a N-methyl-2-pyrrolidone (NMP) dispersion on Quantifoil holey carbon TEM grid and dried in oven at 80 ℃. Elemental analysis was conducted with a Thermo scientific Flash 2000 Analyzer.

4.5 Synthesis of the ORR catalyst (Fe@C_2N)

$FeCl_3$ (1.168g) was first dissolved in NMP (35 mL) and placed on an ice bath in a 3-necked round bottom flask. Hexaketocyclohexane octahydrate (HKH; 1.125 g, 3.603 mmol) was added followed by the addition of Hexaaminobenzene trihydrochloride (HAB; 1.00g, 3.603 mmol) under nitrogen atmosphere. The reaction flask was allowed to warm up to room temperature for 2 hours. The ice bath was replaced with an oil bath, which was heated to 175 ℃. This temperature was maintained during 8h of reflux. After completion of the reaction the reaction mixture was cooled to 80 ℃ and $NaBH_4$ (40 mL, 10% solution) was added; then the mixture was refluxed again for 3 hours. Then, the flask was cooled to room temperature and water was added. The precipitated black solid product was collected by suction filtration using PTFE (0.5 μm) membrane. The resultant dark solid was further Soxhlet extracted with methanol and water, respectively for three days each, and freeze dried below -120 ℃ under reduced pressure. After drying the product was annealed at 600 ℃ for 2 hours under argon atmosphere. After cooling down the material was leached with 4 M HCl for 4 hours to remove free standing metallic residues, if any.

4.6 Cyclic voltammogram

The electrochemical tests were carried out using a computer-controlled potentiostat (1470E Cell Test System, Solartron Analytical, UK) with a typical three-electrode cell. A platinum gauze was used as a counter-electrode and an Ag/AgCl (Saturated KCl) electrode as the reference electrode. All the experiments were conducted at ambient conditions. The working electrodes were prepared by applying catalyst inks onto the prepolished glassy carbon (GC) disk electrodes. Briefly, samples were dispersed in NMP and ultrasonicated for 1 min to form uniform catalyst inks (2 g L-1). A total of 20 μL of a well-dispersed catalyst ink was applied onto a pre-polished glassy carbon (GC) disk electrode (3 mm in diameter). After drying at room temperature, Nafion (0.05 wt.%) stock solution (1 μL) in ethanol was applied onto the surface of the catalyst layer to form a thin protective film. The electrodes thus prepared were dried thoroughly at room temperature prior to the electrochemical tests.

4.7 Rotating disk electrode (RDE) measurement

For the RDE studies catalyst inks were prepared by the same method as for CV's. 20 μl ink was loaded on a glassy carbon rotating disk electrode of 3 mm in diameter (RDE-3A, BAS, Japan).The working electrode was scanned cathodically at a rate of 0.01 V s^{-1} with varying the rotating speed from 600 rpm to 2500 rpm.

The detailed kinetic analysis was conducted according to Koutecky-Levich plots in eq. (1):

$$\frac{1}{j} = \frac{1}{j_k} + \frac{1}{B\omega^{0.5}} \quad (1)$$

where *jk* is the kinetic current and B is Levich slope which is given by eq. (2):

$$B = 0.2nF(D_{O_2})^{2/3}\nu^{-1/6}C_{O_2} \quad (2)$$

In 0.1 M aq. KOH: Here *n* is the apparent number of electrons transferred in the reduction of one O^2 molecule, F is the Faraday constant (F = 96485 C mol^{-1}), D_{O2} is the diffusion coefficient of O_2, ν is the kinematics viscosity for KOH and CO_2 is concentration of O_2 in the solution. The constant 0.2 is adopted when the rotation speed is expressed in rpm. According to equations (1) and (2), the apparent number of electrons transferred (n) can be obtained from the slope of Koutecky-Levich plot of i^{-1} vs. $\omega^{-1/2}$. From published data for F (96485 C mol^{-1}), D_{O2} (1.9×10-5 cm2 s-1), ν (0.01 cm^2 s^{-1}), and CO_2 (1.2 ×10^{-6} mol cm^{-3}), B is calculated to be 0.144 mA $s^{-1/2}$ at A=0.9625 cm^2 for a four-electron exchange reaction (n = 4).

In 0.5 M aq. H_2SO_4: n is the overall electron transfer number per O_2, F is the Faraday constant (F = 96485 C mol^{-1}). C_{O2} is the bulk concentration of dissolved O2 in the electrolyte (1.1 × 10^{-6} mol cm^{-3} in 0.5 mol L−1 H_2SO_4), D_{O2} is the diffusion coefficient of O_2 (1.4 × 10^{-}5 cm^2 s^{-1}) and ν is the kinematic viscosity (0.01 cm^2 s^{-1}).

4.8 Rotating ring-disk electrode (RRDE) measurement

The RRDE measurement were carried out using a computer-controlled potentiostat (VSP, BioLogic Science instruments, USA) For RRDE measurements, catalyst inks and electrodes were prepared by the same method as for CV's. 100 µl ink was loaded on a glassy carbon rotating disk electrode of 4 mm in diameter. After measurement in Ag/AgCl, we have expressed all the potentials vs RHE.

In 0.1 M KOH: The disk electrode was scanned cathodically at a rate of 0.01 V s^{-1} and the ring potential was constant at 0.4 V *vs*. Ag/AgCl. The % $HO2^{-}$ and the electron transfer number (n) were determined by the following equations.

$$\%\,HO_2^- = 200 \times \frac{I_r/N}{I_d + I_r/N}$$

$$n = 4 \times \frac{I_d}{I_d + I_r/N} \quad (3)$$

where Id is the disk current, Ir is the ring current and N is the current collection efficiency of the Pt ring. N was determined to be 0.40 from the reduction of $K_3Fe(CN)_6$.

In 0.5 M H_2SO_4: The disk electrode was scanned cathodically at a rate of 0.01 V s^{-1} and the ring potential was constant at 1.0 V *vs*. Ag/AgCl. The % H_2O_2 and the electron transfer number (n) were determined by the following equations.

$$\% H_2O_2 = \frac{200 i_r/N}{i_d + i_r/N}$$

$$n = \frac{4 i_d}{i_d + {}^{i_r}/_N} \quad (4)$$

4.9 Fabrication of hybrid lithium (Li)-air cell

A Li foil with a thickness of 0.2 mm was obtained from Honjo metal, and disks with a diameter of 1 cm were cut for use as the cell anode. 1 M LiPF6 in tetraethylene glycol dimethyl ether (TEGDME) was used as an organic liquid electrolyte, and 1 M $LiNO_3$ + 0.5 M LiOH in pure deionized (DI) water was used as the aqueous liquid electrolyte. All reagents were purchased from Sigma-Aldrich and used as received, unless otherwise specified. The anode and cathode were separated by a $Li_{1+x+y}Ti_{2-x}Al_xP_{3-y}Si_yO_{12}$ (0.15 mm thickness, OHARA Inc., Japan) solid Li-ion conducting ceramic glass. The air electrodes were prepared by spraying the catalyst inks of Fe@C_2N or Pt/C and poly(vinylidene fluoride-*co*-hexafluoropropylene) (PVDF-HFP) binder (Sigma-Aldrich) onto the gas-diffusion layer (Toray TGP-H-090). The catalyst loading density and binder content in the air electrode were 1 mg cm^{-2} and 20 wt%, respectively. Discharge-charge experiments were conducted on a Biologic VMP3.

4.10 Fabrication of zinc (Zn)-air cell.

The air electrode consisted of the gas diffusion layer (Toray TGP-H-090), a Ni mesh current collector, and an active layer. The active layer was prepared by drop-coating the catalyst ink onto gas diffusion layer. An amount of 20 mg of catalyst was dispersed in a 0.9 mL ethanol/isopropyl alcohol solution (1:1) and a Nafion (5 wt.%, Sigma-Aldrich) stock solution (0.1 mL) in ethanol was added to the dispersion by bath sonication to prepare the catalyst ink. The addition of a small amount of Nafion could effectively improve the dispersion of catalyst suspension and enhance the binding onto the gas diffusion layer. The active layer was controlled to be 18 mm of diameter. It was finally heated at 70 ℃. A meshed CR2032 coin cell (CR2032-CASE-304-MESH, MTI Co.) has been used for the battery test. The electrolyte used in Zn-air cell was 6 M aq. KOH, and a Zn foil (0.25 mm thickness, Alfa Aesar) was used as the anode. Cell test was performed at 25 ℃ using a Biologic VMP3.

4.11 Fabrication of polymer electrolyte membrane fuel cell (PEMFC)

For PEMFC single cell test, catalyst inks were prepared by mixing the catalysts with Nafion (5 wt.%, Sigma-Aldrich) at an ionomer/catalyst ratio = 1/1. The inks were sonicated for 10 minutes and stirred overnight, and then sprayed onto a 5 cm^2 gas diffusion layer (GDL, Toray TGP-H-090). The

anode was Pt/C (20 wt.%) with an excessive Pt loading of 0.4 mg cm^{-2} to ensure sufficient proton supply from the anode. A pair of cathode and anode was hot pressed onto either sides of a N211 (Nafion® , Du Pont) membrane at 130 ℃ for 90 s under pressure 60 lb cm^{-2}. The membrane electrode assembly (MEA) thus produced was tested in a 5 cm^2 PEMEC (Scribner Inc.) at 70 ℃ and room temperature with 100 % relative humidity (RH) and back pressure 2 bars. Pure H2 (100 mL min^{-1}) and O_2 (500 mL min^{-1}) were used as anode and cathode fuels, respectively.

4.12 Results and Discussion

Herein, we would like to report a modern alchemy that converts non-precious Fe-based catalyst to be superior to precious Pt. The Fe-based catalyst was prepared by *in-situ* cocooning Fe nanoparticles in nitrogenated holey two-dimensional structures (Fe@C_2N). The resultant Fe@C_2N displays high catalytic activity with excellent stability in both acidic and alkaline media. For comparison, Pt nanoparticles were also *in-situ* encapsulated in C_2N (Pt@C_2N) using a procedure similar to that used for Fe@C_2N.

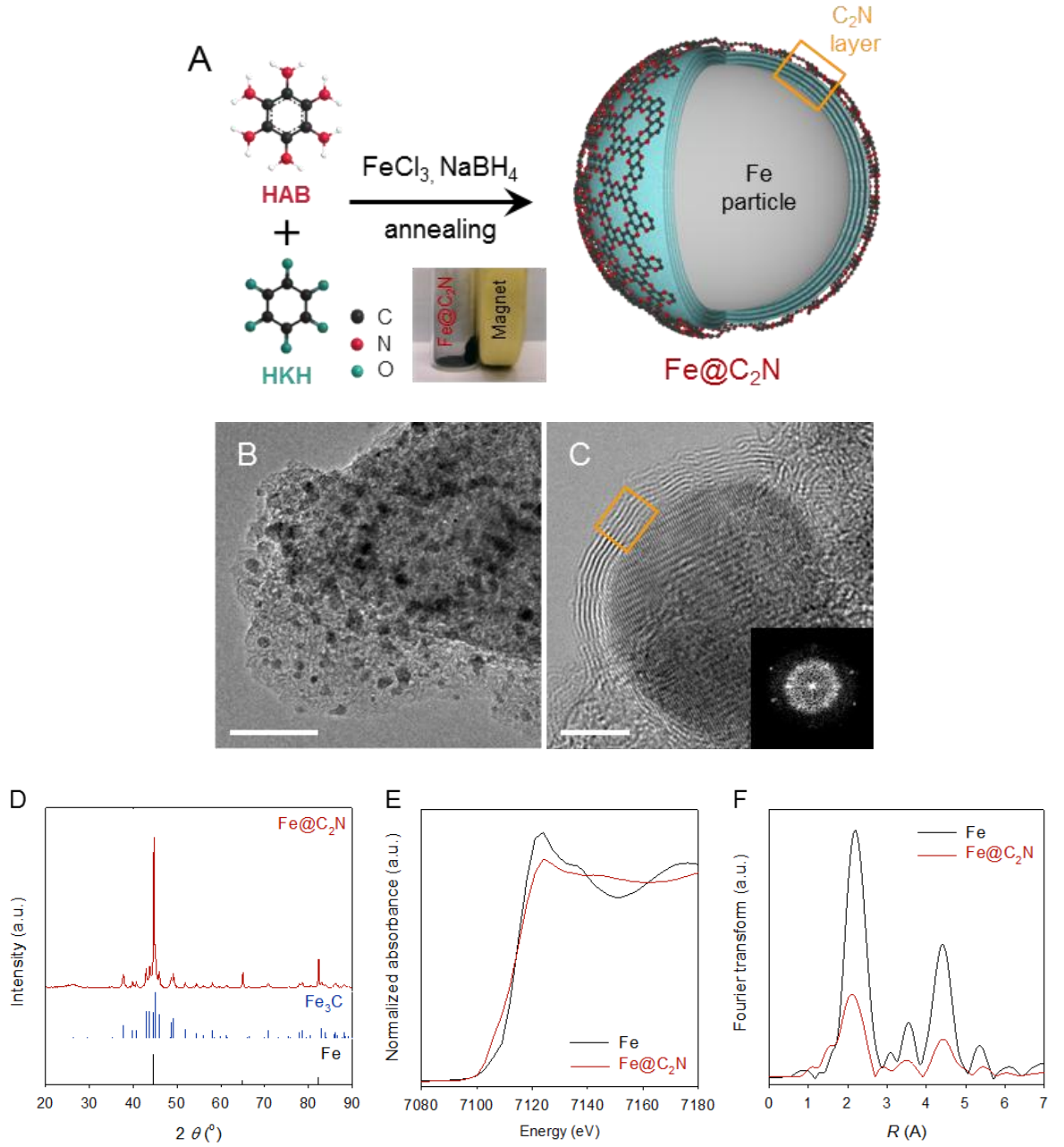

Figure. 4-1. Synthesis and structural characterization of Fe@C_2N. (A) Schematic presentation of the Fe@C_2N synthesis. Inset: behavior of Fe@C_2N in the magnetic field, showing the attraction of the black Fe@C_2N particles toward a magnet and the accumulation of these particles on the side of the glass wall (B) Low-magnification of the HR-TEM image. The scale bar is 100 nm. (C) High-magnification of the HR-TEM image showing the encapsulated Fe nanoparticles. The scale bar is 5 nm. The inset is the fast Fourier transform (FFT) of Fe@C_2N. (D) Powder XRD pattern of the Fe@C_2N compared with those of Fe_3C and pure Fe. (E) X-ray absorption near edge structure (XANES) spectra of Fe@C_2N, Fe and Fe_3O_4. (F) Fourier transform radial distribution of Fe@C_2N, Fe and Fe_3O_4.

As schematically presented in Figure 4-1A, a Fe nanoparticle encapsulated in C_2N (Fe@C_2N) can be synthesized by the polycondensation between hexaketocyclohexane (HKH) and hexaaminobenzene (HAB) trichloride[18] in the presence of iron chloride ($FeCl_3$) as Fe precursor, followed by the subsequent reduction by sodium borohydride ($NaBH_4$). The C_2N stands for the basal plane empirical formula unit of the structure formed. Its morphology consists of evenly distributed holes with six nitrogen surrounding the center of each hole.[19] The resultant Fe@C_2N material is black and displays a strong magnetic response (inset, Figure. 4-1A), indicating the presence of Fe nanoparticles. Energy-dispersive spectroscopy (EDS) combined with scanning electron microscopy (SEM) was used to confirm the elemental composition of Fe@C_2N (Figure. 4-2).

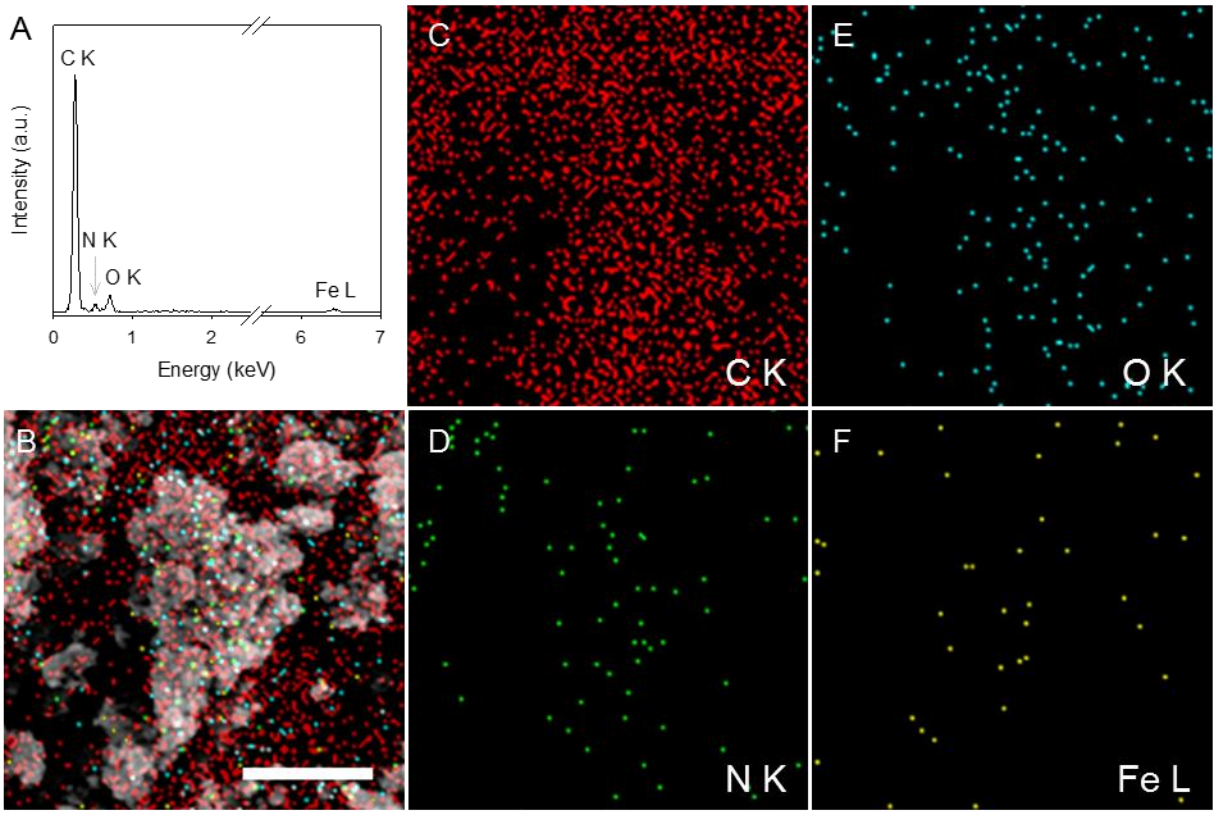

Figure. 4-21. Fe@C_2N energy dispersive X-ray spectroscopy (EDS) spectrum showing the elemental mapping and compositing (C, N, O and Fe) from the SEM image.

A uniform distribution of Fe nanoparticles in the C_2N framework was detected by element mappings in the EDS analysis. EDS (Figure. 4-2A) and XPS (Figure. 4-3) survey spectra of Fe@C_2N revealed the presence of C, N, O (physically adsorbed oxygen and residue of HKH at the edges of C_2N structure) and Fe. Their detailed compositions are summarized in Table 4-1.

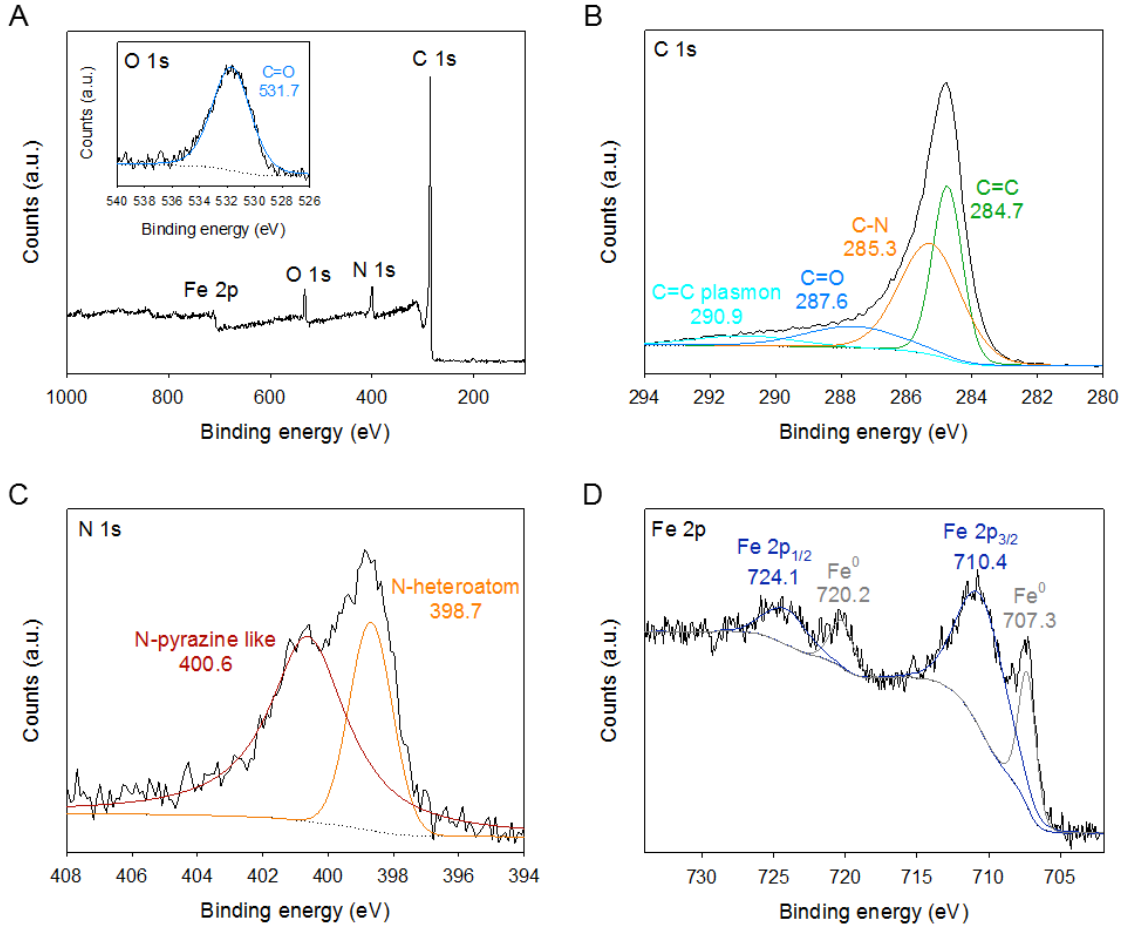

Figugre. 4-3. (A) XPS survey spectrum showing C 1s, Fe 2p, N 1s and O 1s. Inset is deconvoluted O 1s XPS stectrum of Fe@C_2N. Deconvoluted XPS spectra of Fe@C_2N: (B) C 1s; (C) N 1s; (D) Fe 2p. The important peaks identified in the XPS survey spectrum correspond to different chemical states of carbon, nitrogen, oxygen and iron atoms, respectively (Figure. 4-3). High resolution XPS spectra for C 1s, N 1s, O 1s and Fe are shown in the Figure S2. C 1s can be resolved into three major peaks at 284.7 eV (C=C), 285.3 eV (C-N), 287.6 eV (C=O) and 290.9 eV (C-C plasmon) (Figure. 4-3B). There are two peaks of element N 1s in Figure 4-3C. The peak at 398.7 eV corresponds to the binding energy of the N-heteroatom and the peak at 400.6 eV corresponds to the pyrazine like nitrogen in the C2N framework. O 1s is resolved into a peak at 531.7 eV C=O bonds at the edges of C2N structures (inset, Figure 4-3A). The high-resolution XPS spectrum of Fe shows that there are peaks at for the Fe $2p_{3/2}$ and Fe $2p_{1/2}$ suggestive of the presence of metallic iron or its carbides. The peaks at 707.3 eV in the Fe 2p3/2 and 720.2 eV in the Fe $2p_{1/2}$ show that the metallic Fe in Fe@C_2N.

Table 4-1. Elemental composition from different techniques

Technique	C%	Fe%	N%	O%	Total
XPS at.%	66.25	2.93	13.35	17.47	100
EDS (SEM) wt.%	52.31	20.40	14.15	13.14	100
EDS (SEM) at.%	66.47	5.58	15.42	12.53	100

To further investigate the nanostructure of Fe@C_2N, we conducted their high-resolution transmission electron microscopy (HR-TEM). As illustrated in Figure 4-1B, Fe nanoparticles (dark contrast), which have an average diameter of approximately 5-20 nm, are uniformly distributed in the C_2N matrix. At high magnification, the Fe nanoparticles are distinctively encapsulated within C_2N layers (Figure 4-1C). The number of C2N layers varies from 2 to 16 (Figure 4-4). The selected-area electron diffraction (SAED) pattern of the Fe@C_2N can be assigned to diffraction planes of the crystalline structure of the Fe nanoparticles coated with well-defined C_2N layers (inset, Figure 4-1C). The outer C_2N layers can easily be identified along the surface of the core Fe nanoparticles and the interlayer *d*-spacing between C_2N layers is 0.35 nm (Figure 4-4A and Figure 4-4B). This is in good agreement with the XRD results (inset, Figure 4-1D). Furthermore, the cores of the Fe nanoparticles have well-defined crystalline lattice spacing of 0.204 nm (Figure 4-4C and Figure 4-4D) related to the (110) plane of pure Fe crystal. These results ascertain that pure Fe nanoparticles are completely encapsulated in the well-defined C_2N layers, which are protecting Fe nanoparticles from oxidization even after a prolonged exposure to ambient air (over 2 yrs).

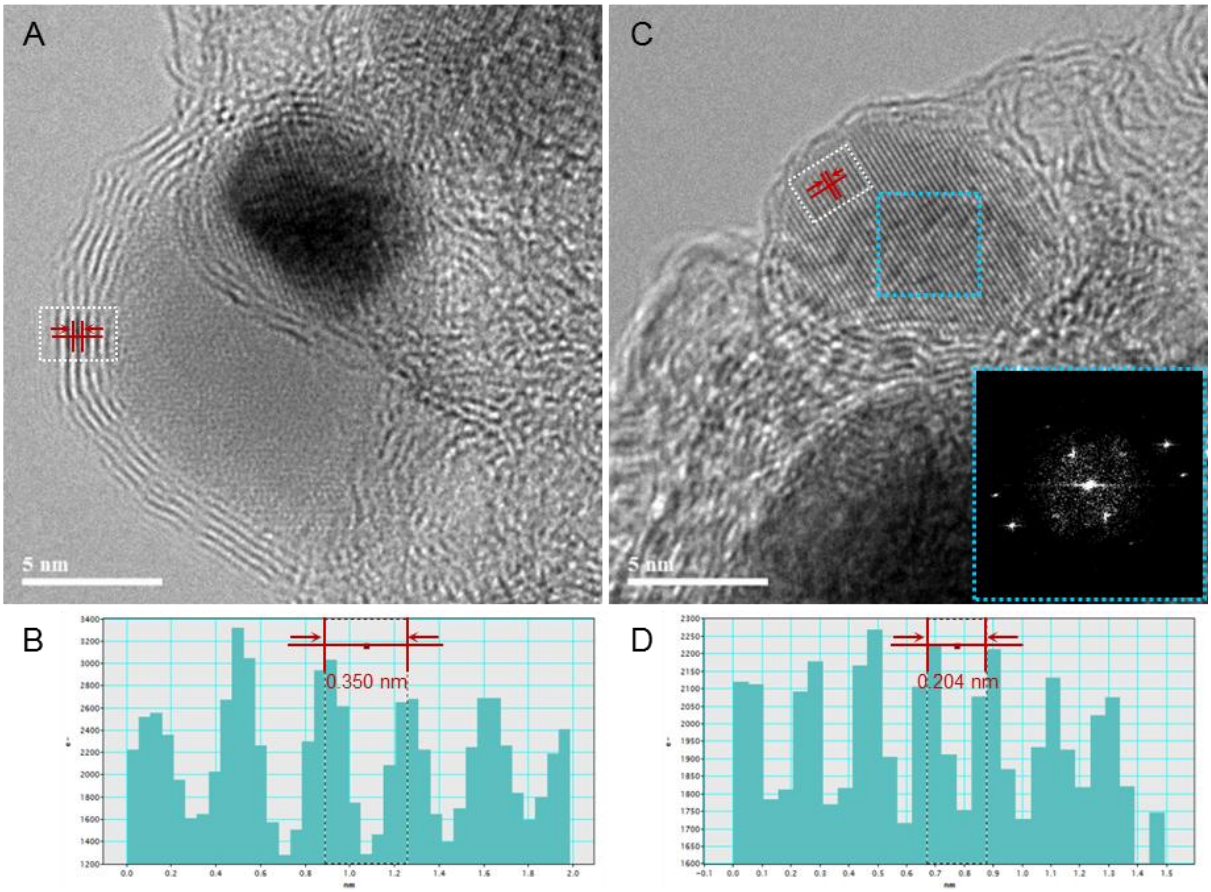

Figure. 4-4. HR-TEM images of as-prepared Fe@C_2N mounted on carbon grid after dispersion in NMP. (A, C) HR-TEM images of as-prepared Fe@C_2N. (B, D) Inter layer distance from the red marked line, respectively. Inset of (C) is the fast Fourier transform (FFT) of marked blue dot square.

The porosity of Fe@C_2N was measured by the Brunauer-Emmett-Teller (BET) method. The specific surface area of the Fe@C_2N is approximately 584 m2 g-1 with a pore volume of 1.1142 cm^3 g-1 and an average pore diameter of 7.6 nm (Figure 4-5). There is an uptake at low pressure range, which is characteristic of microporous materials. The isotherm of the Fe@C_2N also shows a clear uptake at high pressure and a capillary condensation step at P/P_o = 0.9-1.0. The uptake occurring at low pressure is attributed to presence of micropores and the capillary condensation is ascribed to mesopores. Moreover, the nitrogen adsorption-desorption isotherms exhibit a hysteresis loop of type IV according to IUPAC classification and display a pronounced hysteresis for partial pressures P/Po > 0.45, indicating the presence of slit shape pores between the layers.

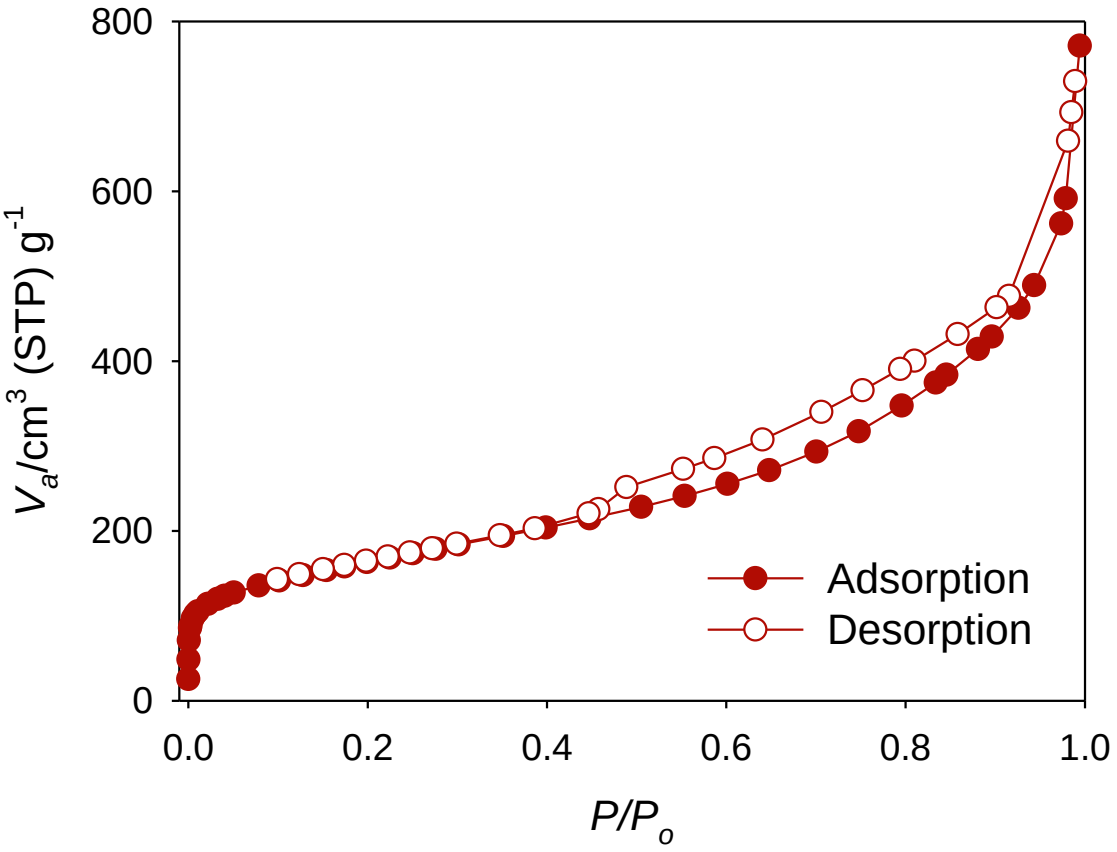

Figure 4-5. Nitrogen adsorption and desorption isotherms for the Fe@C_2N. The Brunauer-Emmett-Teller (BET) specific surface area is approximately 584 m^2 g^{-1} which is quite high. The nitrogen adsorption-desorption isotherms exhibit a hysteresis loop of type H4 indicating the presence of slit like pores between the layers.

The X-ray diffraction (XRD) patterns of the prepared Fe@C_2N shows a peak at 26.1° (2θ°), which is related to the (002) plane of the C_2N structure (Figure 4-1D). The peaks at 44.7, 65.0 and 82.3° are characteristic of metallic iron (JCPDS 87-0721).[20] The minor diffraction peaks are related to the Fe_3C species (JCPDS 72-1110).[21] Therefore, the XRD results validate that strong binding exists at the boundary between the Fe cores and the C_2N shells, as indicated by TEM analysis (Figure 4-1B and Figure 4-1C). Extended X-ray absorption fine structure (EXAFS) measurements of the Fe@C_2N were also recorded to further ascertain the metallic nature of the Fe in the Fe@C_2N. Figure 4-1E shows the X-ray absorption near edge structure (XANES) spectra for Fe@C_2N together with those for Fe as references. Bond lengths (R), coordination number (CN), disorder (Debye-Waller factor) and atomic

species around the X-ray absorbing atoms are summarized in Table 4-2. The weak fluctuation for Fe@C_2N compared with reference samples are an evidence of the well encapsulation of Fe atoms by C_2N layers. Figure 4-1F represents the magnitude of the Fourier transform with the distance from the absorbing atom. In the case of Fe reference, the interatomic distances (R) of the first shell and second shell related to Fe–Fe are 2.48 and 2.87 Å, respectively (Table 4-2). On the other hand, R of the first shell of Fe–O in the reference Fe_3O_4 is 2.04 Å. For Fe@C_2N, the distances (R) of the first and second shells corresponding to Fe–Fe are 2.47 and 2.88 Å, respectively and R of the shell corresponding to Fe-C is 2.56 Å. Considering the interatomic distance, the iron in the Fe@C_2N exists as a pure metallic iron rather than iron oxides (Fe_xO_y) with very small amount of iron carbide at the C_2N and iron nanoparticle interface indicating strong interaction between the particle and the encapsulating C_2N layers. The quantitative results of Fe@C_2N obtained from curve fitting radial distribution functions are listed in Table 4-2. These results reveal a complete encapsulation of the metallic Fe nanoparticles inside the C_2N layers, preventing the oxidation/dissociation of unstable Fe nanoparticles even after a prolonged exposure to electrochemical conditions.

Table 4-2. Phase-shift corrected structural parameters obtained from the curve fitting of EXAFS spectrum for Fe@C_2N obtained at the Fe K-edge and compared with Fe and Fe_2O_4

Samples	Bonds	R(Å)[a]	*CN*[b]	$\Delta E_{0\,(eV)}$[c]	σ^2 (Å^2)[d]	R-factor
Fe	Fe-Fe	2.48	8.0	-6.72	0.003701	0.01416
	Fe-Fe	2.87	6.0			
Fe_3O_4	Fe-O	2.04	4.0	2.80	0.010741	0.00389
Fe@C_2N	Fe-Fe	2.47	3.39	-10.15	0.003016	0.041
	Fe-Fe	2.88	0.48	-8.44	0.003015	
	Fe-C	2.56	1.68	-9.28	0.00297	

[a]Interatomic distance, [b]Coordination number, [c]Energy shift. [d]Debye Waller factor.

Given the well-defined structure identification of Fe@C_2N, its oxygen reduction reaction (ORR) activity was evaluated using cyclic voltammetry (CV) in both 0.1 M aq. KOH and 0.5 M aq. H_2SO_4 solutions. For comparison, the ORR effectiveness of a commercial 20 wt.% Pt/C (Vulcan XC-72R, E-TEK) was also carried out under the same environment. The same mass of each material was loaded onto a glassy electrode (0.1 mg cm^{-2}). The electrocatalytic activity can be estimated by the capacitance from the cyclic voltammogram. To understand the principle element in Fe@C_2N for unusual ORR behavior, a series of comparative CV experiments were conducted. CVs of the samples were performed on glassy carbon electrode with a scan rate of 10 mV s^{-1}, both in N_2 and O_2 saturated 0.1 M aq. KOH solutions (Figure 4-6A). In O_2-saturated 0.1 M aq. KOH solution, the capacitance of the Fe@C_2N and Pt/C are 145.7 and 94.7 F g^{-1}, respectively (Table 4-3). In nitrogen-saturated 0.1 M aq. KOH solution, the capacitance (131.8 F g^{-1}) of Fe@C_2N is also much higher than that (83.1 F g^{-1}) of Pt/C (Table 4-3). In O_2-saturated 0.5 M aq. H_2SO_4 solution (Figure 4-6B), the capacitance of the Fe@C_2N is 150.9 F g^{-1} and that of Pt/C is 80.2 F g^{-1} (Table 4-3). In nitrogen-saturated 0.5 M aq. H_2SO_4 solution, the capacitances are 121.4 and 66.7 F g^{-1}, respectively, for Fe@C_2N and Pt/C (Table 4-3).

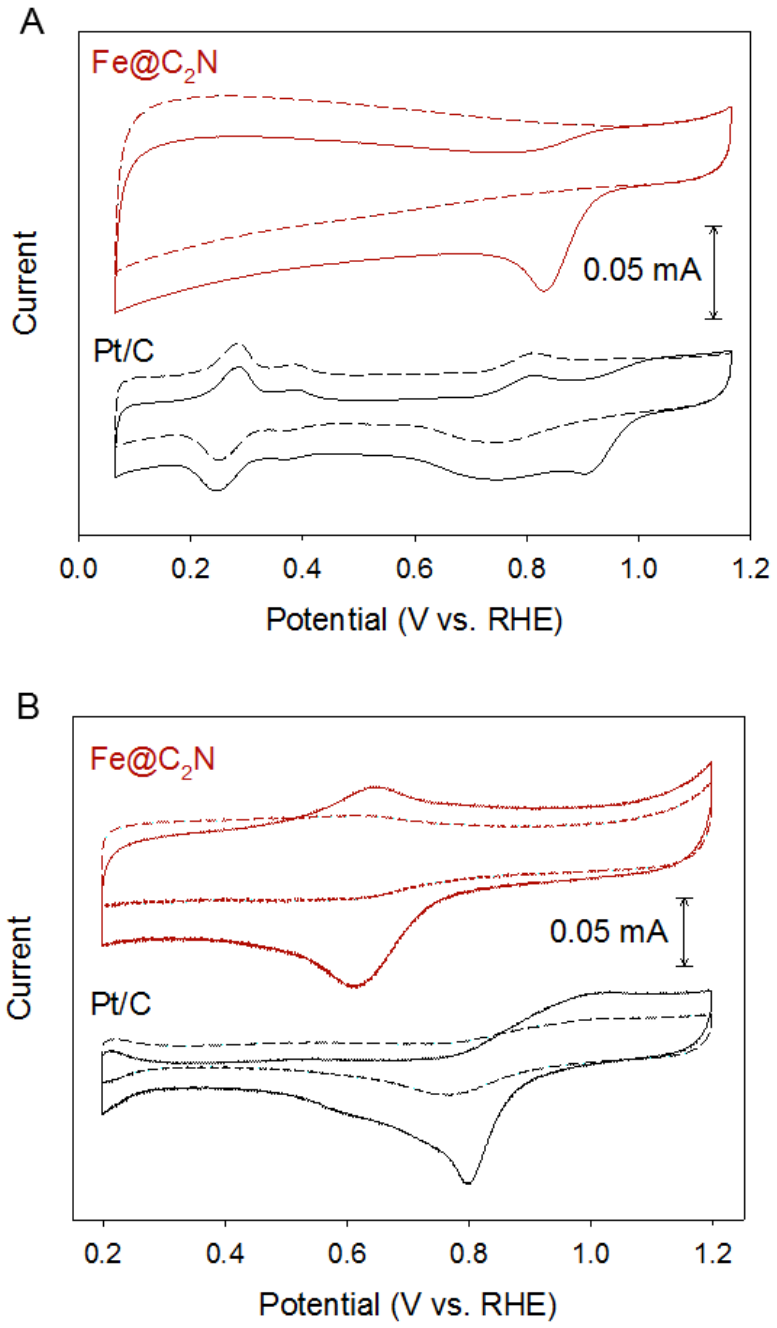

Figure 4-6. Cyclic voltammograms of Pt/C and Fe@C_2N in O_2-saturated (solid line) and N_2-saturated conditions: (A) 0.1 M KOH; (B) 0.5 M H_2SO_4 solution. The scan rate was 0.01 V s^{-1}.

Table 4-3. Capacitance of the commercial Pt/C and of $Fe@C_2N$

Electrolyte	Condition	Capacitance ($F\ g^{-1}$)	
		Pt/C	$Fe@C_2N$
0.1 M KOH	O_2	94.7	145.7
	N_2	83.1	131.8
0.5 M H_2SO_4	O_2	80.2	150.89
	N_2	66.7	121.4

To further verify the selectivity of the 4*e* reduction pathways for oxygen reduction at $Fe@C_2N$ and Pt/C, we performed rotating ring-disk electrode (RRDE) measurements to examine the generation of peroxide species during ORR process in both alkaline and acidic media (Figure 4-7A and Figure 4-7B).[22] Remarkably, the peroxide species (HO_2^-) yield of $Fe@C_2N$ catalyst remained below ~10% at all potentials in alkaline medium (0.1 M aq. KOH) and decreased to the same value as that measured for commercial Pt/C at 0.66 V, corresponding to an electron transfer number of 3.88 (Figure 4-7A). In acidic medium (0.5M aq. H_2SO_4), the measured H_2O_2 yields are below ~9% and ~5% for $Fe@C_2N$ and Pt/C, respectively, over the potential range of 0.2 ~ 0.8 V, indicating electron transfer number of ~3.8 (Figure 4-7B).

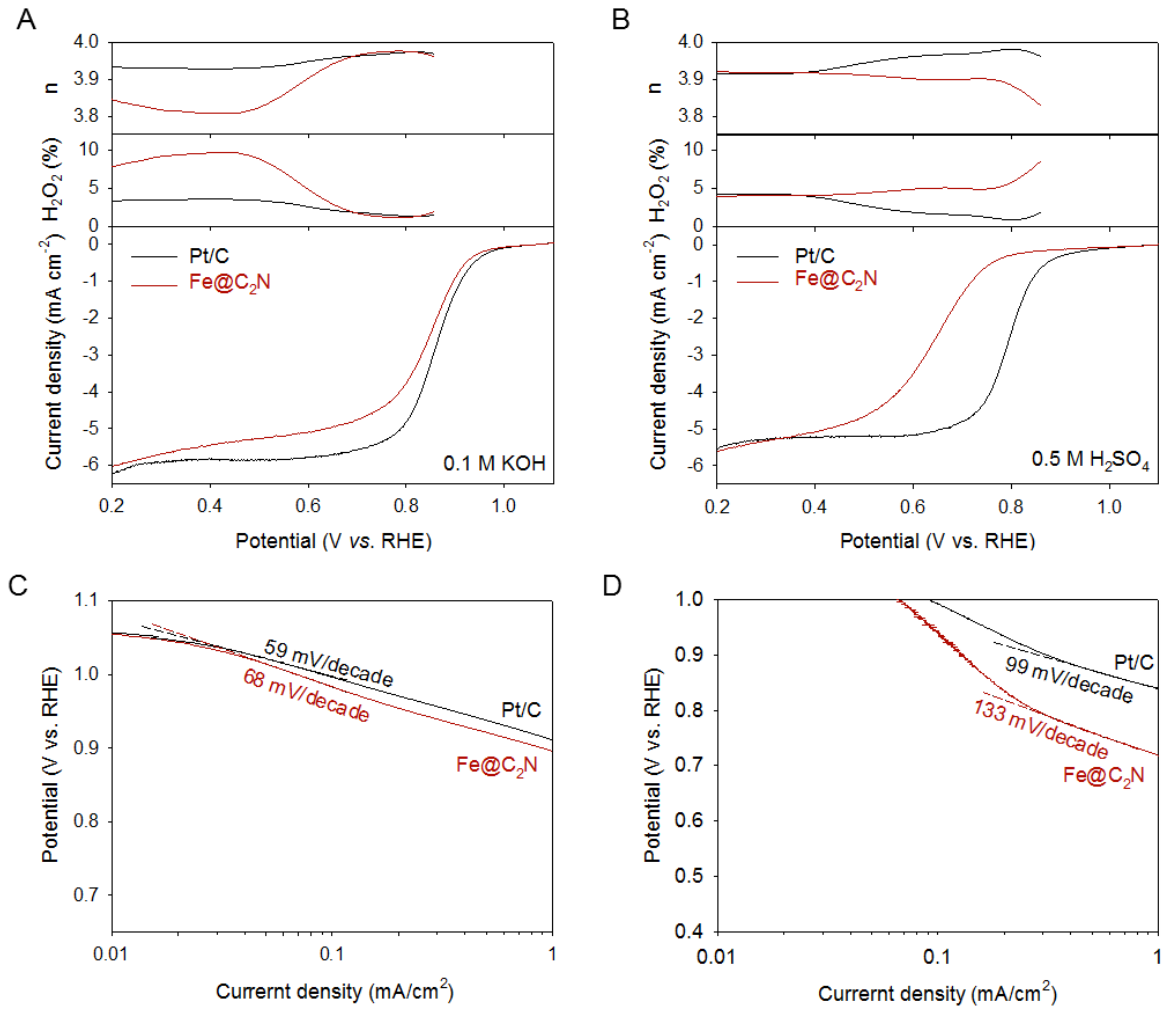

Figure 4-7. Electrochemical evaluation of Fe@C_2N. (A, B) Rotating ring-disk electrode (RRDE) voltammograms (bottom), percentage of peroxide (middle) and electron transfer number (*n*) (top) recorded with Fe@C_2N and Pt/C at 1,600 rpm in O_2-saturated conditions: (A) 0.1 M aq. KOH solution and (B) 0.5 M aq. H_2SO_4 solution. The disk potential was scanned at 10 mV s^{-1} and the ring potential was constant at 1.4 V *vs.* RHE. Tafel plots were obtained by mass-transport correction of corresponding RDE measurements at 1,600 rpm in O_2-saturated conditions: (C) 0.1 M aq. KOH solution and (D) 0.5 M H_2SO_4 solution. The catalyst loading was 0.795 mg cm^{-2} (159 μgPt cm^{-2}).

To further examine the kinetics of electrochemical catalytic ORR at Fe@C_2N and Pt/C electrodes, rotating disk electrode (RDE) measurements were performed. The polarization curves were recorded by scanning the potential range from 1.16 to 0.06 V at a scan rate of 10 mV s^{-1} with different rotation frequency (Figure 4-8). The current increases with respect to rotation rate owing to the shortened diffusion distance. The onset potential is located at 0.92 V for Fe@C_2N electrode in 0.1 M aq. KOH,

approaching near to that of Pt/C electrode (0.97 V). Analysis of the steady-state diffusion currents through Koutechy-Levich (K-L) plots indicated good linearity with parallelism, suggesting a first order dependence of the dissolved O_2 reduction kinetics on the electrodes and similar electron transfer numbers for ORR at different potentials (Figure 4-8B and Figure 4-8E). From the K-L equation, the numbers of electrons transferred for ORR at Fe@C_2N and Pt/C electrodes were determined to be about 3.88 and 3.98 in 0.1 M KOH (Figs. S6B and S6C) and 3.99 and 3.87 in 0.5 M H_2SO_4 (Figure 4-8 and Figure 4-8F) respectively, demonstrating that the ORR in Fe@C2N and Pt/C electrodes predominantly proceeds with an ideal four electron (4*e*) reaction process. In addition, the kinetic current of Fe@C_2N was -0.28 mA at 1600 rpm at 0.06 V, which is slightly higher than that of Pt/C catalyst (-0.27 mA). This enhanced kinetic current at the Fe@C2N electrode symbolizes the improved dynamics for the ORR relative to the Pt/C catalyst. The efficient ORR activity of the Fe@C_2N was also observed from the smaller Tafel slope of 68 mV Dec.$^{-1}$ for Fe@C_2N in 0.1 M aq. KOH solution, which is comparable to the ~59 mV Dec.$^{-1}$ of the commercial Pt/C (Figure 4-7C). In 0.5 M aq. H_2SO_4 solution, the Tafel slope of kinetic current was 133 mV Dec.$^{-1}$ for Fe@C_2N and 99 mV Dec.$^{-1}$ for Pt/C (Figure 4-7D).

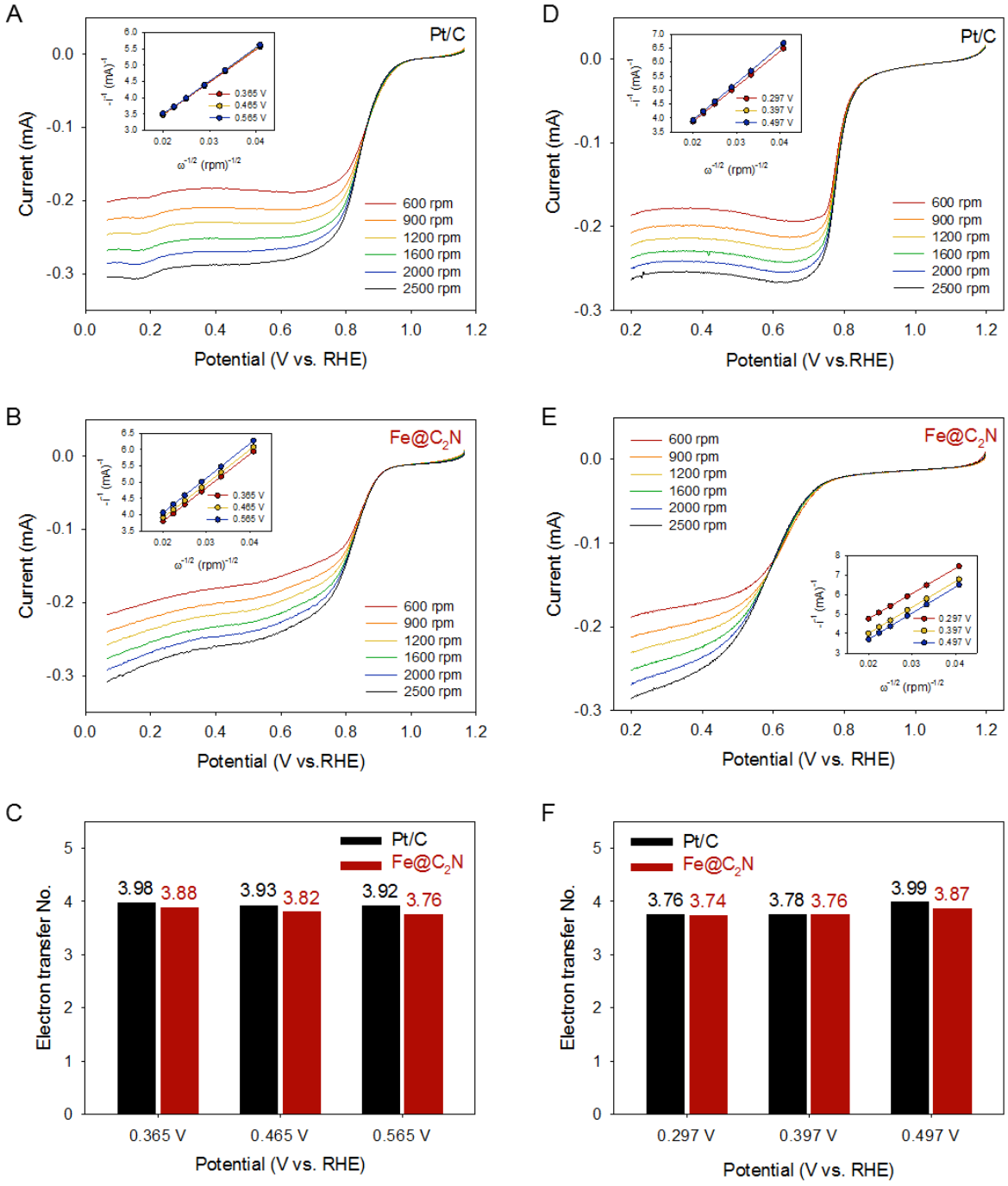

Figure 4-8. Polarization curves on a glassy carbon RDE voltammograms for Pt/C and Fe@C_2N in O_2-saturated (A,B) 0.1 M aq KOH solution and (D,E) 0.5 M aq H_2SO_4 with a scan rate of 0.01 V s^{-1} at different rotating rates of 600, 900, 1200, 1600, 2000, and 2500 rpm. Inset is Koutecky-Levich plots for each electrodes. (C,F) Electron transfer numbers of PtC and Fe@C_2N as a function of the electrode potential in O_2-saturated (C) 0.1 M aq KOH solution and (F) 0.5 M aq H_2SO_4 solution.

Cycle stability of the samples before and after 100,000 cycles (~ one month) in 0.1 M aq. KOH and 0.5 M aq. H_2SO_4 solutions were also performed (Figure 4-9A and Figure 4-9B). In case of O_2^- saturated 0.1 M aq. KOH solution, the current retention of Fe@C_2N is 92.7%, while Pt/C decreases to 50.7% after 100,000 cycles (Figure 4-9A and Table 4-4). The current retention for Fe@C_2N in 0.5 M aq. H_2SO_4 is 95.2% in O_2 saturated conditions, while that of Pt/C retains only 27.3% in O_2 saturated condition after 100,000 cycles (Figure 4-9B and Table 4-5). Furthermore, the fuel crossover effect on the ORR activity of Fe@C_2N was evaluated in the presence and absence of methanol. It has a serious influence on the ORR activity of Pt/C, while there is almost no effect on Fe@C_2N (Figure 4-10). These results are indicative of promising activities for Fe@C_2N as a stable ORR catalyst in direct methanol fuel cells (DMFCs). On the basis of the observed results, the overall performance of Fe@C_2N as cathode catalyst for ORR is almost equivalent to that of Pt/C. More importantly, long-term stability is critical for practical use. In this regard, Fe@C_2N is superior to commercial Pt/C in both acid and basic electrolytes.

The origin high catalytic activity and stability of Fe@C_2N could be anticipated by recent study on the basis of density functional theory (DFT) calculations. The tunneling effect can be observed even through thin insulating layers around the metal core but diminishes with the increased thickness.[23] Close interface combined with electron tunneling from the underneath metal particles, activate the adsorbed O_2. On the other hand, the thin encapsulating C_2N layers prevents the strong coordination between ligands (such as carbon monoxide (CO) and cyanide ($^-$CN)) and transition metal (such as Fe and Pt) surfaces, thereby protecting the metal surface from CO and $^-$CN coordination, which lead to activity and stability losses.[23] The high degree of catalytic properties could be associated to the synergic effects from the core Fe nanoparticles encapsulated in C_2N layers with uniformly distributed holes and nitrogen atoms, allowing efficient electron tunneling and Fe encapsulation. In addition to the high ORR activity and enhanced kinetics of Fe@C_2N *vs*. Pt/C, the synthetic protocol is simple and the process could be easily scale up for mass production.

The higher activity and durability of the Fe@C_2N as ORR catalyst can be mainly ascribed to the following aspects. The well-ordered nanoporous structure of the C_2N framework of the Fe@C_2N provides excellent mass transport properties. The electrochemical reaction (ORR) usually involves a heterogeneous phenomenon at the triple phase boundary, requiring oxygen diffusion (contact), electrolyte and solid catalyst. Faster and active exchange of gas and the electrolyte at the catalyst surface could expedite the ORR process. The superior activity and durability of Fe@C_2N catalyst can be explained by a synergic interaction between the reactive Fe nanoparticles and the protective C_2N layers. Particularly, the encapsulated Fe nanoparticles communicate with the surrounding C_2N layers, making the outer surface of the C_2N layers active towards the ORR, despite of the fact that the encased Fe nanoparticles are not in direct contact with the corrosive electrolyte.[24] This assumption

was evidenced by poisoning test with one of strongest ligands and TEM observations. Poisoning tests using CN^- for alkaline medium and SCN^- for acidic medium were conducted on Fe@C_2N (Figure 4-9C and Figure 4-9D) and on Pt/C (Figure 4-11). It was clear that Fe@C_2N has little effect with/without presence of CN^- and SCN^- (Figure 4-9C and Figure 4-9D), while Pt/C showed dramatic activity decay in both media (Figure 4-11A and Figure 4-11B). This result suggests that Fe nanoparticles in Fe@C_2N are indeed protected by C_2N layers. High-resolution TEM observation could visually confirm the stability of Fe@C_2N (Figure 4-12). Although Fe nanoparticles are very susceptible to oxidation, there are no noticeable morphology changes even after 100,000 chronoamperometric cycles.

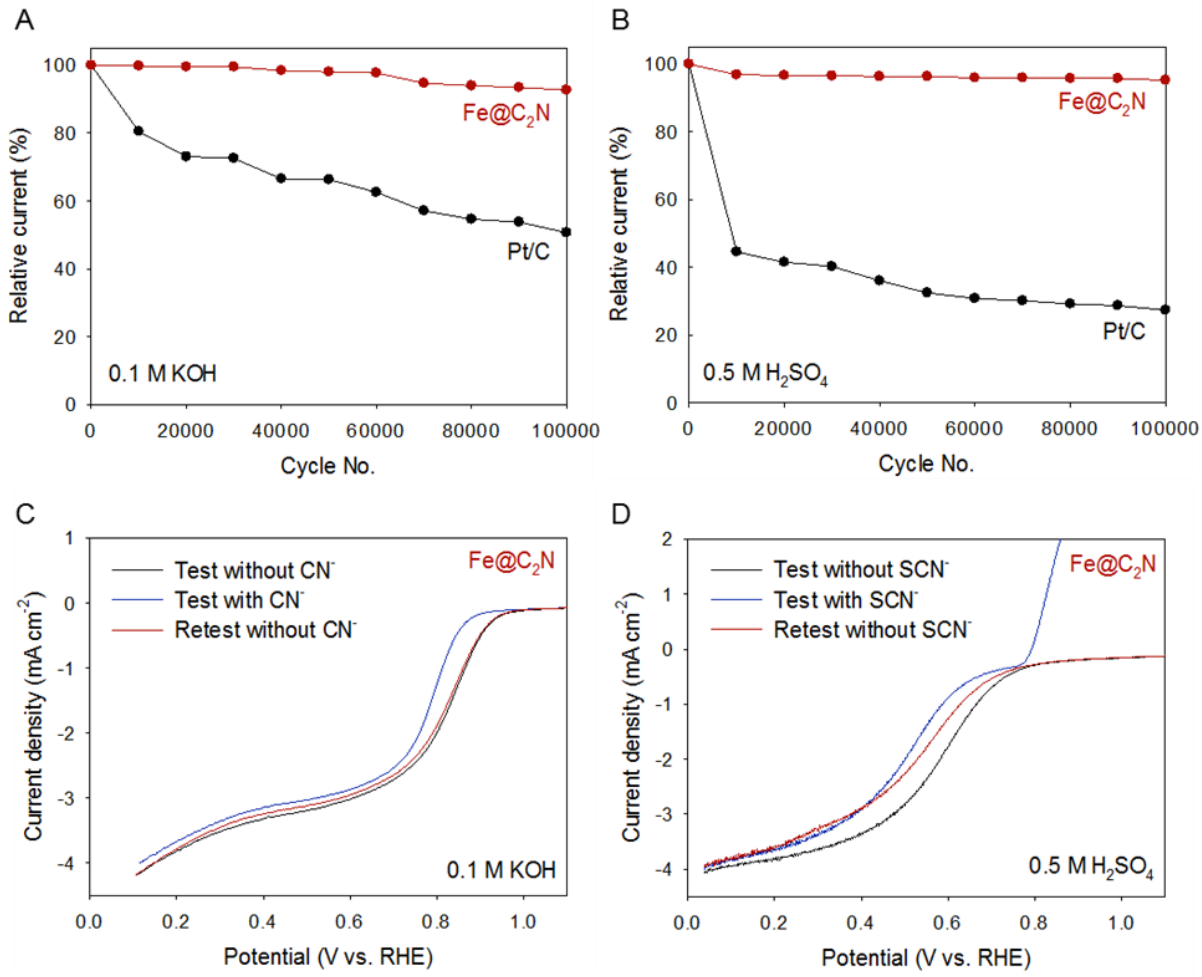

Figure 4-9. Durability and impurity tolerance of $Fe@C_2N$. (A) Current variation with respect to cycling number for $Fe@C_2N$ and Pt/C in O_2-saturated conditions: (A) 0.1 M aq. KOH solution and (B) 0.5 M aq. H_2SO_4 solution. Durability test was accelerated as a function of cycle number up to 100,000. RDE polarization curves for $Fe@C_2N$ in O_2-saturated conditions: (C) 0.1 M aq. KOH solution and (D) 0.5 M aq. H_2SO_4 solution, tested without 10 mM CN^- or SCN^- (black line), with 10 mM CN^- or SCN^- (blue line) and retested without CN^- or SCN^- (red line).

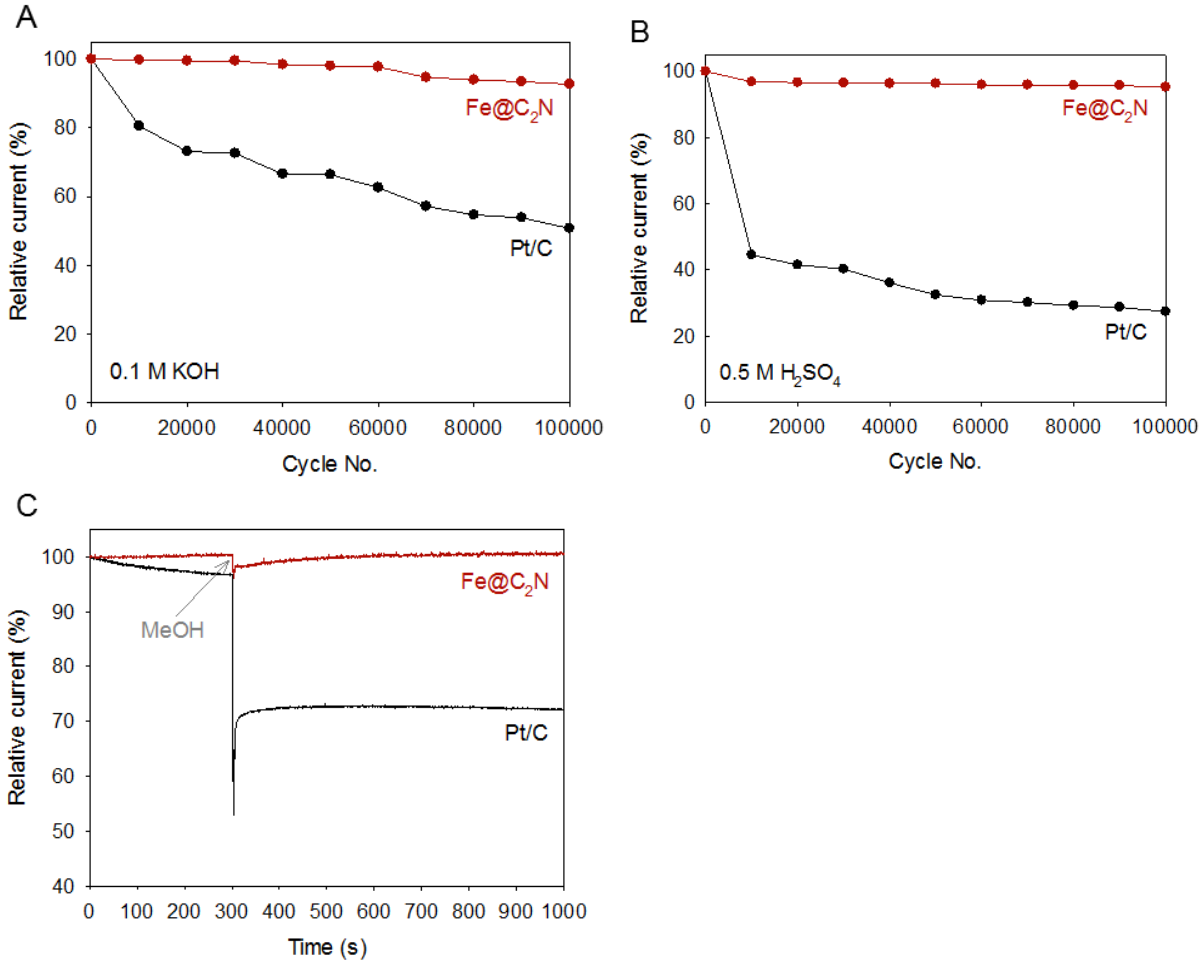

Figure 4-10. Durability and impurity tolerance of Fe@C_2N. (A) Current variation with respect to cycling number for Fe@C_2N and Pt/C in O_2-saturated conditions: (A) 0.1 M aq. KOH solution and (B) 0.5 M aq. H_2SO_4 solution. Durability test was accelerated as a function of cycle number up to 100,000. RDE polarization curves for Fe@C_2N in O_2-saturated conditions: (C)The current–time (*j*–t) chronoamperometric response at 0.5 V (*vs.* RHE) at a rotation rate of 2,500 rpm in 0.1 M aq. KOH with the addition of 3 M methanol (2 mL).

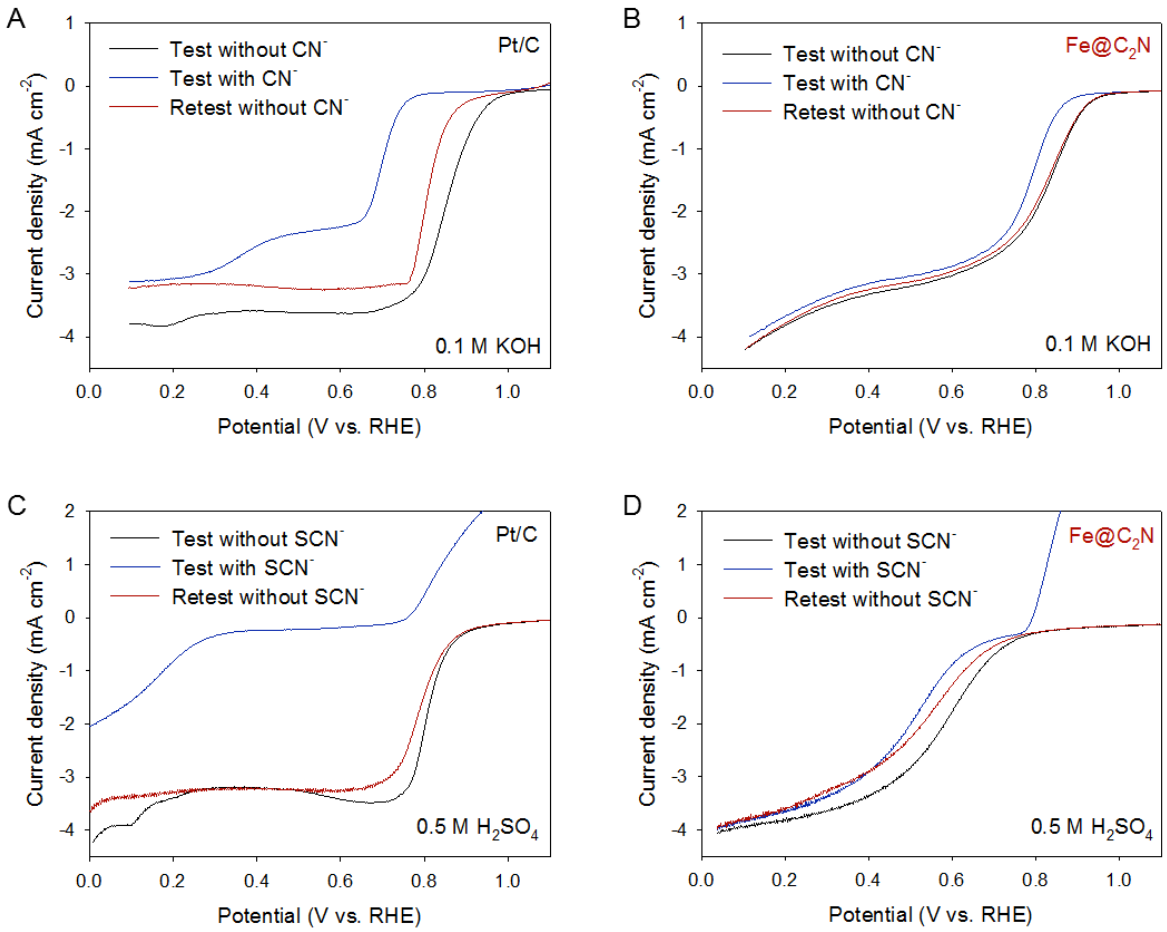

Figure 4-11. RDE polarization curves for (A,C) Pt/C and (B,D) Fe@C_2N in O_2-saturated (A,B) 0.1 M aq KOH solution or (C,D) 0.5 M aq H_2SO_4 solution tested without 10 mM CN^-(black line), with 10 mM CN^-(blue line) or retested without CN^-(red line).

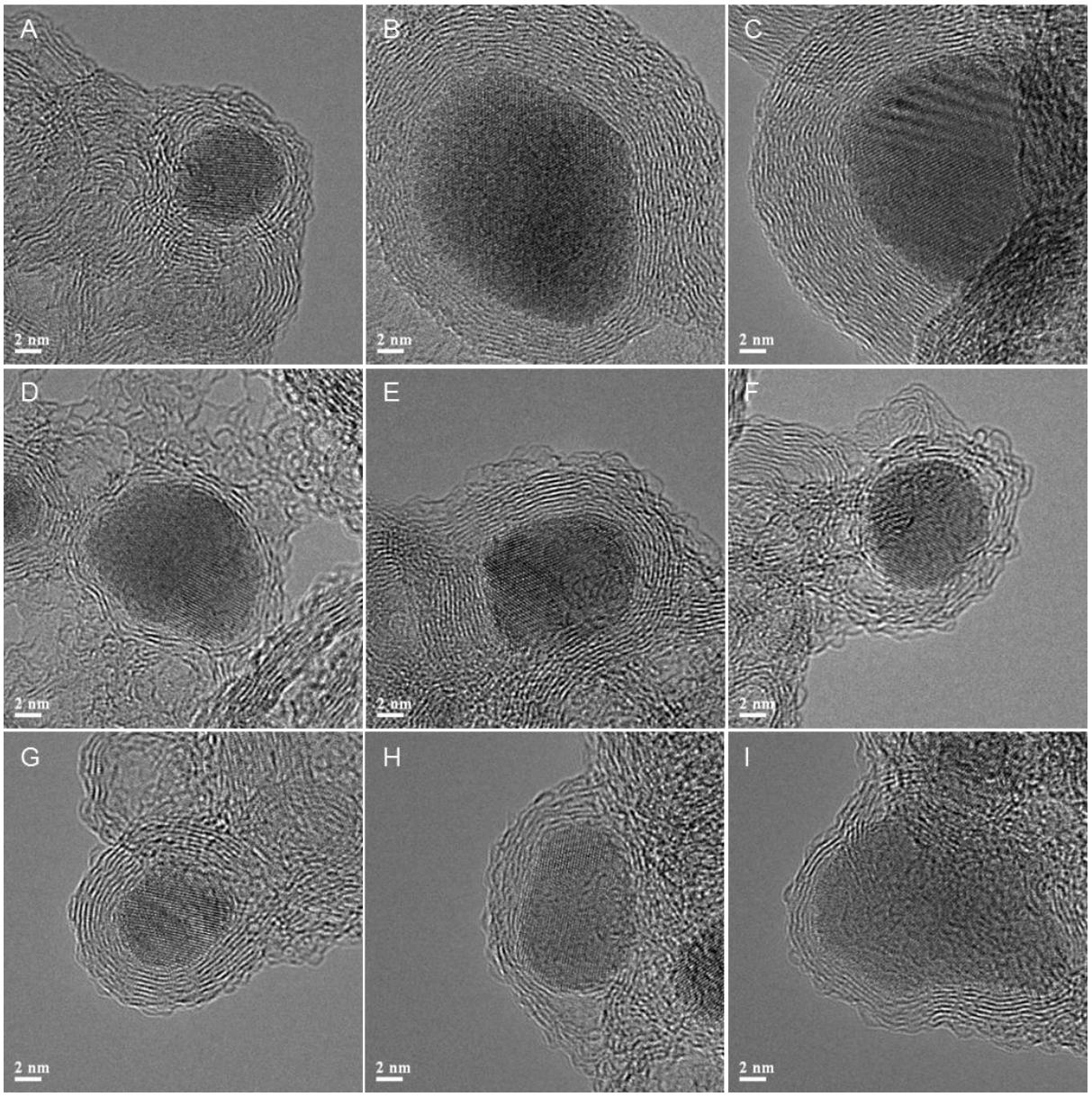

Figure 4-12. HR-TEM images of Fe@C_2N: (A, B, C) Before chronoamperometric cycles. (D, E, F) After 100,000 chronoamperometric cycles in 0.1 M aq KOH solution. (G, H, I) After 100,000 chronoamperometric cycles in 0.5 M aq H_2SO_4 solution.

On the basis of ORR performance of Fe@C_2N, full cell performance was evaluated by lithium (Li)-air cell, which is probably one of the most promising metal-air cells with a high storage capacity nearly ten times that of the state-of-the-art Li-ion battery.[25] Figure 4-13A shows the first discharge-charge curves of Fe@C2N and Pt/C at a current density of 0.5 mA cm^{-2} in hybrid Li-air cell. Discharge voltage plateaus are obtained at 2.92 and 2.94 V *vs.* Li/Li+ for Fe@C_2N and Pt/C, respectively. As expected from the ORR kinetics by the linear sweep voltammetry (LSV) results in Figure 4-7, the discharge voltage of Fe@C_2N is comparable with that of Pt/C due to excellent electrochemical activity of Fe@C_2N in alkaline medium.

The discharge profiles were further investigated at a higher current density in the range of 0.5 to 2.0 mA cm^{-2} (Figure 4-13B). At a current density of 0.5 mA cm^{-2}, the discharge voltage of Fe@C_2N is similar with that of Pt/C. By increasing the current density, however, the voltage gap between Fe@C_2N and Pt/C becomes larger, indicating that the Fe@C_2N has exceptional electrocatalytic activity for ORR even in higher current region. Furthermore, the cell using Fe@C_2N electrode exhibits excellent cycling stability during 20 h operation without any degradation of the performance at a constant current density of 0.1 mA cm^{-2} in ambient air (Figure 4-13C). The result indicates that Fe@C_2N provides not only excellent ORR but also outstanding oxygen evolution reaction (OER). Therefore, Fe@C_2N can be considered a remarkable bi-functional catalyst for both ORR and OER at the same time.

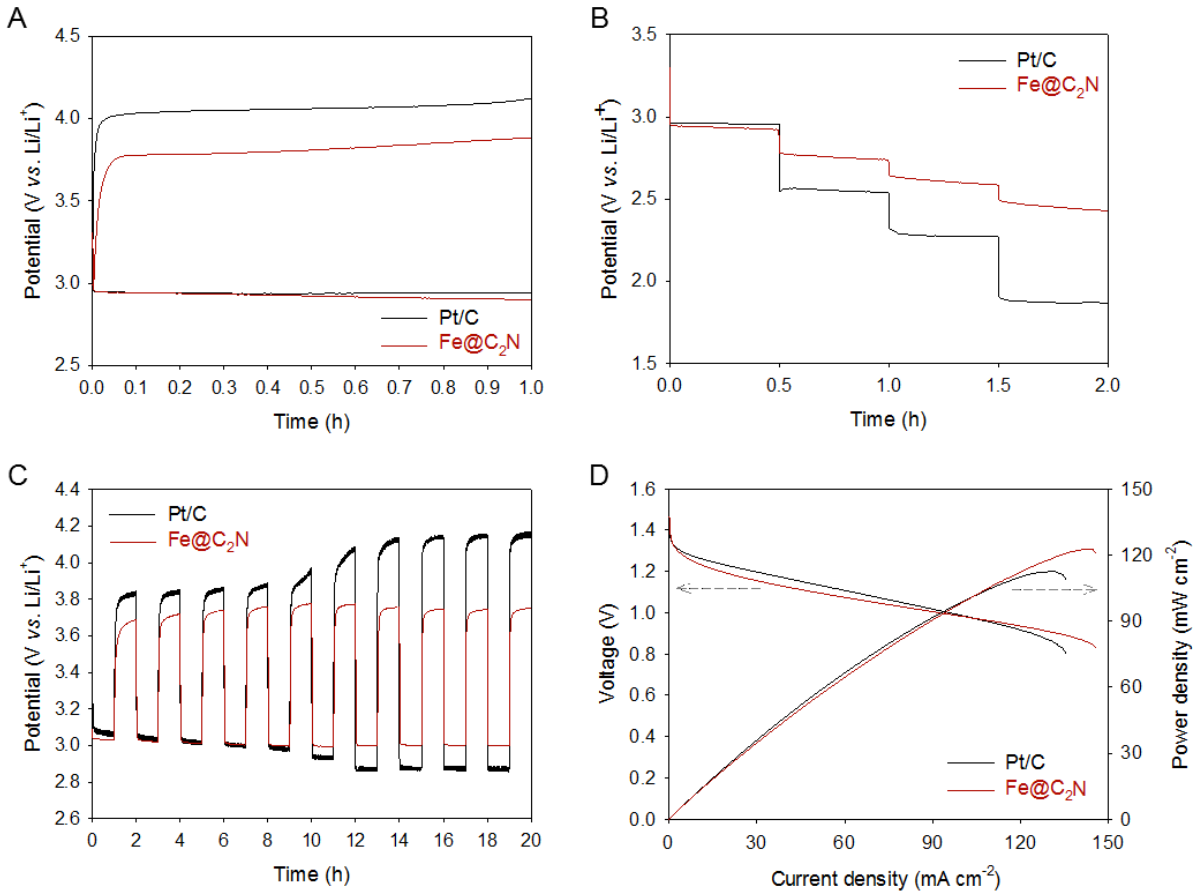

Figure 4-13. Full cell test of Fe@C_2N. (A) First discharge-charge curves of Fe@C_2N and Pt/C at current density of 0.5 mA cm^{-2}. (B) Discharge voltage profiles with different current density in the range of 0.5 to 2.0 mA cm^{-2}. (C) Cycling performance of three-electrode hybrid Li-air cell using Fe@C_2N and Pt/C at current density of 0.1 mA cm^{-2}. (D) Polarization and power density curves of Zn–air cells using Fe@C_2N and Pt/C as catalysts (mass loading = 1.0 mg cm^{-2}) and 6 M aq. KOH electrolyte (scan rate: 10 mV s^{-1}).

As the Fe@C_2N displayed outstanding ORR performance, zinc (Zn)-air cells[26] were also fabricated using Fe@C_2N-based air cathodes. The polarization and power density curves of a primary Zn–air cell using Fe@C_2N and Pt/C as electro-catalysts are shown in Figure 4-13. The open-circuit voltage (OCV) of Fe@C_2N and Pt/C is around 1.47 V and 1.45, respectively. These values are quite similar to that of the theoretical value of a Zn-air cell.[27] The maximum power density provided by the Zn–air cell using the Fe@C_2N catalyst is 123 mW cm^{-2} at 143 mA cm^{-2}. This power generation property is even better than that of Pt/C (112 mW cm^{-2} at 128 mA cm^{-2}), indicating that Fe@C_2N demonstrates superior electrocatalytic properties for ORR compared with commercial Pt/C in Zn-air cell. The Fe@C_2N catalyst displayed somewhat lower activity compared to Pt/C in the RDE experiment of Figure 4-7A, but it showed enhanced performance compared to that of Pt/C in actual Zn-air cell tests. The major reason is due to the holey C_2N coat on Fe nanoparticles, providing a perfect protection and an enhanced conductivity to the reactive Fe and a high surface area (Figure 4-5) for the Fe@C_2N-based catalyst. The other reason could be the difference of the concentration of KOH in RDE and in a real air cell test. The ORR was measured using RDE in 0.1 M aq. KOH, while Zn-air cells were tested in 6 M aq. KOH. The high concentration of KOH is necessary to obtain a high electrical conductivity in a practical device (Zn-air cell). Although Fe@C_2N catalyst showed a slightly lower activity than Pt/C in RDE test, the non-noble catalyst displays a low electrical resistance and a favorable mass transfer, due to the holey C_2N layers on Fe nanoparticles, leading to improved activity and durability for the Fe@C_2N catalyst in Zn-air cells. Consequently, Fe@C_2N catalyst is able to exhibit better activity than Pt/C, enlightening the promise to replace precious-metal-based catalysts for rechargeable Zn-air cells.

We also tested the Fe@C_2N as a cathode catalyst in polymer electrolyte membrane fuel cell (PEMFC).[28] The polarization and power density curves of the membrane electrode assemblies (MEAs) that employed Fe@C_2N or Pt/C as a cathode catalyst are presented in Figure 4-14. The yet-to-optimize Fe@C_2N cathode generated over 80% of power densities at 70 ℃ (>82%) and room temperature (>85%) compared with well-optimized Pt/C cathode in PEMFC.

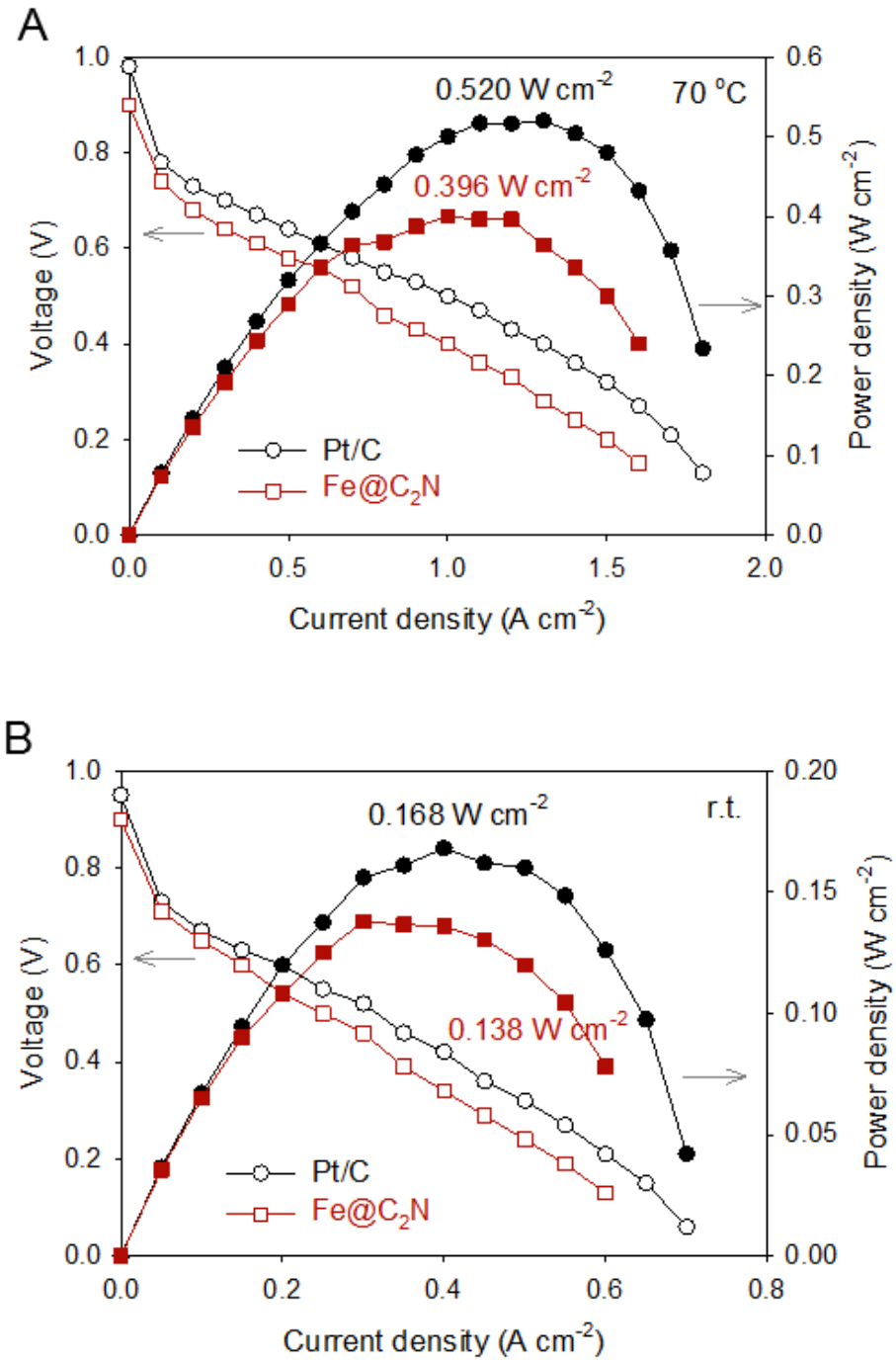

Figure 4-14. Performance of polymer electrolyte membrane fuel cell (PEMFC): (A) at 70 °C; (B) at room temperature.

4.14 Conclusions

In summary, we have, for the first time, synthesized a new class of Fe-cocooned C_2N (Fe@C_2N) electrocatalysts by a simple but efficient synthetic protocol. The structure of Fe nanoparticles encapsulated in 2-16 C_2N layers was confirmed by XRD, EXAFS and HR-TEM. In comparison with commercial Pt/C, Fe@C_2N displayed significantly improved catalytic activity with a superior stability in both acidic and alkaline aqueous solutions, suggesting a considerable cost reduction in air-breading electrodes for energy conversion devices (fuel cells and metal-air cells). The electrochemical performance of the Fe@C_2N catalyst can be attributed to the electrochemical transparency and stable encapsulation of Fe nanoparticles by C_2N layers. Hence, Fe@C_2N can be a potential alternative to Pt-based cathode materials for energy conversion devices. The approach described in this work could lead to the development of various non-precious metal-based electrocatalysts on C_2N platform for many different applications.

4.15 References

(1) Wen Z. et al., Nitrogen-enriched core-shell structured Fe/Fe_3C-C nanorods as advanced electrocatalysts for oxygen reduction reaction. Adv. Mater. **2012**, *24*, 1399-1404.

(2) Yeager E., Fuel cells: They produce more electricity per pound of fuel than any other nonnuclear method of power production. Science **1961**, *134*, 1178-1186.

(3) Li Y. et al., Advanced zinc-air batteries based on high-performance hybrid electrocatalysts. Nat. Commun. **2013**, *4*, 1805.

(4) Zhang J., Zhao Z., Xia Z., Dai L., A metal-free bifunctional electrocatalyst for oxygen reduction and oxygen evolution reactions. Nat. Nanotechnol. **2015**, *10*, 444-452.

(5) Steele B.C.H., Heinzel A., Materials for fuel-cell technologies. Nature **2001**, *414*, 345-352.

(6) B. Lim et al., Pd-Pt Bimetallic Nanodendrites with High Activity for Oxygen Reduction. Science **2009**, *324*, 1302-1305.

(7) Dai L., Xue Y., Qu L., Choi H.-J., Baek J.-B., Metal-Free catalysts for oxygen reduction reaction. Chem. Rev. **2015**, *115*, 4823-4892.

(8) Gong K., Du F., Xia Z., Durstock M., Dai L., Nitrogen-doped carbon nanotube arrays with high electrocatalytic activity for oxygen reduction. Science **2009**, *323*, 760-764.

(9) Qu L., Liu Y., Baek J.-B., Dai L., Nitrogen-doped graphene as efficient metal-free electrocatalyst for oxygen reduction in fuel cells. ACS Nano **2010**, *4*, 1321-1326.

(10) Yang Z., Nie H., Chen X.A., Chen X., Huang S., Recent progress in doped carbon nanomaterials as effective cathode catalysts for fuel cell oxygen reduction reaction. J. Power Sources **2013**, *236*, 238-249.

(11) Lefèvre M., Proietti E., Jaouen F., Dodelet J.-P., Iron-based catalysts with improved oxygen reduction activity in polymer electrolyte fuel cells. Science **2009**, *324*, 71-74.

(12) Jaouen F. et al., Recent advances in non-precious metal catalysis for oxygen-reduction reaction in polymer electrolyte fuel cells. Energy Environ. Sci. **2011**, *4*, 114-130.

(13) Chen Z., Higgins D., Yu A., Zhang L., Zhang J., A review on non-precious metal electrocatalysts for PEM fuel cells. Energy Environ. Sci. **2011**, *4*, 3167-3192.

(14) Thorum M. S., Yadav J., Gewirth A. A., Oxygen reduction activity of a copper complex of 3,5-diamino-1,2,4-triazole supported on carbon black. Angew. Chem. Int. Ed. 48, **2009**, 165-167.

(15) Yang W., Fellinger T.-P.,. Antonietti M, Efficient metal-free oxygen reduction in alkaline medium on high-surface-area mesoporous nitrogen-doped carbons made from ionic liquids and nucleobases. J. Am. Chem. Soc. **2010**, *133*, 206-209.

(16) Banham D.et al., A review of the stability and durability of non-precious metal catalysts for the oxygen reduction reaction in proton exchange membrane fuel cells. J. Power Sources **2015**, *285*,

334-348.

(17) Liu R., Wu D., Feng X., Müllen K., Nitrogen-doped ordered mesoporous graphitic arrays with high electrocatalytic activity for oxygen reduction. Angew. Chem. Int. Ed. **2010**, *49*, 2565-2569.

(18) Mahmood J., Kim D., Jeon I.-Y., Lah M. S., Baek J.-B., Scalable synthesis of pure and stable hexaaminobenzene Trihydrochloride. Synlett **2013**, *24*, 246-248.

(19) Mahmood J. et al., Nitrogenated holey two-dimensional structures. Nat. Commun. **2015**, *6*, 6486.

(20) Wang H. et al., Magnetic-Fe/Fe_3O_4-nanoparticle-bound SN38 as carboxylesterase-cleavable prodrug for the delivery to tumors within monocytes/macrophages. Beilstein J. Nanotechnol. **2012**, *3*, 444-455.

(21) Wu A., Liu D., Tong L., Yu L., Yang H., Magnetic properties of nanocrystalline Fe/Fe3C composites. CrystEngComm **2011**, *13*, 876-882.

(22) Paulus U. A., Schmidt T. J., Gasteiger H. A., Behm R. J., Oxygen reduction on a high-surface area Pt/Vulcan carbon catalyst: a thin-film rotating ring-disk electrode study. J. Electroanal. Chem. **2001**, *495*, 134-145.

(23) Shin D., Sinthika S., Choi M., Thapa R.,. Park N, Ab Initio study of thin oxide–metal overlayers as an inverse catalytic system for dioxygen reduction and enhanced CO tolerance. ACS Catalysis **2014**, *4*, 4074-4080.

(24) Deng D.et al., Iron Encapsulated within pod-like carbon nanotubes for oxygen reduction reaction. Angew. Chem. Int. Ed. **2013**, *52*, 371-375.

(25) Girishkumar G., McCloskey B., Luntz A. C., Swanson S, Wilcke W., Lithium−air battery: Promise and challenges. J. Phy. Chem. Lett. **2010**, *1*, 2193-2203.

(26) Li Y., Dai H., Recent advances in zinc-air batteries. Chem. Soc. Rev. 2014, 43, 5257-5275.

(27) Lee J.-S. et al., Metal–Air Batteries with high energy density: Li–air versus Zn–air. Adv. Energy Mater. **2011**, *1*, 34-50.

(28) Wang Y., Chen K. S., Mishler J., Cho S. C., Adroher X. C., A review of polymer electrolyte membrane fuel cells: Technology, applications, and needs on fundamental research. Appl. Energy **2011**, *88*, 981-1007.

Appendix 1: List of publications

1. Jeon, I.-Y.; Choi, M.; **Choi , H.-J.**; Jung, S.-M.; Kim, M.-J.; Seo, J.-M.; Bae, S.-Y.; Yoo, S.; Kim, G.; Jung, H. Y.; Park, N.; Baek, J.-B. "Antimony-doped graphene nanoplatelets" Nature Communications 2015, 6, 7123-highlighted in Chosun Daily, Dong-A Science and more than 40 Press Hits.

2. Dai, L.; Xue, Y.; Qu, L.; **Choi, H.-J**.; Baek, J.-B. "Metal-free catalysts for oxygen reduction reaction" Chemical Reviews 2015, 115, 4823-4892-Most Read Articles & Highlighted in YTN and more than 23 Press Hits

3. Mahmood, J.; Lee, E. K.; Jung, M.; Shin, D.; Jeon, I.-Y.; Jung, S.-M.; **Choi, H.-J**.; Seo, J.-M.; Bae, S.-Y.; Sohn, S.-D.; Park, N.; Oh, J. H.; Shin, H.-J.; Baek, J.-B. "Nitrogenated holey two-dimensional structures" Nature Communications 2015, 6, 6486-highlighted in CNBC, KBS, Chosun Daily and more than 333 Global News Hits

4. Jeon, I.-Y.; Kim, H. M.; Choi, I. T.; Lim, K.; Ko, J.; Kim, J. C.; **Choi, H.-J**.; Ju, M. J.; Lee, J.-J.; Kim, H. K.; Baek, J.-B. "High-performance dye-sensitized solar cells using edge-halogenated graphene nanoplatelets as counter electrodes" Nano Energy 2015, 13, 336-345.

5. Chang, D. W.*; **Choi, H.-J.*;** Baek, J.-B. "Wet-chemical nitrogen-doped graphene nanoplatelets as electrocatalysts for oxygen reduction reaction" Journal of Materials Chemistry A 2015, 3, 7659-7665.

6. **Choi, H.-J.**; Kumar, N. A.; Baek, J.-B. "Graphene supported non-precious metal-macrocycle catalysts for oxygen reduction reaction in fuel cells" Nanoscale 2015, 7, 6991-6998-Invited Feature Article.

7. Jeon, I.-Y.; Ju, M. J.; **Choi, H.-J.**; Seo, J.-M.; Kim, M.-J.; Choi, I. T.; Kim, H. M.; Kim, J.- C.; Lee, J.-J.; Kim, H. K.; Dou, S.; Dai, L.; Baek, J.-B. "Edge-fluorinated graphene nanoplatelets as high performance electrodes for dye-sensitized solar cells and lithium-ion batteries" Advanced Functional Materials 2015, 25, 1170-1179. -selected as a Back Cover Article.

8. Chang, D. W.*; **Choi, H.-J.***; Jeon, I.-Y.; Seo, J.-M.; Dai, L.; Baek, J.-B. "Solvent-free mechanochemical reduction of graphene oxide" Carbon 2014, 77, 501-507-Most downloaded articles

9. Filer, A.; **Choi, H.-J.**; Seo, J.-M.; Baek, J.-B. "Two and three dimensional network polymers for electrocatalysis" Physical Chemistry Chemical Physics 2014, 16, 11150-11161. Invited Perspective..

10. Chang, D.-W.; **Choi, H.-J.**; Filer, A.; Baek, J.-B. "Graphene in photovoltaic applications: Organic photovoltaic cells (OPVs) and dye-sensitized solar cells (DSSCs)" Journal of Materials Chemistry A 2014, accepted-Invited Feature Article.

11. Ju, M. J.; Jeon, I.-Y.; Kim, J. C.; Lim, K.; **Choi, H.-J.**; Choi, I. T; Eom, Y. K.; Kwon, Y. J.; Ko, J.; Lee, J.-J.; Kim, H. K.; Baek, J.-B. "Graphene Nanoplatelets Doped with N at its Edges as Metal-Free Cathodes for Organic Dye-Sensitized Solar Cells" Advanced Materials 2014, 26, 3055-3062.

12. Ju, M. J.; Jeon, I.-Y.; Lim, K.; Kim, J. C.; **Choi, H.-J.**; Choi, I. T; Eom, Y. K.; Kwon, Y. J.; Ko, J.; Lee, J.-J.; Baek, J.-B.; Kim, H. K. "Edge-carboxylated graphene nanoplatelets as oxygen-rich metal-free cathodes for organic dye-sensitized solar cells" Energy and Environmental Science 2014, 7, 1044-1052.

13. Jeon, I.-Y.; Zhang, S.; Zhang L.; **Choi, H.-J.**; Seo, J.-M.; Xia, Z.; Dai, L.; Baek, J.-B. "Edge-Selectively Sulfurized Graphene Nanoplatelets as Efficient Metal-Free Electrocatalysts for Oxygen Reduction Reaction: The Electron Spin Effect" *Advanced Materials* 2013, 25, 6138-6145.

14. Jeon, I.-Y.*; **Choi, H.-J.***; Ju, M. J.*; Choi, I. T.; Lim, K.; Ko, J.; Kim, H. K.; Kim, J. C.; Lee, J.-J.; Shin, D..; Jung, S.-M.; Seo, J.-M.; Kim, M.-J.; Park, N.; Dai, L.; Baek, J.-B. "Direct nitrogen fixation at the edges of graphene nanoplatelets as efficient electrocatalysts for energy conversion" Scientific Reports 2013, 3, DOI: 10.1038/srep02260 (Highlighted in Science Daily and more than Fourty Global News Hits).

15. Kim, S. G.; Ju, M. J.; Choi, I. T.; Choi, W. S.; **Choi, H.-J.**; Baek, J.-B.; Kim, H. K. "Nb-doped TiO_2 Nnanoparticles as rrganic dye-sensitized solar cells" *RSC Advances* 2013, accepted.

16. Chang, D. W.; Lee, E, K.; Park, E. Y.; Yu, H.; **Choi, H.-J.**; Son, G.-J. Shin, D.; Park, N.; Oh, J. H.; Dai, L.; Baek, J.-B. "Nitrogen-doped Graphene Nanoplatelets from Simple Solution Edge-Functionalization for n-Type Field-Effect Transistors" *Journal of the American Chemical Society* 2013, 135, 8981-8988 (Highlighted in Graphene Times.com).

17. Ju, M. J.*; Kim, J. C*.; **Choi, H.-J.***; Choi, I. T.; Kim, S. G.; Lim, K. M.; Ko, J.; Lee, J. J.; Jeon,

I.-Y.; Baek, J.-B.; Kim, H. K. “N-Doped Graphene Nanoplatelets as Superior Metal-Free Counter Electrodes for Organic Dye-Sensitized Solar Cells” ACS Nano 2013, 7, 5243-5250

18. Jeon, I.-Y.*; **Choi, H.-J.***; Choi, M.*; Seo, J.-M.; Jung, S.-M.; Kim, M.-J.; Zhang, S.; Zhang, L.; Xia, Z.; Dai, L.; Park, N.; Baek, J.-B. "Facile, scalable synthesis of edge-halogenated graphene nanoplatelets as efficient metal-free electrocatalysts for oxygen reduction reaction" Scientific Reports 2013, accepted.

19. Chang, D. W.; **Choi, H.-J.**; Jeon, I.-Y.; Baek, J.-B. “Edge-selectively functionalized graphene nanoplatelets” *Chem. Rec.* 2013, 13, 224-238 (Invited Review Article).

20. Jeon, I.-Y.*; **Choi, H.-J.***; Jung, S.-M.; Seo, J.-M.; Kim, M.-J.; Dai, L.; Baek, J.-B. “Large-scale production of edge-selectively functionalized graphene nanoplatelets via ball-milling and their use as metal-free electrocatalysts for oxygen reduction reaction” *Journal of the American Chemical Society* 2013, 135, 1386-1393 (Highlighted in Science Daily, Chosun Daily, Dong-A Daily, Graphene Times.com and more than Twenty Global News Hits).

21. Sohn, G.-J.; **Choi, H.-J.**; Jeon, I.-Y.; Chang, D. W.; Dai, L.; Baek, J.-B. "Water-dispersible, sulfonated hyperbranched poly(ether-ketone) grafted multi-walled carbon nanotubes as oxygen reduction catalysts" *ACS Nano* 2012, 6, 6345-6355.

22. **Choi, H.-J.**; Jung, S.-M.; Seo, J.-M.; Chang, D. W.; Dai, L.; Baek, J.-B. "Graphene for energy conversion and storage infuel cells and supercapacitors" *Nano Energy* 2012, 1, 534-551 (Invited Review Article).

23. Chang, D. W.; **Choi, H.-J.**; Jung, S.-M.; Dai, L.; Baek, J.-B. “Large Cluster and Hallow Microfibers by Multicomponent Self-Assembling of Citrate Stabilized Gold Nanoparticles with Temperature-Responsive Amphiphilic Dendrimers” *Journal of Materials Chemistry* 2012, 22, 13365-13373.

24. Kumar, N. A.; **Choi, H.-J.**; Bund, A.; Baek, J.-B.; Jeong, Y. T. “Electrochemical supercapacitors based on a novel graphene/conjugated polymer composite system” *Journal of Materials Chemistry* 2012, 22, 12268-12274.

25. Jeon, I.-Y.; Shin, Y.-R.; Sohn, G.-J.; **Choi, H.-J.**; Bae, S.-Y.; Mahmood, J.; Jung, S.-M.; Seo, J.-M.; Kim, M.-J.; Chang, D.-W.; Dai, L.; Baek, J.-B. “Edge-carboxylated graphene nanosheets via ball milling” *Proceedings of the National Academy of Sciences, USA*, 2012, 109, 5588-5593 (Hi

ghlighted in Science Daily, Chosun.com, KBS World, and more than 100 times of global News Hits)

26. Kumar, N. A.; **Choi, H.-J.**; Shin, Y.-R.; Chang, D. W.; Dai, L.; Baek, J.-B. "Polyaniline-Grafted Reduced Graphene Oxide for Efficient Electrochemical Supercapacitors" *ACS Nano* 2012, 6, 17 15-1723 (Top Twenty Most Read Articles in March, 2012, Highlighted in Graphene Times.com).

27. **Choi, H.-J.**; Kang, J.-Y.; Jeon, I.-Y.; Eo, S.-M.; Tan, L.-S.; Baek, J.-B. "Immobilization of Plati num Nanoparticles on ortho-Diaminobenzoyl-Functionalized Multi-Walled Carbon Nanotube an d Its Electrocatalytic Activity" *Journal of Nanoparticle Research* 2012, 14, 704.

28. **Choi, H.-J.**; Jeon, I.-Y.; Kang, S.-W.; Baek, J.-B. "Electrochemical activity of a polyaniline/pol yaniline-grafted multiwalled carbon nanotube mixture produced by a simple suspension polymer ization" *Electrochimica Acta* 2011, 56,10023-10031.

29. Jeon, I.-Y.; Yu, D.; Bae, S.-Y.; **Choi, H.-J.**; Chang, D. W.; Dai, L.; Baek, J.-B. "Formation of L arge-Area Nitrogen-Doped GrapheneFilm Prepared from Simple Solution Casting of Edge-Selec tively Functionalized Graphite and Its Electrocatalytic Activity" *Chemistry of Materials* 2011, 2 3(7), 3987-3992. (Top Twenty Most Read Articles in September, 2011, Highlighted in Graphene Times.com).

30. Jeon, I.-Y.; **Choi, H.-J.**; Bae, S.-Y.; Chang, D. W.; Baek, J.-B. "Wedging graphite into graphene and graphene-like platelets by dendritic macromolecules" *Journal of Materials Chemistry* 2011, 21, 7820-7826.

31. Jeon, I.-Y.; **Choi, H.-J.**; Tan, L.-S.; Baek, J.-B. "Nanocomposite prepared from in-situ grafting o f polypyrrole to aminobenzoyl-functionalized multi-walled carbon nanotube and its electrochemi cal properties" *Journal of Polymer Science, Part A: Polymer Chemistry* 2011, 49, 2529-2537.

32. **Choi, H.-J.**; Jeon, I.-Y.; Chang, D. W.; Yu, D.; Dai, L.; Tan, L.-S.; Baek, J.-B. "Preparation and electrocatalytic activity of gold nanoparticles immobilized onto the surface of mercaptobenzoyl-functionalized multi-walled carbon nanotubes" *Journal of Physical Chemistry C* 2011, 115, 1746-1751.

Appendix 2: International proceedings

1. **Hyun-Jung Choi**, Jong-Beom Baek “The synthesis of mercaptobenzoyl functionalized graphene/platinum nanoparticle composites” Recent Progress in Graphene Research 2011, (Suwon, October 3-6).

2. In-Yup Jeon, **Hyun-Jung Choi**, Seo-Yoon Bae, Dong Wook Chang, Jong-Beom Baek “ Wedging graphite into graphene and graphene-like platelets by dendritic macromolecules” Recent Progress in Graphene Research 2011, (Suwon, October 3-6).

3. **Hyun-Jung Choi**, In-Yup Jeon, Jong-Beom Baek "Stable anchoring of gold nanoparticle onto thiol-functionalized multi-walled carbon nanotube and its electrochemical properties " MRS. 2009 fall meeting, Prepr. Boston, MA, November 30-December 4.

4. **Hyun-Jung Choi**, In-Yup Jeon, Loon-Seng Tan, Jong-Beom Baek "Synthesis and properties of gold nanopaticle/thiol-functionalized multi-walled carbon nanotube composites" Polym. Prepr. 2009, 49(2), Salt Lake, UT, March 22-26.

Appendix 3: Domestics proceedings

1. **Hyun-Jung Choi,** In-Yup Jeon and Jong-Beom Baek "Nitrogen Doped Graphene/Carbon Nanotube Composite for Supercapacitors" The Polymer Society of Korea 2013, 38(2), (Changwon, October 10-11).

2. **Hyun-Jung Choi**, In-Yup Jeon, Min Choi, Jeong-Min Seo, Sun-Min Jung, Min-Jung Kim, Shen g Zhang, Lipeng Zhang, Zhenhai Xia, Liming Dai, Noejung Park and Jong-Beom Baek "Edge-ha logenated graphene nanoplatelets for the oxygen reduction reaction in fuel cells" The Korean Soc iety of Industrial and Engineering Chemistry 2013, 47, (Jeju, May 1-3).

3. **Hyun-Jung Choi**, In-Yup Jeon, Min Choi, Jeong-Min Seo, Sun-Min Jung, Min-Jung Kim, Shen g Zhang, Lipeng Zhang, Zhenhai Xia, Liming Dai, Noejung Park and Jong-Beom Baek "Edge-ha logenated graphene nanoplatelets as electrocatalysts for the oxygen reduction reaction" The Poly mer Society of Korea 2013, 38(1), (Daejeon, April 11-12).

4. In-Yup Jeon, Sheng Zhang, Lipeng Zhang, **Hyun-Jung Choi**, Jeong-Min Seo, Zhenhai Xia and J ong-Beom Baek "Edge-Selectively sulfurized Graphene Nanoplatelets as efficient Metal-Free El ectrocatalysts for Oxygen Reduction Reaction: The Electron Spin Effect" The Polymer Society o f Korea 2013, 38(1), (Daejeon, April 11-12).

5. **Hyun-Jung Choi**, In-Yup Jeon, Liming Dai and Jong-Beom Baek "Large-Scale Production of E dge-Selectively Functionalized Graphene Nanoplatelets *via* Ball-Milling and Their Use as Metal-Free Electrocatalysts for Oxygen Reduction Reaction" Korean Carbon Society 2012, (Jeonbuk, N ovember, 8-9)

6. In-Yup Jeon, Yeon-Ran Shin, Gyung-Joo Sohn, **Hyun-Jung Choi**, Seo-Yoon Bae, Javeed Mahmood, Sun-Min Jung, Jeong-Min Seo, Min-Jung Kim, Dongwook Chang, Liming Dai and Jong-Beom Baek "Edge-Functionalized Graphite via a simple and eco-friendly Ball-Milling" Korean Carbon Society 2012, (Jeonbuk, November, 8-9)

7. **Hyun-Jung Choi**, In-Yup Jeon and Jong-Beom Baek "Edge-Functionalized Graphene Nanoplatelets as Catalysts for Oxygen Reduction Reaction" The Korean Chemical Society 2012, (Busan, October 17-19).

8. **Hyun-Jung Choi**, In-Yup Jeon and Jong-Bem Baek, "Edge-Functionalized Graphene Nanoplatelets as Catalysts for Oxygen Reduction Reaction" The Polymer Society of Korea 2012, 37(2), (Changwon, October 11-12).

9. **Hyun-Jung Choi** and Jong-Beom Baek "Electrocatalytic Activities of Platinum Nanoaprticles on Graphene Sheets for Fuel Cell Applications" The Polymer Society of Korea 2012, 37(1), (Daejeon, April 12-13).

10. In-Yup Jeon, Dingshan Yu, Seo-Yoon Bae, **Hyun-Jung Choi**, Dong Wook Chang, Liming Dai, Jong-Beom Baek "Formation of large area nitrogen doped graphene film prepared from simple solution casting of edge-selectively functionalized graphite and its electrocatalytic activity" The Polymer Society of Korea 2011, 36(2), (Gwangu, October 6-7).

11. **Hyun-Jung Choi**, Ji-Ye Kang, In-Yup Jeon, Soo-Mi Eo, Loon-Seng Tan, Jong-Beom Baek " The synthesis of Nitrogen Doped Multi-walled Carbon Nanotube Catalyst for Oxygen Reduction Reaction" The Polymer Society of Korea 2011, 36(2), (Gwangu, October 6-7).

12. **Hyun-Jung Choi**, Jong-Beom Baek "The Synthesis of Edge Functionalized Graphene with 4-Mercaptobenzoic acid and Mercaptobenzoyl Functionalized Graphene/platinum Nanoparticle Composites" The polymer Society of Korea 2011, 36(1), (Daejeon, April 7-8).

13. **Hyun-Jung Choi**, In-Yup Jeon, Jong-Beom Baek "Preparation and electrocatalytic activity of gold nanoparticles immobilized onto the surface of mercaptobenzoyl-functionalized multi-walled carbon nanotubes" The polymer Society of Korea 2010, 35(2), (Daegu, October 7-8).

14. **Hyun-Jung Choi**, Jong-Beom Baek "GNP/mercaptobenzoyl-functionalized multi-walled carbon nanotube composites." The polymer Society of Korea 2010, 35(1), (Daejeon, April 8-9).

15. **Hyun-Jung Choi**, Jong-Beom Baek "Synthesis of thiol-functionalized multi-walled carbon nanotube/gold nano-particle composites and its electrochemical properties" The polymer Society of Korea 2009, 34(2), (Gwangu, October 8-9).

16. **Hyun-Jung Choi**, Jong-Beom Baek "Synthesis and properties of gold nanopaticle/thiol-functionalized multi-walled carbon nanotube composites" The Polymer Society of Korea 2009, 34(1) (Daejeon, April 9-10).

Appendix 4: Books

1. Chang, D. W.; Jeon, I.-Y.; Choi, H.-J.; Baek, J.-B. “Mild and nondestructive chemical modification of carbon nanotubes (CNTs): Direct Friedel-Crafts acylation reaction” Recent Progress in Carbon Nanotube Research/Book 2, InTech Open Access Publisher, 2012. ISBN: 980-953-307-485-1

Appendix 5: Permission from all cited journal papers in this thesis

Chapter 1 (from Graphene supported non-precious metal-macrocycle catalysts for oxygen reduction reaction in fuel cells." Nanoscale, 2015, 7, 6991)

Graphene supported non-precious metal-macrocycle catalysts for oxygen reduction reaction in fuel cells

H. Choi, N. Ashok Kumar and J. Baek, *Nanoscale*, 2015, **7**, 6991
DOI: 10.1039/C4NR06831A

If you are not the author of this article and you wish to reproduce material from it in a third party non-RSC publication you must formally request permission using RightsLink. Go to our Instructions for using RightsLink page for details.

Authors contributing to RSC publications (journal articles, books or book chapters) do not need to formally request permission to reproduce material contained in this article provided that the correct acknowledgement is given with the reproduced material.

Reproduced material should be attributed as follows:

- For reproduction of material from NJC:
  Reproduced from Ref. XX with permission from the Centre National de la Recherche Scientifique (CNRS) and The Royal Society of Chemistry.
- For reproduction of material from PCCP:
  Reproduced from Ref. XX with permission from the PCCP Owner Societies.
- For reproduction of material from PPS:
  Reproduced from Ref. XX with permission from the European Society for Photobiology, the European Photochemistry Association, and The Royal Society of Chemistry.

Chapter 2. (from "Immobilization of platinum nanoparticles on 3,4-diaminobenzoyl-functionalized multi-walled carbon nanotube and its electrocatalytic acitivty", Journal of Nanoparticle Research 2012, 14, 704)

SPRINGER LICENSE
TERMS AND CONDITIONS

Jan 13, 2016

This is an Agreement between Hyunjung Choi ("You") and Springer ("Springer"). It consists of your order details, the terms and conditions provided by Springer, and the payment terms and conditions.

All payments must be made in full to CCC. For payment instructions, please see information listed at the bottom of this form.

License Number	3786881440523
License date	Jan 13, 2016
Licensed Content Publisher	Springer
Licensed Content Publication	Journal of Nanoparticle Research
Licensed Content Title	Immobilization of platinum nanoparticles on 3,4-diaminobenzoyl-functionalized multi-walled carbon nanotube and its electrocatalytic activity
Licensed Content Author	Hyun-Jung Choi
Licensed Content Date	Jan 1, 2012
Volume number	14
Issue number	2
Type of Use	Thesis/Dissertation
Portion	Full text
Number of copies	5
Author of this Springer article	Yes and you are the sole author of the new work
Order reference number	None
Title of your thesis / dissertation	Carbon-based Electrocatalysts for Oxygen Reduction Reactions
Expected completion date	Feb 2016
Estimated size(pages)	120
Total	**0.00 USD**
Terms and Conditions	

Chapter 3 (from "Facile, scalable synthesis of edge-halogenated graphene nanoplatets as efficient metal-free electrocatalysts for oxygen reduction reaction", Scientific Reports 2013, 3, 1810.)

Acknowledgement

학위를 시작한지 얼마 되지 않은 것 같은데 어느덧 박사학위를 마무리 짓는 시점이 되었습니다. 그동안 힘들고 보람되며 울고 웃던 많은 시간들이 주마등 처럼 지나가는 것 같습니다. 학위를 하면서 많은 고마운 분들이 생각이 납니다.

먼저 박사학위를 지도해주신 백종범 교수님, 학부 4 학년부터 지도교수님으로 시작되어 석사, 박사 과정까지 많은 가르침과 지도편달 때문에 여기까지 온게 아닌가 생각됩니다. 한번씩 흐트러질때마다 다잡아주시고, 가야할 방향에 대해서 같이 고민해주시고 조언해주셔서 감사드립니다.

또 논문 심사를 해주신 조재필교수님, 송현곤교수님, 김건태 교수님, 장동욱 교수님께도 깊은 감사를 드립니다.

그리고 같이 생활했던 CDCOF 선배님, 동기, 후배들.

주명종 교수님, 고려대 계실때부터 인연이 되어 같이 많은 연구를 할수 있어서 좋았습니다. 인엽이 오빠 항상 잘 챙겨주셔서 감사했어요. 서윤이는 동기 이상의 후배였어. 박사기간동안 많이 의지도 하고 도움도 많이 받았던 것같애. I'm very thank to Javeed for the help. I wish you all the best in the future. 항상 긍정 마인드 선민이, 겉은 까칠하지만 속은 따뜻한 정민이, 그리고 실험실 후배들 석진이, 윤광이, 선희, 혁준이, 도형이, Ishfaq 모두의 도움이 있어서 너무 고마웠어.

학교생활을 하며 만난 소중한 인연, 보람이 오빠, 상하오빠, 재환이 오빠, 효진이 오빠, 오빠들 덕에 즐거운 학교생활 할수 있었던 것 같애. 즐거운 추억을 공유할 수 있는 사람들이 있는것만으로도 큰 행복인것같아. 언제 또 그런시간들을 갖을수 있을까 생각이 들기도하지만, 각자 분야에서 열심히 하고 있는 모습 항상 응원할게!

경식아 20 살때부터 지금까지 좋은 친구로 그리고 동료로 함께해서 좋았어. 경식이의 진면목을 대학교때보다 대학원 들어와서 더 느낄수 있었던 것같애. 배려 많고 착한 경식이. 조만간 좋은 소식으로 함께하자.

박사기간 동안 제게는 소중한 가족이 생겼습니다. 사랑하는 남편 고영훈. 그대가 있어 가족과 학위 두마리 토끼를 다잡을 수 있었던 것 같아. 학교에서는 전기화학의 개인 선생님이었고, 집에서는 최고의 남편이었어. 항상 나의 편이 있다는 것만으로도 큰힘이야. 나의 보물 고유준. 지금처럼 건강하고 밝게 자라자. 앞으로도 엄마가 많이 사랑해줄게.

그리고 지금껏 뒤에서 묵묵히 저를 믿어주시고 지지해주셨던 부모님. 너무 감사하고 사랑합니다. 그리도 나의 동생 병진이 노력뒤엔 좋은 결과가 있을거라 확신해. 열심히 하는 모습이 아름답다.

그리고 아버님, 어머님 항상 응원해주시고 좋은 말씀 많이해주셔서 감사합니다.

끝으로 앞으로 더욱 열심히 하고 좋은 모습 보여드리도록 노력하는 사람이 되겠습니다. 제 주변의 모든 분들에게 행복한 일들만 가득하길 기원합니다. 감사합니다.

2016 년 1 월

최현정 드림.